

# Arbeitsbericht NAB 13-86

**Numerical reproduction  
and sensitivity analysis  
of undrained triaxial test results**

April 2014

W. Shiu, D. Billaux  
ITASCA

Nationale Genossenschaft  
für die Lagerung  
radioaktiver Abfälle

Hardstrasse 73  
CH-5430 Wettingen  
Telefon 056-437 11 11

[www.nagra.ch](http://www.nagra.ch)



# Arbeitsbericht NAB 13-86

**Numerical reproduction  
and sensitivity analysis  
of undrained triaxial test results**

April 2014

W. Shiu, D. Billaux  
ITASCA

**KEYWORDS**

Numerical modelling, FLAC, undrained, triaxial,  
Schlattingen-1

**Nationale Genossenschaft  
für die Lagerung  
radioaktiver Abfälle**

Hardstrasse 73  
CH-5430 Wettingen  
Telefon 056-437 11 11

[www.nagra.ch](http://www.nagra.ch)

Nagra Working Reports concern work in progress that may have had limited review. They are intended to provide rapid dissemination of information. The viewpoints presented and conclusions reached are those of the author(s) and do not necessarily represent those of Nagra.

"Copyright © 2014 by Nagra, Wettingen (Switzerland) / All rights reserved.

All parts of this work are protected by copyright. Any utilisation outwith the remit of the copyright law is unlawful and liable to prosecution. This applies in particular to translations, storage and processing in electronic systems and programs, microfilms, reproductions, etc."

## Zusammenfassung

Kernproben von Opalinuston aus der Tiefbohrung Schlattingen-1 (Albert et al. 2012) wurden kürzlich in einem umfassenden geomechanischen Laborprogramm charakterisiert (Jahns 2013). Zentraler Bestandteil des Laborprogramms waren undrainierte Triaxialversuche zur Untersuchung des Kurzzeitverhaltens von Opalinuston auf mechanische Beanspruchung.

Im vorliegenden Bericht werden ausgesuchte Experimente aus diesem Laborprogramm numerisch nachmodelliert. Als Materialgesetz für das elasto-plastische Verhalten wurde dafür das in FLAC implementierte, transversal-isotrope und bilineare strain-hardening-softening-Gesetz mit Zugspannungsbegrenzung verwendet (das sogenannte *subiquitous joint model*, kurz *SUBI*). Es handelt sich dabei um dasselbe Stoffgesetz, welches für den Opalinuston bezüglich Deformations- und Bruchverhalten in bautechnischen Fragestellungen auch in der Vergangenheit verwendet wurde (Nagra 2002; TeKamp 2008).

Die numerische Reproduktion der Laborexperimente verfolgt zwei Hauptziele. Erstens soll für den Opalinuston eine Konsistenzprüfung bezüglich des verwendeten Materialgesetzes durchgeführt werden durch Vergleich mit Laborexperimenten, welche bei kontrollierten Zustandsbedingungen ausgeführt wurden. Zweitens sollen durch Parameterstudien die Unsicherheiten des Materialgesetzes untersucht werden, insbesondere für experimentell nur schwer bestimmbare Grössen wie etwa der hydromechanischen Kopplungsparameter.

Generell können die in Laborversuchen beobachteten Phänomene bezüglich des mechanischen Verhaltens von Opalinuston durch die numerischen Modellrechnungen gut reproduziert werden. Sowohl die Verfestigung im Vorbruchbereich (strain-hardening) wie auch die Entfestigung bei grösserer Scherdehnung (strain-softening) können durch geeignete Kalibrierung nachgebildet werden. Auch die Festigkeitsanisotropie ist durch Berücksichtigung von "verschmierten Schichtflächen", beziehungsweise der Unterscheidung von "Matrix-" und "Schicht-"Eigenschaften implizit in SUBI berücksichtigt. Schliesslich wird in den numerischen Modellrechnungen auch eine relativ starke Lokalisierung der Deformation durch Ausbildung von Scherbändern beobachtet, welche qualitativ mit den diskreten Bruchflächen in den Laborversuchen in Einklang stehen.

Nicht berücksichtigt wird in SUBI die in Laborversuchen beobachtete Anisotropie der Steifigkeit. Entsprechend kann für den verwendeten Parametersatz eine gute Annäherung des mechanischen Verhaltens nicht gleichzeitig für die "Matrix" und die "Schichtung" erreicht werden. Diese Limitierung ist im Bericht durch die Wahl sowohl eines 'steifen' als auch eines 'weichen' Parametersets vergleichend dargestellt. Ein 'weicher' Parametersatz liefert eine bessere Annäherung an das mechanische Verhalten für Proben, in welchen die Belastungsrichtung unter einem hohen Winkel zur "Schichtung" steht. Umgekehrt liefert der 'steife' Parametersatz eine viel bessere Annäherung für eine Belastungsrichtung mit sehr kleinem Winkel zur "Schichtung".



## Table of Contents

Zusammenfassung.....	I
Table of Contents .....	III
List of Tables.....	IV
List of Figures .....	V
<b>1 Introduction .....</b>	<b>1</b>
<b>2 Experimental data base.....</b>	<b>3</b>
2.1 Sample description and orientation convention.....	3
2.2 Triaxial experimental data .....	3
<b>3 Model description .....</b>	<b>7</b>
3.1 Numerical sample .....	7
3.2 Model setup .....	7
3.3 Choice of Poroelastic parameters for the model.....	10
3.4 Parametric study scope .....	10
<b>4 Results and discussions.....</b>	<b>13</b>
4.1 Investigation of softening behavior .....	13
4.1.1 Critical strain of the cohesion/internal friction angle for matrix .....	13
4.1.2 Critical strain of the cohesion/internal friction angle for bedding.....	17
4.1.3 Softening behavior – comparison between FLAC3D and experimental data.....	20
4.2 Variation of dilation angle.....	30
4.3 Introducing hardening behavior.....	32
4.4 Variation in pore pressure coupling parameters .....	37
4.4.1 Biot coefficient .....	38
4.4.2 Skempton B – lower value (0.225 to 0.25).....	42
4.4.3 Skempton B - higher value (0.7 to 0.9).....	46
<b>5 Comparison between FLAC3D and laboratory experiments .....</b>	<b>53</b>
5.1 Parameter set 1 – "stiff" Opalinus Clay .....	53
5.2 Parameter set 2 – "soft" Opalinus Clay .....	64
5.3 Shear band formation.....	71
5.4 Boundary condition effect .....	76
5.5 Angle between loading and bedding orientation .....	82
<b>6 Conclusions.....</b>	<b>85</b>
<b>7 References.....</b>	<b>87</b>
<b>Appendix A: Bilinear, strain-(hardening-)softening ubiquitous joint model .....</b>	<b>A-1</b>

<b>Appendix B:</b>	<b>Strain dependency to the mesh discretization</b> .....	B-1
<b>Appendix C:</b>	<b>Parameter set used for the different modelling runs</b> .....	C-1
<b>Appendix D:</b>	<b>Structure of the electronic data base</b> .....	D-1

## List of Tables

Tab. 2-1:	Test conditions and results of selected laboratory tests from Jahns (2013).....	5
Tab. 2-2:	Material properties from laboratory test data provided by Nagra.....	6
Tab. 3-1:	Poroelastic parameters. ....	10
Tab. 4-1:	Residual critical strain (reference case).....	13
Tab. 4-2:	Governing parameters for different samples. ....	20
Tab. 4-3:	Hardening-softening parameters at initial, peak and residual state (cohesion).....	33
Tab. 4-4:	Hardening-softening parameters at initial, peak and residual state (friction angle). ....	34
Tab. 4-5:	Parameters set for cases using different Biot coefficient.....	38
Tab. 4-6:	Parameters set for cases using different $B_{sk}$ .....	38
Tab. 4-7:	Parameter set for $B_{sk}$ tests.....	47
Tab. 5-1:	"Stiff" parameter set for the FLAC3D model.....	54
Tab. 5-2:	"Soft" parameter set for the FLAC3D model. ....	65

## List of Figures

Fig. 2-1:	Plug orientation with respect to bedding (indicated by horizontal lines). .....	3
Fig. 2-2:	Important parameters of a single stage triaxial test with brittle failure. ....	4
Fig. 3-1:	Layout of the numerical sample. ....	7
Fig. 3-2:	Bedding plane orientation for numerical samples (dashed line).....	7
Fig. 3-3:	Stresses and pore pressure initialization. ....	8
Fig. 3-4:	Velocity boundary condition for top and bottom zones, stress boundary condition for lateral zones. ....	9
Fig. 3-5:	Strain and stress measurements during numerical triaxial simulation.....	9
Fig. 3-6:	Softening behavior as function of the critical strain. ....	11
Fig. 4-1:	Influence of $\gamma_{mc1}$ and $\gamma_{mf1}$ for P samples. ....	14
Fig. 4-2:	Influence of $\gamma_{mc1}$ and $\gamma_{mf1}$ for S samples. ....	15
Fig. 4-3:	Influence of $\gamma_{mc1}$ and $\gamma_{mf1}$ for X samples. ....	15
Fig. 4-4:	Influence of $\gamma_{mc1}$ and $\gamma_{mf1}$ for Z samples.....	16
Fig. 4-5:	Influence of $\gamma_{mc2}$ and $\gamma_{mf2}$ for P samples. ....	16
Fig. 4-6:	Influence of $\gamma_{mc2}$ and $\gamma_{mf2}$ for Z samples. ....	17
Fig. 4-7:	Influence of $\gamma_{jc1}$ and $\gamma_{jf1}$ for P samples.....	18
Fig. 4-8:	Influence of $\gamma_{jc1}$ and $\gamma_{jf1}$ for Z samples.....	18
Fig. 4-9:	Influence of $\gamma_{jc2}$ and $\gamma_{jf2}$ for P samples.....	19
Fig. 4-10:	Influence of $\gamma_{jc2}$ and $\gamma_{jf2}$ for Z samples.....	19
Fig. 4-11:	Ccomparison of stress-strain evolution between FLAC3D (numerical test results) and laboratory experimentsfor P samples. ....	22
Fig. 4-12:	Matrix plastic shear strain at the end of the test for P samples.....	23
Fig. 4-13:	Pore pressure increment comparison between FLAC3D and laboratory experiments (P samples).....	23
Fig. 4-14:	Volumetric strain and pore pressure, P samples (YZ cutting plane). ....	24
Fig. 4-15:	Comparison of stress-strain evolution between FLAC3D and laboratory experiments for S samples.....	24
Fig. 4-16:	Matrix plastic shear strain at the end of the test for S samples.....	25
Fig. 4-17:	Pore pressure increment comparison between FLAC3D and laboratory experiments (S samples).....	25
Fig. 4-18:	Volumetric strain and pore pressure, S samples (YZ cutting plane). ....	26

Fig. 4-19: Comparison of stress-strain evolution between FLAC3D and laboratory experiments (X samples). .....	26
Fig. 4-20: Bedding plastic shear strain at the end of the test, X samples. ....	27
Fig. 4-21: Pore pressure increment comparison between FLAC3D and laboratory experiments (X samples). ....	27
Fig. 4-22: Volumetric strain and pore pressure, X samples (YZ cutting plane).....	28
Fig. 4-23: Comparison of stress-strain evolution between FLAC3D and laboratory experiments (Z samples).....	28
Fig. 4-24: Bedding plastic shear strain at the end of the test, Z samples.....	29
Fig. 4-25: Pore pressure increment comparison between FLAC3D and laboratory experiments (Z samples).....	29
Fig. 4-26: Volumetric strain and pore pressure, Z samples (YZ plane). ....	30
Fig. 4-27: Influence of the dilation angle for P samples. ....	31
Fig. 4-28: Influence of the dilation angle for Z samples. ....	31
Fig. 4-29: Previous softening curve (left) and new hardening softening curve (right). ....	33
Fig. 4-30: Evolution of cohesion for matrix (left) and for bedding (right).....	33
Fig. 4-31: Stress-strain curve accounting for hardening behavior (P samples). ....	34
Fig. 4-32: Pore pressure increment accounting for hardening behavior (P samples). ....	35
Fig. 4-33: Stress-strain curve accounting for hardening behavior (Z samples).....	36
Fig. 4-34: Pore pressure increment account for hardening behavior (Z samples).....	36
Fig. 4-35: Resulting stress-strain curves from variation of Biot coefficient $\alpha$ (P samples). ....	39
Fig. 4-36: Resulting pore pressure increments from variation of Biot coefficient $\alpha$ (P samples). ....	40
Fig. 4-37: Verification of $B_{sk}$ for cases using different Biot coefficients (P samples). ....	40
Fig. 4-38: Stress-strain curve using different Biot coefficients (Z sample). ....	41
Fig. 4-39: Pore pressure increments from variation of Biot coefficient $\alpha$ (Z samples).....	41
Fig. 4-40: Verification of $B_{sk}$ for cases using different Biot coefficients (Z samples).....	42
Fig. 4-41: Stress-strain curve for different $B_{sk}$ (P samples). ....	43
Fig. 4-42: Pore pressure increment for different $B_{sk}$ (P samples).....	43
Fig. 4-43: Verification of $B_{sk}$ for cases using different $B_{sk}$ (P samples). ....	44
Fig. 4-44: Stress-strain curve for different $B_{sk}$ (Z samples). ....	44
Fig. 4-45: Pore pressure increment for different $B_{sk}$ (Z samples). ....	45
Fig. 4-46: Verification of $B_{sk}$ for cases using different $B_{sk}$ (Z samples). ....	45

Fig. 4-47:	Stress-strain curve for different $B_{sk}$ (P samples).	47
Fig. 4-48:	Pore pressure increment for different $B_{sk}$ (P samples).	48
Fig. 4-49:	Verification of $B_{sk}$ for cases using different $B_{sk}$ (P samples).	48
Fig. 4-50:	Stress-strain curve for different $B_{sk}$ (S samples).	49
Fig. 4-51:	Pore pressure increment for different $B_{sk}$ (S samples).	49
Fig. 4-52:	Verification of $B_{sk}$ for cases using different $B_{sk}$ (S samples).	50
Fig. 4-53:	Stress-strain curve for different $B_{sk}$ (X samples).	50
Fig. 4-54:	Pore pressure increment for different $B_{sk}$ (X samples).	51
Fig. 4-55:	Verification of $B_{sk}$ for cases using different $B_{sk}$ (X samples).	51
Fig. 5-1:	Comparison of stress-strain evolution between FLAC3D and laboratory experiments for P samples (stiff parameter set).	54
Fig. 5-2:	Matrix plastic shear strain at the end of the test for P samples (stiff parameter set).	55
Fig. 5-3:	Pore pressure increments comparison between FLAC3D and laboratory experiments for P samples (stiff parameter set).	55
Fig. 5-4:	Volumetric strain and pore pressure for P samples (stiff parameter set) YZ cutting plane shown.	56
Fig. 5-5:	Comparison of $B_{sk}$ between FLAC3D and laboratory experiments for P samples (stiff parameter set).	56
Fig. 5-6:	Comparison of stress-strain evolution between FLAC3D and laboratory experiments for S samples (stiff parameter set).	57
Fig. 5-7:	Matrix plastic shear strain at the end of the test for S samples (stiff parameter set).	57
Fig. 5-8:	Pore pressure increments comparison between FLAC3D and laboratory experiments for S samples (stiff parameter set).	58
Fig. 5-9:	Volumetric strain and pore pressure for S samples (stiff parameter set) . YZ cutting plane shown.	58
Fig. 5-10:	Compariosn of $B_{sk}$ between FLAC3D and laboratory experiments for S samples (stiff parameter set).	59
Fig. 5-11:	Comparison of stress-strain evolution between FLAC3D and laboratory experiments for X samples (stiff parameter set).	59
Fig. 5-12:	Bedding plastic shear strain at the end of the test for X samples (stiff parameter set).	60
Fig. 5-13:	Pore pressure increments comparison between FLAC3D and laboratory experiments for X samples (stiff parameter set).	60

Fig. 5-14:	Volumetric strain and pore pressure for X samples (stiff parameter set). YZ cutting plane shown. ....	61
Fig. 5-15:	Comparison of $B_{sk}$ between FLAC3D and laboratory experiments for X samples (stiff parameter set). ....	61
Fig. 5-16:	Comparison of stress-strain evolution between FLAC3D and laboratory experiments for Z samples (stiff parameter set). ....	62
Fig. 5-17:	Bedding plastic shear strain at the end of the test for Z samples (stiff parameter set). ....	62
Fig. 5-18:	Pore pressure increments comparison between FLAC3D and laboratory experiments for Z samples (stiff parameter set). ....	63
Fig. 5-19:	Volumetric strain and pore pressure for Z samples (stiff parameter set). YZ cutting plane shown. ....	63
Fig. 5-20:	Comparison of $B_{sk}$ between FLAC3D and laboratory experiments for Z samples (stiff parameter set). ....	64
Fig. 5-21:	Comparison of stress-strain evolution between FLAC3D and laboratory experiments for S samples. ....	65
Fig. 5-22:	Matrix plastic shear strain at the end of the test for S samples (soft parameter set). ....	66
Fig. 5-23:	Pore pressure increments comparison between FLAC3D and laboratory experiments for S samples. ....	66
Fig. 5-24:	Volumetric strain and pore pressure for S samples (soft parameter set). YZ cutting plane shown. ....	67
Fig. 5-25:	Comparison of $B_{sk}$ between FLAC3D and laboratory experiments for S samples (soft parameter set). ....	67
Fig. 5-26:	Comparison of stress-strain evolution between FLAC3D and laboratory experiments for P samples. ....	68
Fig. 5-27:	Pore pressure increments comparison between FLAC3D and laboratory experiments for P samples. ....	68
Fig. 5-28:	Comparison of stress-strain evolution between FLAC3D and laboratory experiments for X samples. ....	69
Fig. 5-29:	Bedding plastic shear strain at the end of the test for X samples (soft parameter set). ....	69
Fig. 5-30:	Pore pressure increments comparison between FLAC3D and laboratory experiments for X samples. ....	70
Fig. 5-31:	Comparison of stress-strain evolution between FLAC3D and laboratory experiments for Z samples. ....	70
Fig. 5-32:	Pore pressure increments comparison between FLAC3D and laboratory experiments for Z samples. ....	71
Fig. 5-33:	Shear bands formation for P samples. ....	72
Fig. 5-34:	Shear bands formation for S samples. ....	73

Fig. 5-35:	Shear bands formation for X samples.....	74
Fig. 5-36:	Shear bands formation for Z samples. ....	75
Fig. 5-37:	Example of kink band formation orthogonal to the main slip direction. ....	76
Fig. 5-38:	Stress –strain curve for P samples using roller and fixed boundary (P samples). ....	77
Fig. 5-39:	Minor principal stress tensor (compression) just after reaching peak strength (P115). ....	77
Fig. 5-40:	Pore pressure increment for samples using roller and fixed boundary (P samples). ....	78
Fig. 5-41:	Pore pressure just after reaching peak strength (P115).....	78
Fig. 5-42:	$B_{sk}$ for samples using roller and fixed boundary (P samples).....	79
Fig. 5-43:	Comparison of plastic shear strain with roller and fixed boundary. ....	79
Fig. 5-44:	Stress –strain curve for samples using roller and fixed boundary (X samples). ....	80
Fig. 5-45:	Pore pressure increment for samples using roller and fixed boundary (X samples). ....	80
Fig. 5-46:	Comparison of $B_{sk}$ for samples using roller and fixed boundary (X samples). ....	81
Fig. 5-47:	Plastic shear strain at the end of the test (X24).....	81
Fig. 5-48:	Maximum shear strain and displacement vector for samples using different bedding orientation. ....	83
Fig. 5-49:	Plastic shear strain for samples using different bedding orientation. ....	84
Fig. 5-50:	Schematic of localization using subiquitous joint model. ....	84
Fig. A1:	Failure criterion in principal stress plane (Matrix). ....	A-2
Fig. A2:	Failure criterion in component parallel ( $\tau$ ) and perpendicular ( $\sigma_{33}$ ) to the weak plane (Bedding). ....	A-3
Fig. B1:	Strain dependency to the mesh discretization.....	A-1



## 1 Introduction

As part of a geomechanical testing program of cores recovered from the geothermal well of Schlattingen-1, Nagra recently conducted a large number of undrained triaxial tests on Opalinus Clay samples (Jahns 2013). The experimental findings are in qualitative agreement with previously reported characteristics of the mechanical behaviour of intact Opalinus Clay rock samples (Nagra 2002). These characteristics comprise of a distinct strain softening and anisotropy in elastic and strength properties, complex non-saturated and moderate swelling behaviour. Based on the relatively strong localization of deformation and pronounced brittleness under in-situ stress conditions, a bi-linear Mohr-Coulomb constitutive model with a tension cut-off is considered appropriate to represent failure behaviour.

ITASCA consultants was requested by Nagra to numerically reproduce a selection of the laboratory tests reported in Jahns (2013) using FLAC3D software with the bilinear constitutive model and an updated geomechanical parameter set for Opalinus Clay. The numerical simulations are conducted to assess the suitability of the modelling approach in reproducing experimental results at the sample scale. In addition, the study investigates the relative impact of different parameters on strength evolution. This is of particular interest for parameters such as hydromechanical coupling parameters (Biot alpha and Skempton-B values), which are notoriously difficult to constrain for low-permeability claystones in the laboratory.

The calibration work is separated in two parts. Simulations are first conducted to calibrate parameters related to softening behavior (Task 1) documented in Chapter 4.1. Based on results obtained, a second batch of simulations is then performed, to calibrate the hardening behaviour and investigate the effect of dilation angle and hydromechanical coupling parameters (Chapter 4.2 to 4.4) (Task 2). Following the calibration and parameter study in Chapter 4, numerical results are then compared to results from laboratory experiments in Chapter 5.



## 2 Experimental data base

### 2.1 Sample description and orientation convention

The Opalinus Clay in the Schlattingen-1 borehole in northeastern Switzerland was recovered from a depth of between approximately 830 m and 950 m below ground (Albert et al. 2012). For the undrained triaxial testing program, plugs of 50.8 mm length and 25.4 mm diameter were prepared. The plugs were drilled in four different directions with respect to the dominant fabric or 'bedding' (Fig. 2-1):

- P direction: plug long axis parallel (0°) to bedding
- X direction: plug long axis 30° to bedding
- Z direction: plug long axis 45° to bedding
- S direction: plug long axis perpendicular (90°) to bedding

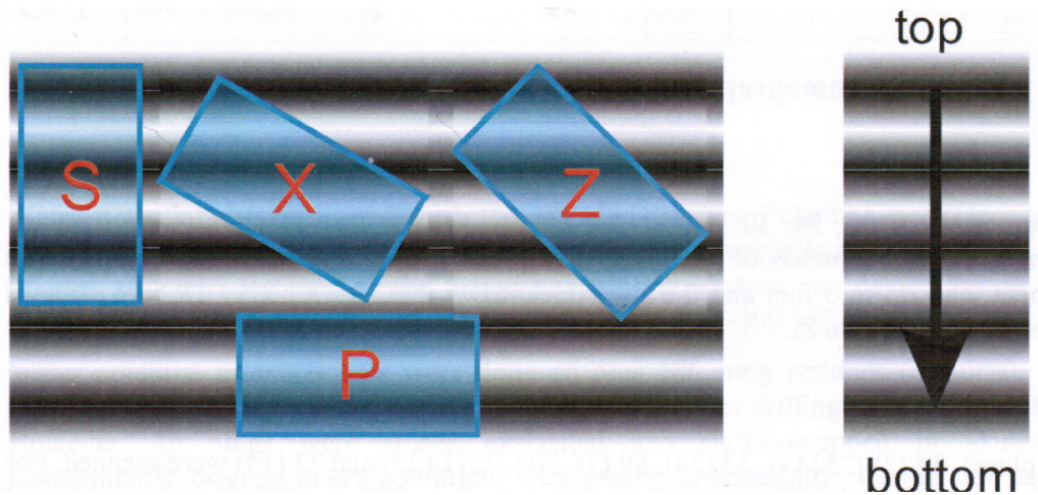


Fig. 2-1: Plug orientation with respect to bedding (indicated by horizontal lines).

From Jahns (2013).

### 2.2 Triaxial experimental data

The experimental triaxial test procedure is described in Jahns (2013). The sample is first loaded at isotropic confining stress by ramping up pore fluid pressure and holding the ratio between confining and fluid pressure constant at a value of 2.5. After a period of pressure equilibrating lasting typically a few days and up to two weeks, a single stage triaxial test was performed (at a strain rate of typically  $10^{-6}\text{s}^{-1}$ ):

- Step 1: The axial deformation is applied until the stress-strain curve turns to be linear.
- Step 2: The sample undergoes an unload-reload path. This allows the measurement of the Young's Modulus, according to ASTM 2010.
- Step 3: Axial loading is then continued until failure.
- Step 4: After failure detection, the sample is deformed axially until approximately 0.5% shear strain is reached to determine the residual strength.
- Step 5: A post failure hysteresis is conducted in the same manner as step 2.

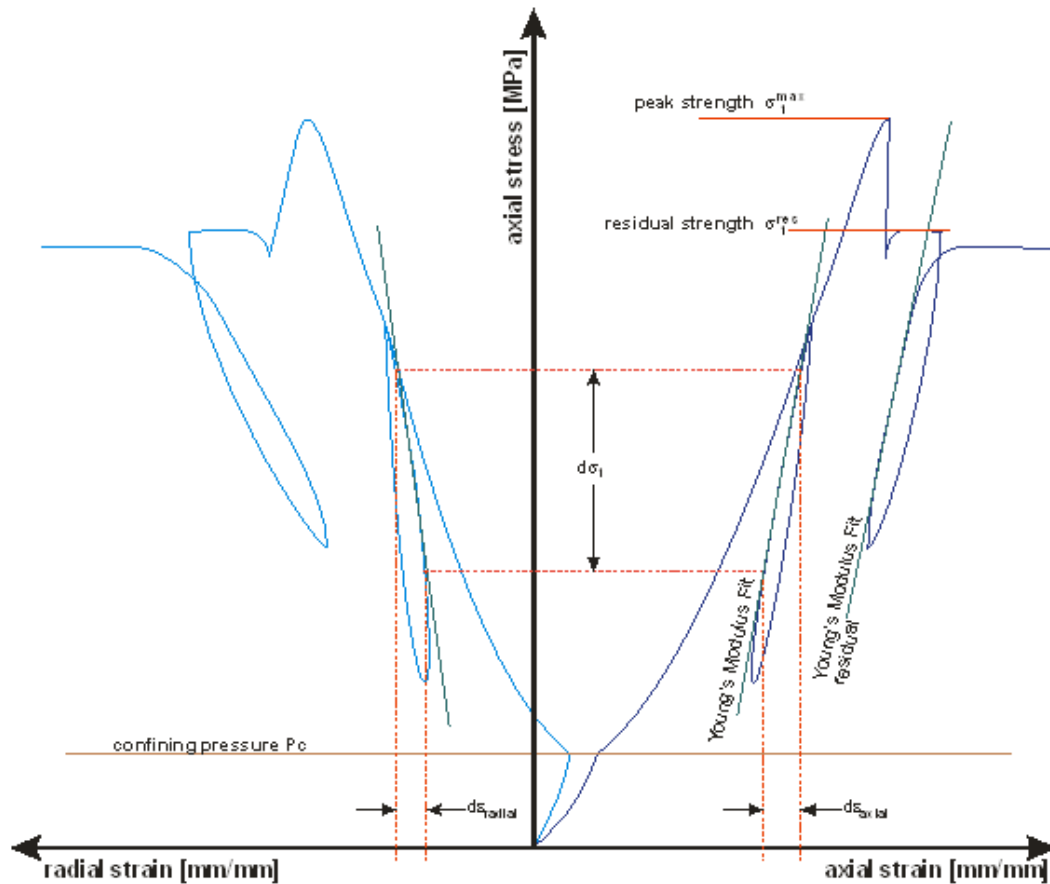


Fig. 2-2: Important parameters of a single stage triaxial test with brittle failure. According to ASTM 2010 (so called Harvestman Diagram). Figure from Jahns (2013).

Nagra has selected a number of tests from Jahns (2013) to be reproduced in this current study (Table 2-1). Material properties interpreted from the laboratory tests are summarized in Table 2-2. It is noted that the data set listed in Table 2-2 represent a preliminary analysis of geomechanical properties of Opalinus Clay based on laboratory tests from cores of the borehole Benken (Nagra 2001) and Schlattingen-1 (Ferrari et al. 2012; Jahns 2013). For cohesion and internal friction angle, two values are reported in the Table 2-2. They denote respectively values of the first segment and the second segment for the bilinear law of Strain hardening/softening, Ubiquitous-joint, Bilinear model, or "SUBI model". A detailed description of the SUBI model is given in Appendix A.

Tab. 2-1: Test conditions and results of selected laboratory tests from Jahns (2013).

<i>P sample</i>	Confinement (MPa)	Pore Pressure (MPa)	E-Modul initial (GPa)	E-Modul residual (GPa)	Sigma peak (MPa)	Sigma residual (MPa)	Poisson ratio
<b>P115</b>	<b>7.61</b>	<b>3.04</b>	<b>13.8</b>	<b>11.9</b>	<b>38.4</b>	<b>29.3</b>	<b>0.46</b>
<b>P109</b>	<b>12.61</b>	<b>5.04</b>	<b>15.4</b>	<b>13.0</b>	<b>52.3</b>	<b>33.1</b>	<b>0.15</b>
<b>P14</b>	<b>22.61</b>	<b>9.04</b>	<b>20.7</b>	<b>16.8</b>	<b>76.4</b>	<b>48.6</b>	<b>0.53</b>
<i>S sample</i>							
<b>S106</b>	<b>7.61</b>	<b>3.04</b>	<b>7.8</b>	<b>6.2</b>	<b>33.0</b>	<b>21.5</b>	<b>0.30</b>
<b>S03</b>	<b>12.61</b>	<b>5.04</b>	<b>6.2</b>	<b>5.7</b>	<b>30.2</b>	<b>28.3</b>	<b>0.32</b>
<b>S102</b>	<b>22.61</b>	<b>9.04</b>	<b>9.5</b>	<b>7.2</b>	<b>54.7</b>	<b>44.9</b>	<b>0.34</b>
<i>X sample</i>							
<b>X24</b>	<b>7.6</b>	<b>3.04</b>	<b>9.9</b>	<b>8.5</b>	<b>22.8</b>	<b>17.4</b>	<b>0.34</b>
<b>X25</b>	<b>12.6</b>	<b>5.04</b>	<b>11.3</b>	<b>9.4</b>	<b>35.1</b>	<b>25.9</b>	<b>0.20</b>
<i>Z sample</i>							
<b>Z19</b>	<b>7.61</b>	<b>3.04</b>	<b>9.1</b>	<b>7.8</b>	<b>26.8</b>	<b>21.1</b>	<b>0.60</b>
<b>Z23</b>	<b>22.61</b>	<b>9.04</b>	<b>11.7</b>	<b>7.8</b>	<b>57.3</b>	<b>45.2</b>	<b>0.50</b>

Tab. 2-2: Material properties from laboratory test data provided by Nagra.

Parameter	Unit	Value II bedding	Value I bedding
Bulk density (natural)	[g/cm <sup>3</sup> ]	2.52	
Bulk density (dry)	[g/cm <sup>3</sup> ]	2.43	
Grain density (dry)	[g/cm <sup>3</sup> ]	2.71	
Water content	[vol.%]	4.5	
Physical porosity	[vol.%]	11	
E-Modulus			
Drained (unload-reload cycle)	[GPa]	16	6
Undrained (unload-reload cycle)	[GPa]	20	8
Poisson ratio	[-]	0.27	0.27
Uniaxial Compressive Strength (UCS)	[MPa]	33	31
Uniaxial Compressive Strength – calculated	[MPa]	22	
Uniaxial Tensile Strength (UTS)	[MPa]	1.5	2.5
Mohr-Coulomb shear strength			
Peak strength ( $p' \leq 25$ MPa / $p' > 25$ MPa) $\pm \sigma$			
Matrix – effective cohesion	[MPa]	5.7 / 14.1	
Matrix – effective angle of internal friction	[°]	35 / 18	
Bedding – effective cohesion		4.1 / 7.6	
Bedding – effective angle of internal friction		24 / 17	
Residual strength $\pm 2 \sigma$			
Matrix – effective cohesion	[MPa]	3.1 / 8.1	
Matrix – effective angle of internal friction	[°]	29 / 19	
Bedding – effective cohesion		1.8 / 5.4	
Bedding – effective angle of internal friction		24 / 17	
Dilatancy angle	[°]	0	
Biot coefficient (alpha)			
Reference value	[-]	0.8	

### 3 Model description

#### 3.1 Numerical sample

The numerical sample reproduces the geometry used for the laboratory experiments: cylindrical shape with 25.4 mm width and 50.8 mm length (Figure 3-1). The bedding plane orientation is illustrated in Figure 3-2. The mesh is designed to minimize meshing effects on localization processes.

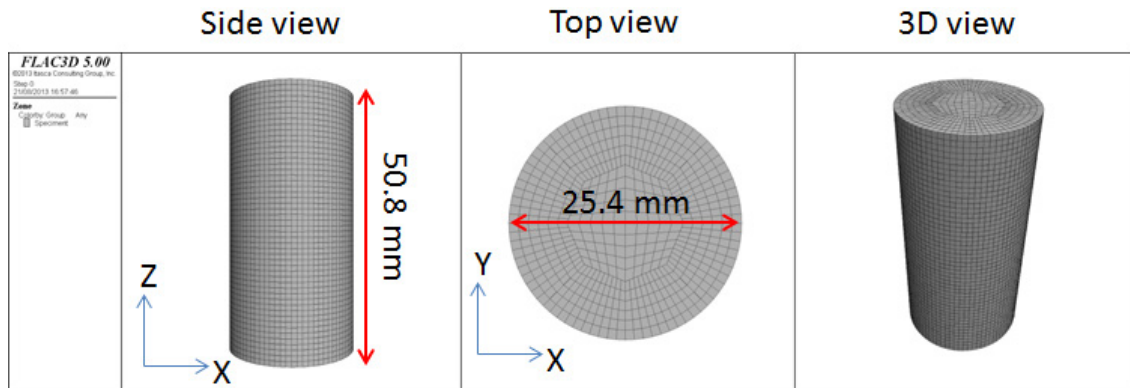


Fig. 3-1: Layout of the numerical sample.

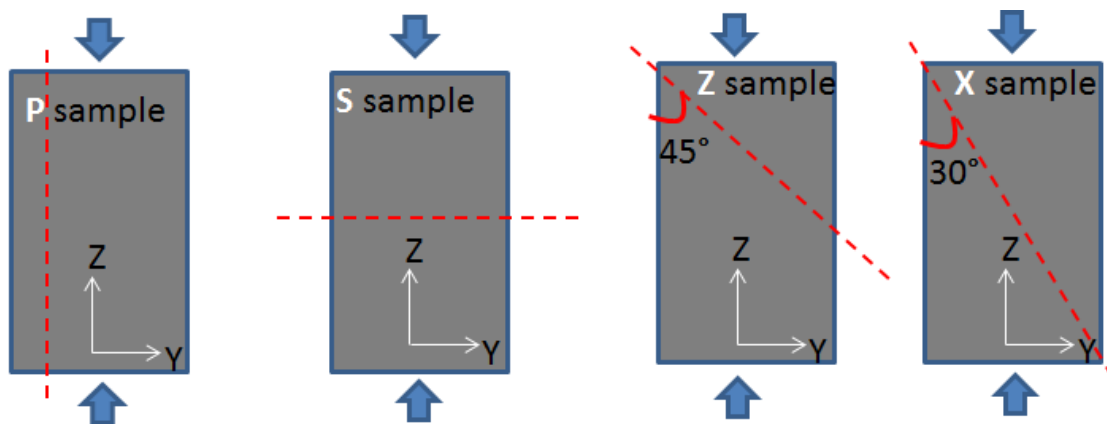


Fig. 3-2: Bedding plane orientation for numerical samples (dashed line).

#### 3.2 Model setup

The numerical model consists of reproducing the selected experimental triaxial tests provided in Table 2-1. The standard loading process follows two steps: isotropic loading (pore pressure and confining stress) to specified confining stress and deviatoric loading during deformation. For the numerical simulation, the end of the isotropic loading step is treated as the initial condition and consolidation is assumed to be in equilibrium with the applied stress field. In other words, the initial stresses in each zone are set equal to the target confinement stress. The pore pressure can be assigned in the same manner (see Figure 3-3).

During deviatoric loading, grid points located at the top surface and at the bottom surface are subjected to a constant vertical velocity. Stress conditions are applied on the vertical faces. Thus, the radial confinement pressure is kept constant during the simulation. Strains and stresses are recorded during the test. The locations of history recorders are illustrated in Figure 3-5. The pore pressure increment is also recorded and is calculated as the mean pore pressure for all zones in the model.

The stress-strain path is controlled in a way similar to the one used for laboratory experiments:

- The sample is loaded until failure. The maximum stress is recorded frequently during the test, and failure is detected if the maximum stress starts diminishing.
- After the failure, the sample is loaded with sufficient axial strain to reach its residual strength (the strain increment is fixed at 0.3% for this study).
- Following the previous step, the post failure hysteresis is triggered. This is done by inducing the same strain increment along unloading and reloading path.
- The sample is finally reloaded to reach its residual strength.

The initial hysteresis step is not reproduced in the numerical model since the strain-stress curve is perfectly reversible during elastic loading.

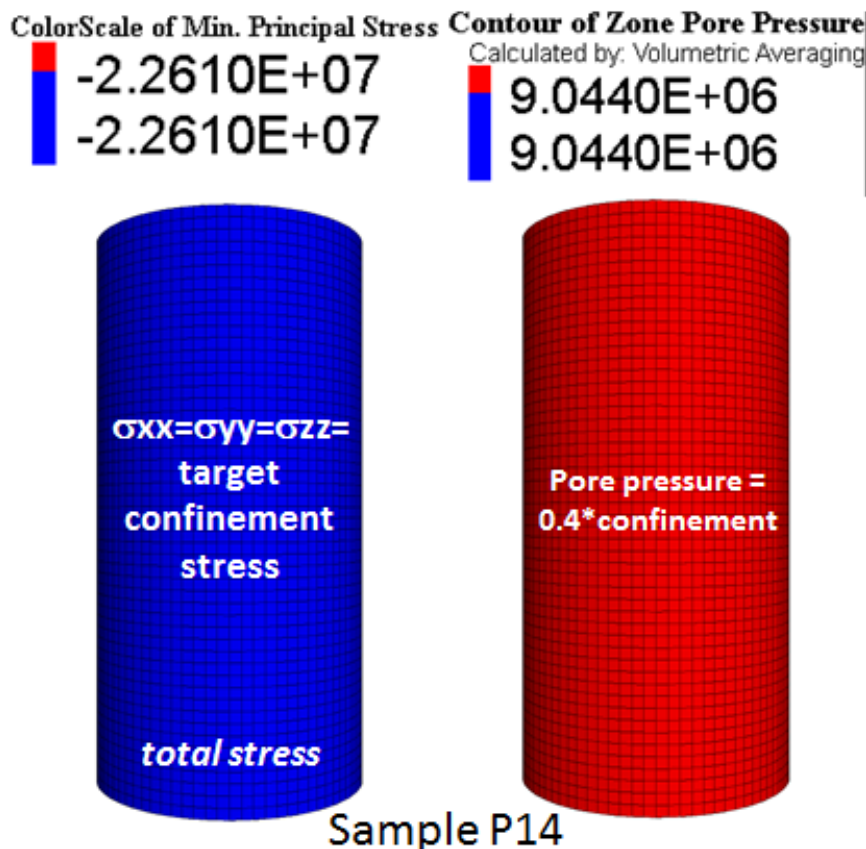


Fig. 3-3: Stresses and pore pressure initialization.

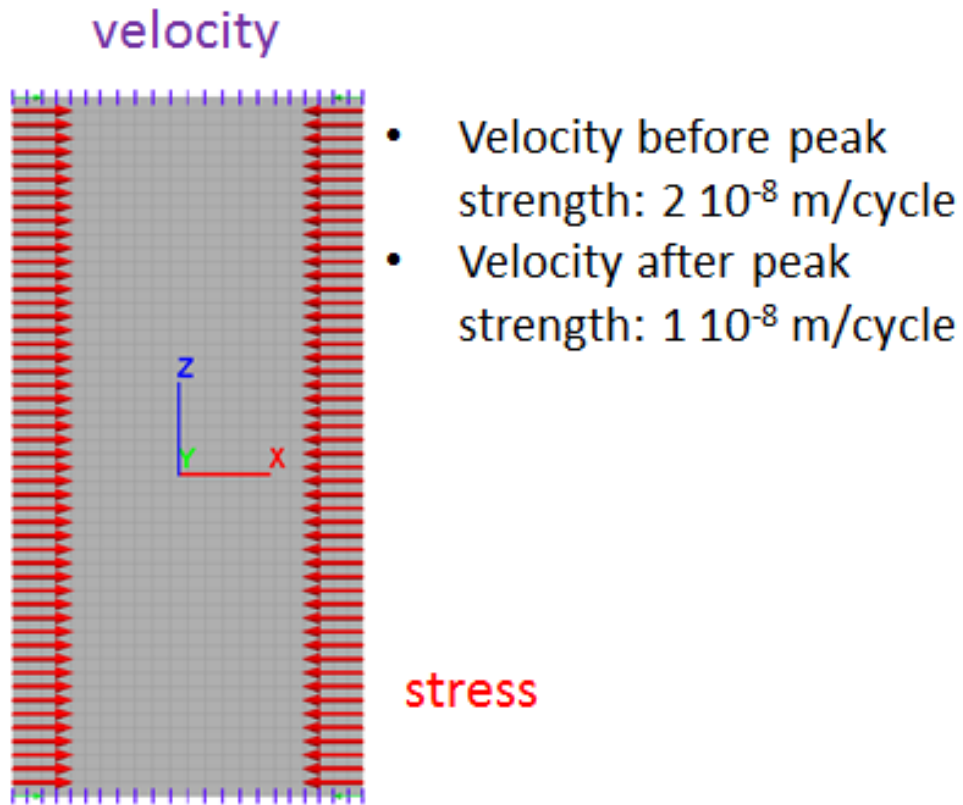


Fig. 3-4: Velocity boundary condition for top and bottom zones, stress boundary condition for lateral zones.

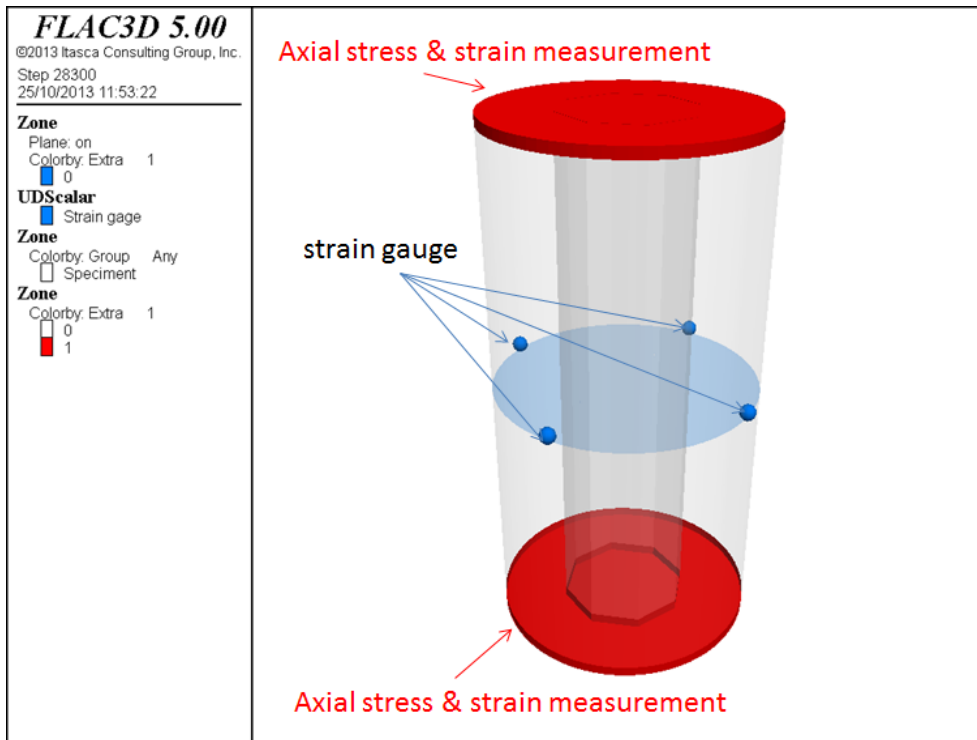


Fig. 3-5: Strain and stress measurements during numerical triaxial simulation.

### 3.3 Choice of Poroelastic parameters for the model

Selected elastic parameters are reported in Table 3-1. According to the experimental measurements (Table 2-1), the Young's modulus varies from 6.2 GPa (S03) to 20.7 GPa (P14). However, the change in Young's modulus while changing the confinement pressure is not reproduced in the numerical simulations. Thus, the Young's modulus is fixed at a "reference value" for all the numerical tests. The reference Young's modulus (12 GPa) is chosen to fit the initial stress-strain curve for P samples.

The Biot modulus is calculated using the following equation:

$$M = \frac{K_u - K_d}{\alpha^2} \quad (\text{Eq 3-1})$$

With  $K_u$  the undrained bulk modulus,  $K_d$  the drained bulk modulus and  $\alpha$  the Biot modulus.

No fluid flow step is performed in the numerical simulation. However, changes in volumetric strain induce changes in pore pressure. The initial pore pressure is set at 40% of the confinement pressure.

Tab. 3-1: Poroelastic parameters.

Young's modulus	12 GPa
Poisson ration	0.27
Biot coefficient, $\alpha$	0.8
Biot modulus, $M$	3.4 GPa

### 3.4 Parametric study scope

The objective of this work is to better understand the mechanical behavior of the material subjected to triaxial loading. Numerous simulations are carried out using different parameter sets (i.e., parametric study). The studied parameters are discussed below:

#### Task 1:

- **Softening behavior of the strength parameters:** As shown in Figure 3-6, the softening behavior is controlled by plastic shear strain. When the material undergoes plastic (shear) strain, the material strength (cohesion and internal friction angle) reduces from its peak value until it reaches a residual value. The strain at which the residual value is reached is called the "critical plastic shear strain". It is named "critical strain" throughout this report.
- Eight critical strains are needed:  $\gamma_{mc1}$ ,  $\gamma_{mc2}$ ,  $\gamma_{jc1}$  and  $\gamma_{jc2}$  for critical strain related to cohesion, respectively  $\gamma_{mf1}$ ,  $\gamma_{mf2}$ ,  $\gamma_{jf1}$  and  $\gamma_{jf2}$  for critical strain related to the internal friction angle. Indices  $m$ ,  $j$ ,  $c$  and  $f$  denote respectively *Matrix*, *Bedding*, *Cohesion* and *internal Friction* angle. The indices  $1$  and  $2$  denote parameters for the first segment and for the second segment of the bilinear law.

- It is further supposed that the cohesion and the friction angle in a given material segment are limited by the same critical strain (i.e.:  $\gamma_{mc1} = \gamma_{mf1}$ ). This reduces the number of softening parameters from 8 to 4. Note that when testing various critical strains, the values of cohesion and internal friction angle remain unchanged. Their values are the ones reported in Table 2-2 (for both peak and residual values). The SUBI (strain-hardening/softening ubiquitous-joint bilinear) model is described in Appendix A.

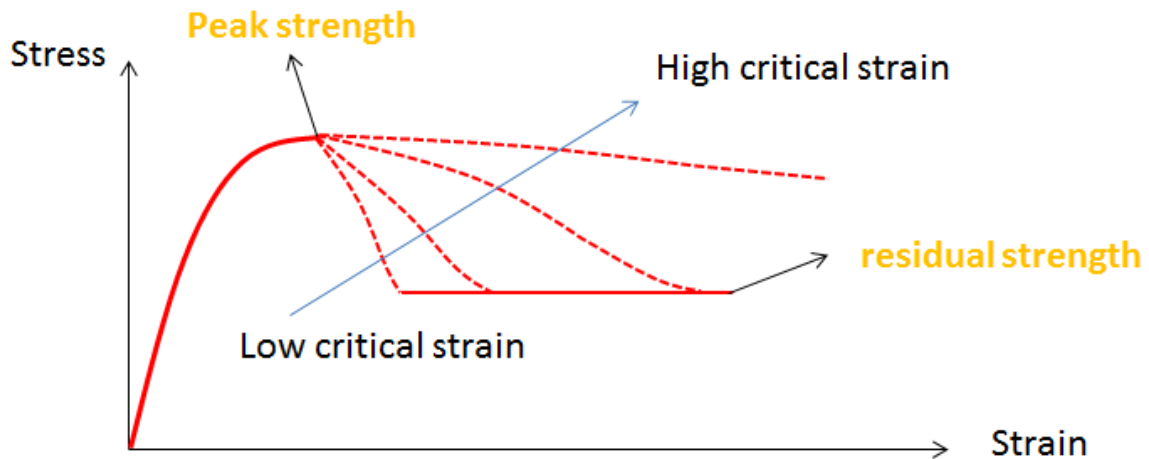


Fig. 3-6: Softening behavior as function of the critical strain.

### Task 2:

- **Dilation angle.** As for the critical strain, eight parameters are needed (4 for matrix and 4 for bedding). In order to simplify the parametric study, the 8 dilation angles for a given case are set at the same value. Simulations with zero dilation angles and with non-zero dilation angles are compared.
- **Hardening (pre-peak) behavior.** Adding hardening before the peak yields a better fit of pre-peak strain-stress curves. Note that the peak strength parameter values remain unchanged.
- Influence of the Biot coefficient ( $\alpha$ ) and the Skempton B coefficient ( $B_{sk}$ ). A detailed description is given in Section 4.4.



## 4 Results and discussions

### 4.1 Investigation of softening behavior

In order to define a reasonable range for the critical strain (cf. Chapter 3.4), a pre-calibration work is done using a FLAC2D model. The initial trial value (for the critical strain) is estimated as the strain increment induced in the experimental curve by the change of stress when it is reduced from peak to residual. This gives the total strain increment. The plastic strain increment is supposed to stay in the same order of magnitude. The obtained values are reported in Table 4-1, and serve as our "reference case". Further sensitivity analyses are then carried out by changing one parameter at a time. Thereafter, results are compared, in terms of stress-strain curve, with the ones obtained in the reference case.

In order to take into account the influence of the mesh discretization on the softening behavior, a regularization rule is used in the numerical model. A reference mesh size ( $L$ ) is defined. The calibrated critical strain is then applied in zones of size  $L$ . The critical strain  $\gamma_l^{res}$  in a zone of size  $l$  is then given by:

$$\gamma_l^{res} = \gamma_{ref}^{res} \cdot \left( \frac{L}{l} \right) \quad (\text{Eq 4-1})$$

Where  $\gamma_{ref}^{res}$  is the critical strain for zones of size  $L$ . A detailed description of the regularization procedure can be found in Appendix B.

The dilation angle is set to zero for all the parametric runs of the softening behavior.

Tab. 4-1: Residual critical strain (reference case).

parameter	Critical strain
$\gamma_{mc1}, \gamma_{mf1}$	0.02
$\gamma_{mc2}, \gamma_{mf2}$	0.006
$\gamma_{jc1}, \gamma_{jf1}$	0.003
$\gamma_{jc2}, \gamma_{jf2}$	0.003

#### 4.1.1 Critical strain of the cohesion/internal friction angle for matrix

The influence of  $\gamma_{mc1}$  and  $\gamma_{mf1}$  are compared, in terms of the deviatoric stress vs. axial strain curve, from Figure 4-1 to Figure 4-4 for P, S, X and Z samples respectively. For these figures, solid lines represent results of the reference case, while dotted lines are for an alternative case, with a critical strain three times larger than in the reference case. As expected, the model predicts a more ductile response for cases using higher critical strain. Moreover, the critical strains for the first segment ( $\gamma_{mc1}$  and  $\gamma_{mf1}$ ) affect mostly the behavior of samples subjected to lower confinement stresses (P115 and S106). The evolution of deviatoric stress is little changed

for samples where higher confinement stresses are applied (P14 and S102). The change in the critical strain for the matrix has almost no effect on X and Z samples.

The P and S samples behave in a similar fashion – as do the X and Z samples. Thus, only the results for the P samples and of Z samples are presented in further parametric studies. The model behavior of S samples can be inferred from the P sample results, and similarly X sample behavior can be inferred from Z sample results.

Figure 4-5 and Figure 4-6 show the stress –strain curves obtained for two different  $\gamma_{mc2}$  and  $\gamma_{mf2}$  for P and Z samples. The model behavior is similar to the one observed previously. A change in the critical strain for the matrix changes the response of the P samples. The response of the Z samples is unchanged. Also, the increase in  $\gamma_{mc2}$  and  $\gamma_{mf2}$  produces a more ductile behavior for samples with higher confinement pressure (due to the bilinear law).

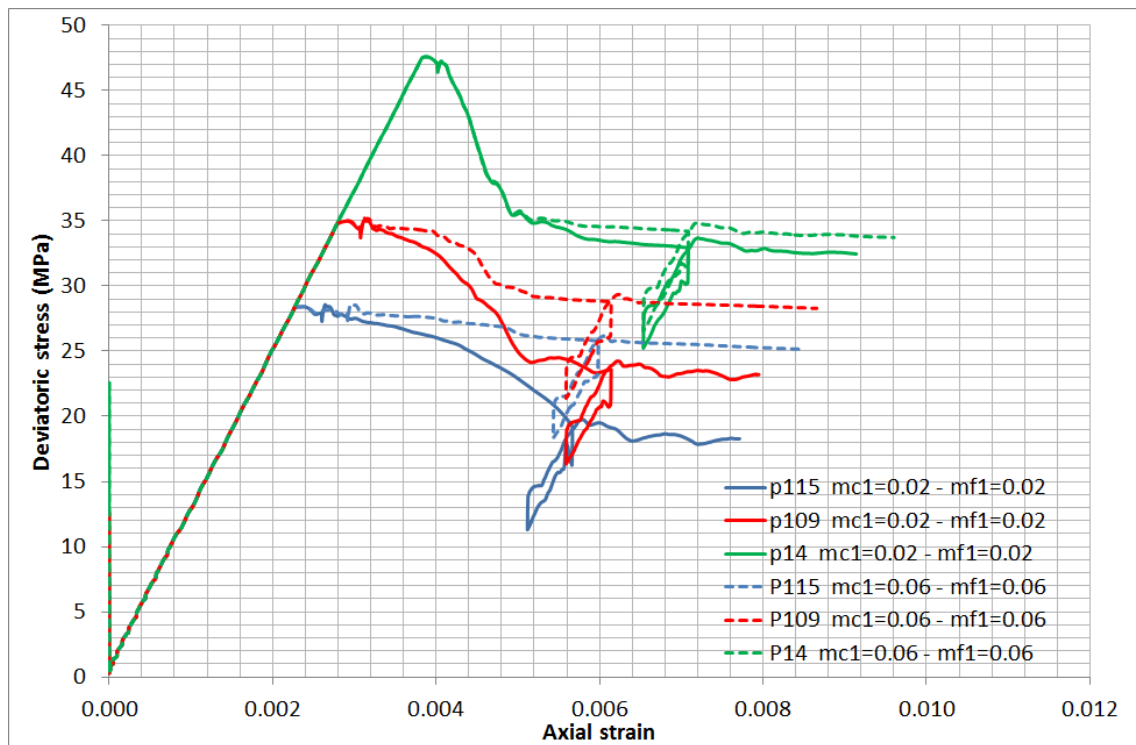


Fig. 4-1: Influence of  $\gamma_{mc1}$  and  $\gamma_{mf1}$  for P samples.

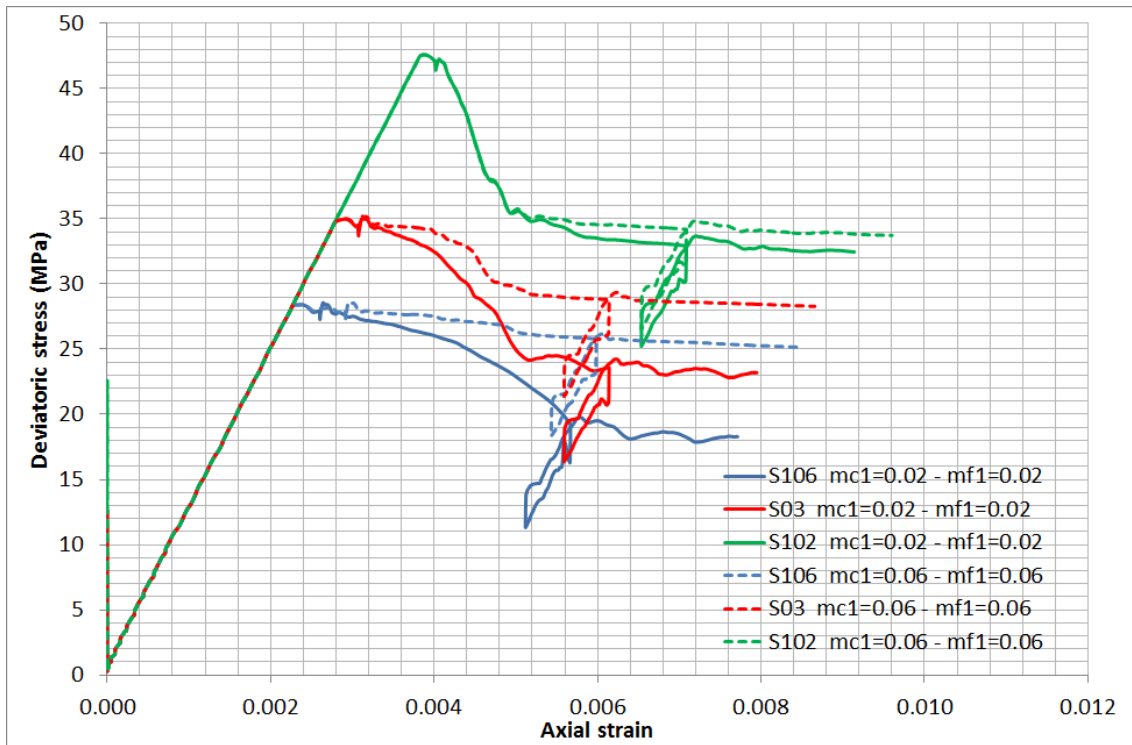


Fig. 4-2: Influence of  $\gamma_{mc1}$  and  $\gamma_{mf1}$  for S samples.

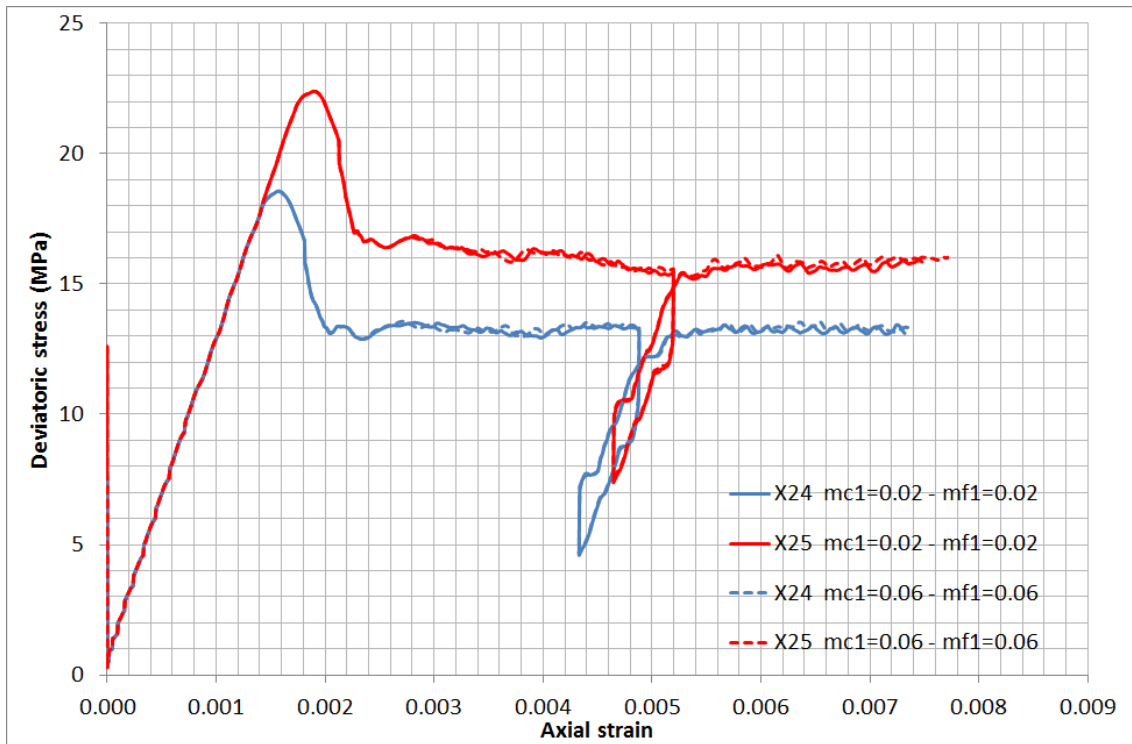


Fig. 4-3: Influence of  $\gamma_{mc1}$  and  $\gamma_{mf1}$  for X samples.

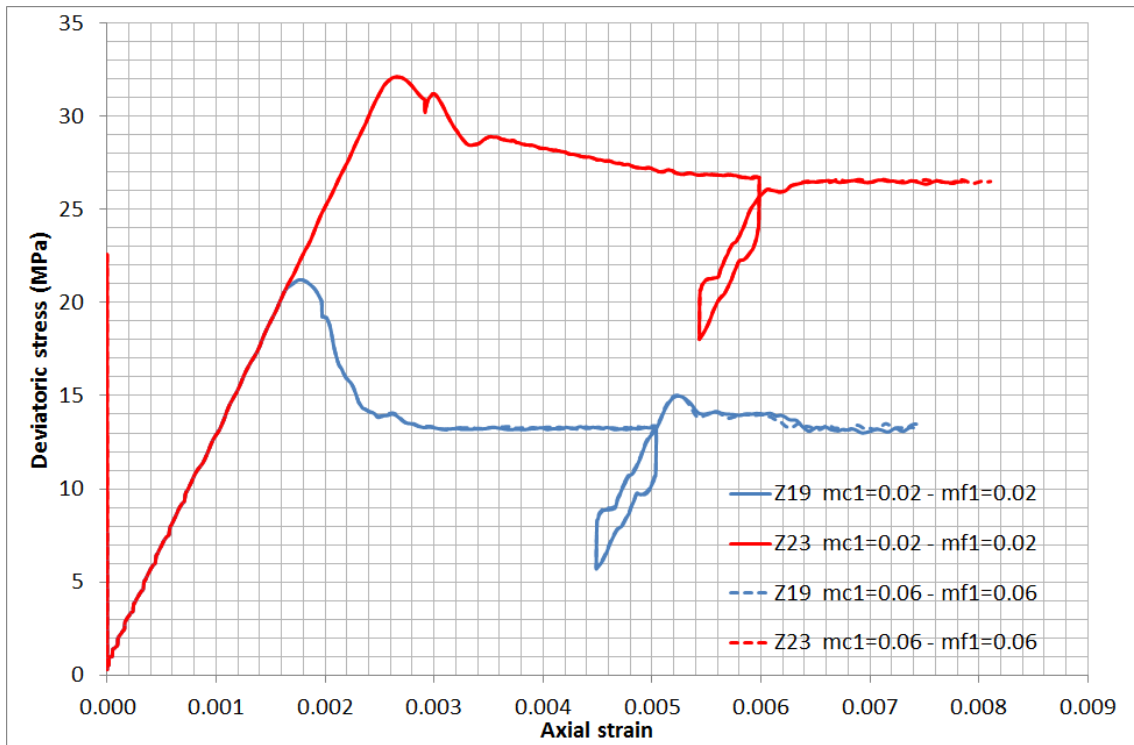


Fig. 4-4: Influence of  $\gamma_{mc1}$  and  $\gamma_{mf1}$  for Z samples.

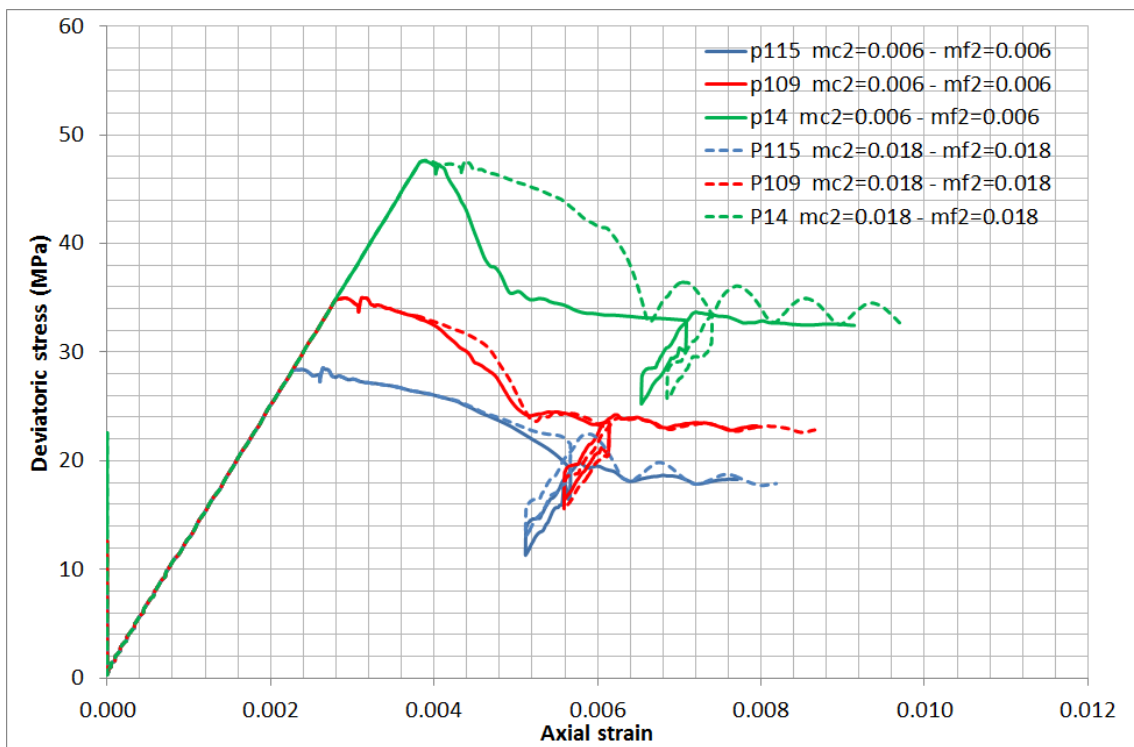


Fig. 4-5: Influence of  $\gamma_{mc2}$  and  $\gamma_{mf2}$  for P samples.

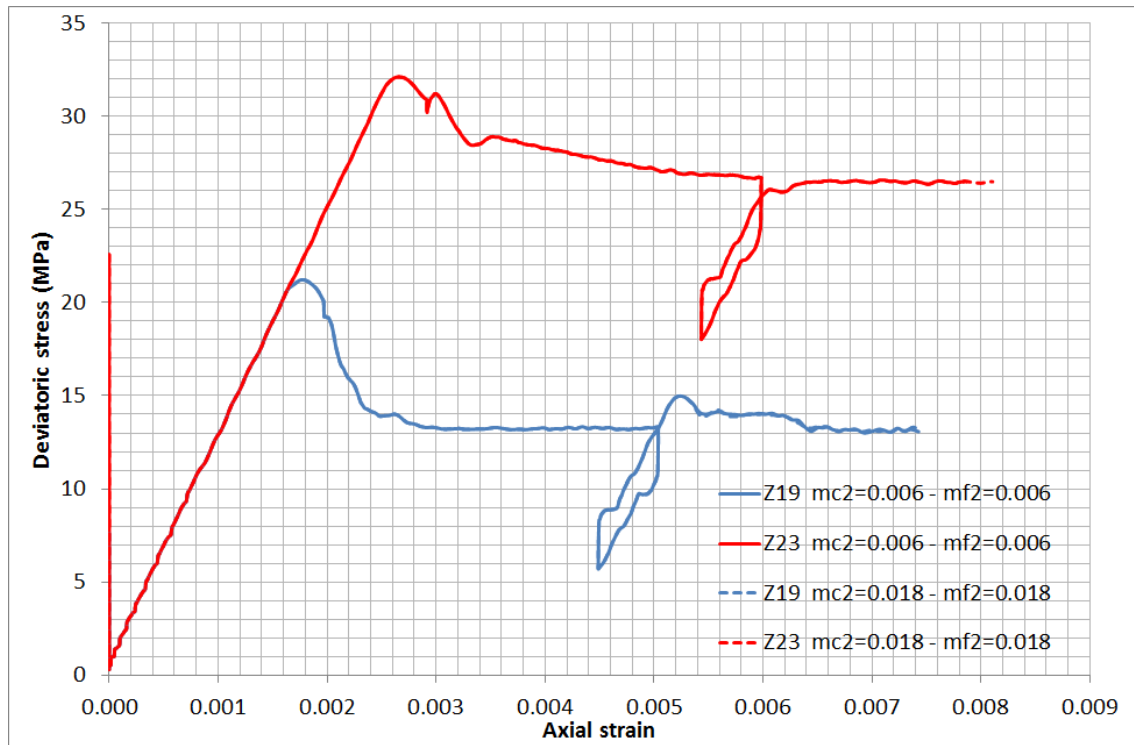


Fig. 4-6: Influence of  $\gamma_{mc2}$  and  $\gamma_{mf2}$  for Z samples.

#### 4.1.2 Critical strain of the cohesion/internal friction angle for bedding

The influence of the critical strain for bedding ( $\gamma_{jc1}$ ,  $\gamma_{jf1}$ ,  $\gamma_{jc2}$  and  $\gamma_{jf2}$ ) on the triaxial behavior is discussed in this section. The critical strains of the parametric cases are set again to three times the values used for the reference case.

Results for the P samples using different  $\gamma_{jc1}$  and  $\gamma_{jf1}$  are presented in Figure 4-7 (respectively in Figure 4-8 for the Z samples). The change in the critical strain for the bedding modifies the behavior of the Z samples (the same change can be expected for the X samples). The model predicts a more ductile behavior for the Z19 sample (7.6 MPa confinement pressure) with a higher critical strain. The stress-strain curve for the Z23 sample (22.6 MPa of confinement pressure) is almost unchanged.

The effect of the critical strain for the second segment is shown in Figure 4-9 and Figure 4-10. The change in  $\gamma_{jc2}$  and  $\gamma_{jf2}$  modifies the stress-strain curve for the Z23 sample, while the stress-strain curve for the Z19 sample stays unchanged. Also, that the critical strain for the bedding has a minor effect on the behavior of the P samples. Thus, a minor effect is also expected for S samples.

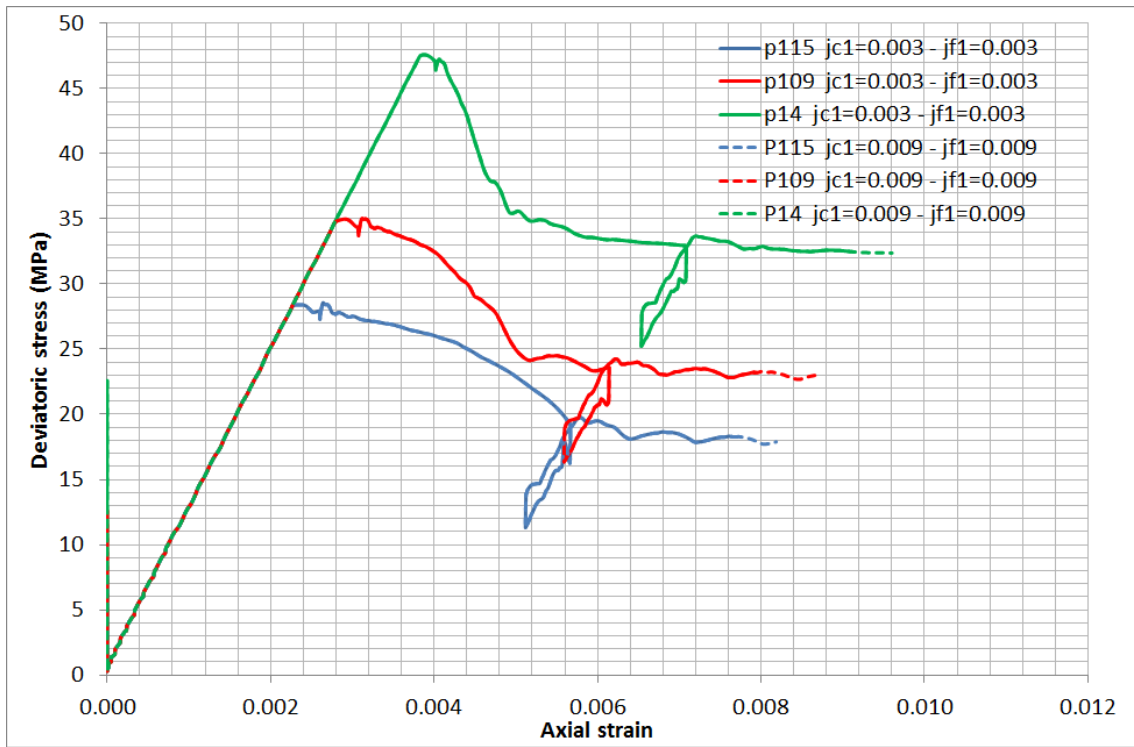


Fig. 4-7: Influence of  $\gamma_{jc1}$  and  $\gamma_{jf1}$  for P samples.

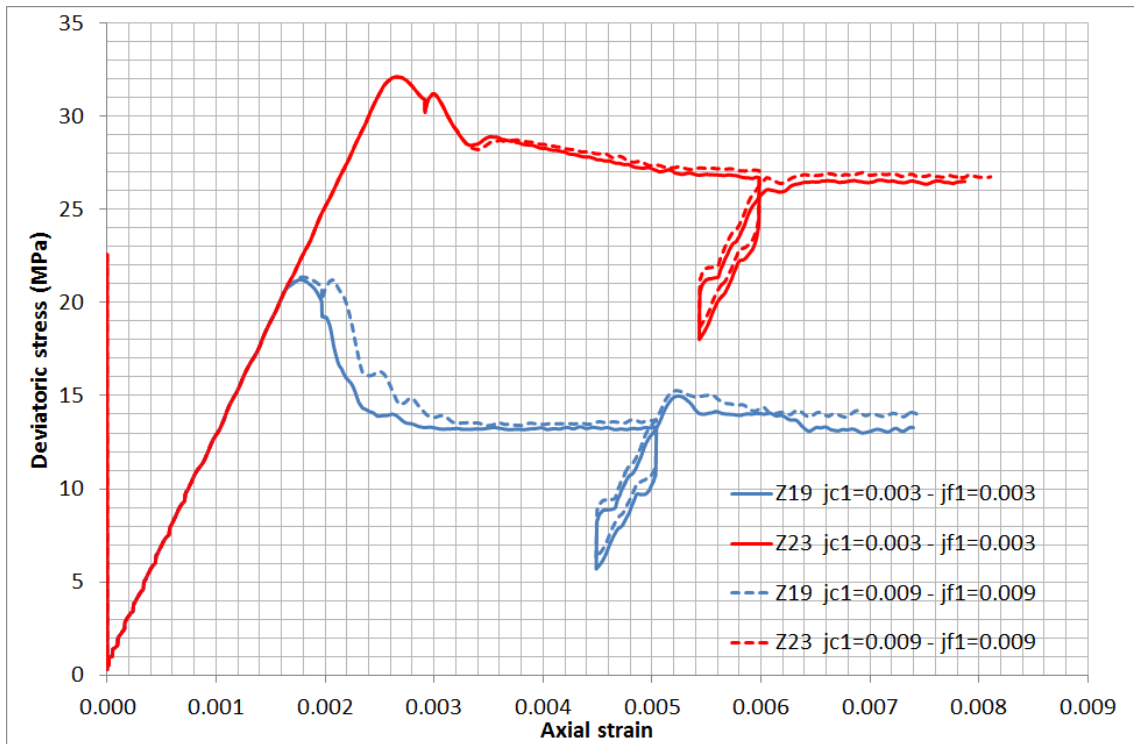


Fig. 4-8: Influence of  $\gamma_{jc1}$  and  $\gamma_{jf1}$  for Z samples.

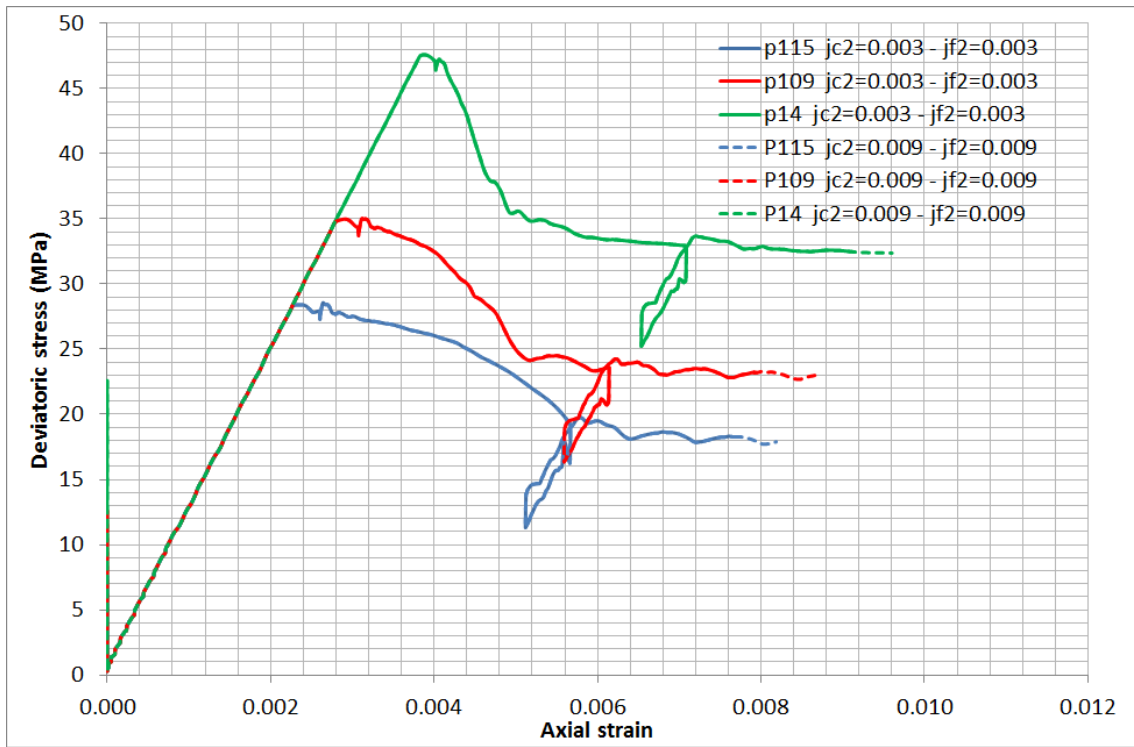


Fig. 4-9: Influence of  $\gamma_{jc2}$  and  $\gamma_{jf2}$  for P samples.

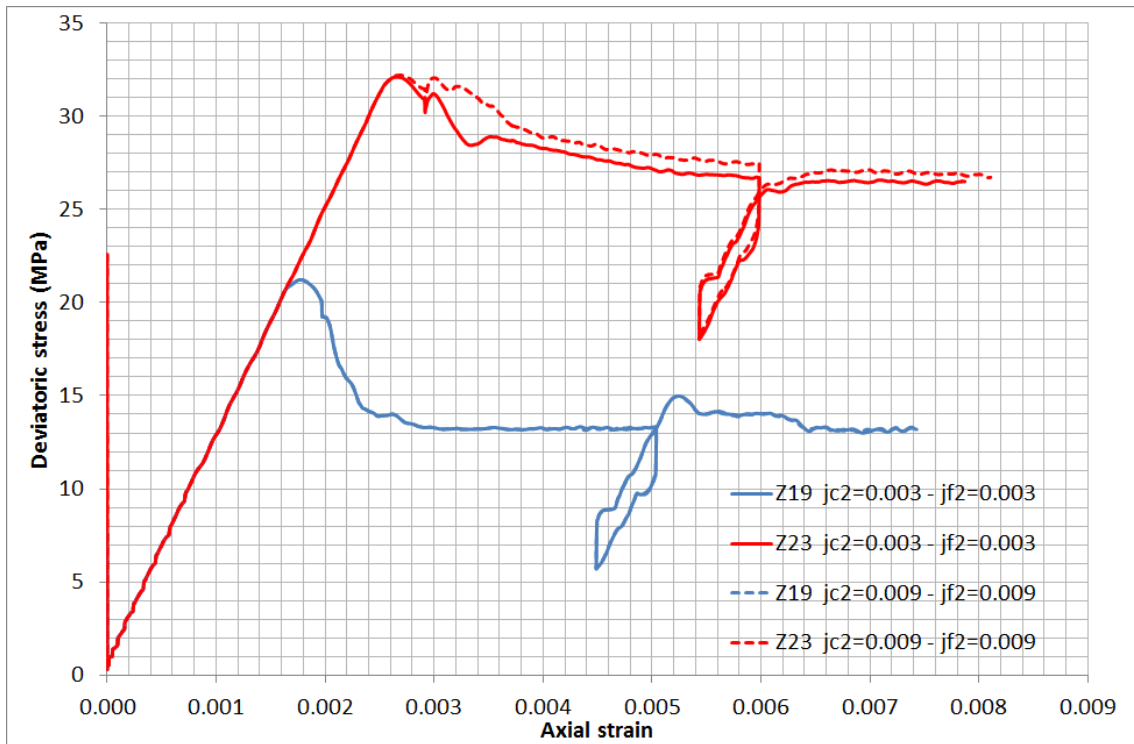


Fig. 4-10: Influence of  $\gamma_{jc2}$  and  $\gamma_{jf2}$  for Z samples.

**4.1.3 Softening behavior – comparison between FLAC3D and experimental data**

According to the results obtained from the sensitivity analyses of the softening parameters, the following remarks are made:

- The parameters of the first segment ( $\gamma_{mc1}, \gamma_{mf1}, \gamma_{jc1}$  and  $\gamma_{jf1}$ ) affect only samples subjected to lower confinement pressures. Similarly, samples subjected to higher confinement pressures are affected by changes in  $\gamma_{mc2}, \gamma_{mf2}, \gamma_{jc2}$  and  $\gamma_{jf2}$ . Thus, it is possible to reproduce the triaxial behavior of samples subjected to different confinement stresses using the bilinear constitutive model. Note that the tested confinements range between 7.6 MPa and 22.6 MPa.
- The SUBI model is used to reproduce the behavior of anisotropic materials containing a plane of weakness. Both matrix and bedding materials are represented by volumetric zones. For each zone, the matrix properties and the bedding properties (cohesion and internal friction angle) can be assigned separately. The numerical results show that a change in matrix critical strain affects only the behavior of P samples and of S samples, while the behaviors of X samples and of Z samples are mostly controlled by the critical strain of the bedding. Thus, calibration can be carried out independently for P and S samples on one side and for Z and of X samples on the other side.

In summary, the triaxial behavior of the Opalinus Clay can be reproduced by the following numerical procedure:

- Calibrate behavior of P and S samples subjected to lower confinement pressure by adjusting  $\gamma_{mc1}$  and  $\gamma_{mf1}$ ;
- Calibrate behavior of P and S samples subjected to higher confinement pressure by adjusting  $\gamma_{mc2}$  and  $\gamma_{mf2}$ ;
- Calibrate behavior of X and Z samples subjected to lower confinement pressure by adjusting  $\gamma_{jc1}$  and  $\gamma_{jf1}$ ;
- Calibrate behavior of X and Z samples subjected to higher confinement pressure by adjusting  $\gamma_{jc2}$  and  $\gamma_{jf2}$ ;

This is summarized in Table 4-2.

Tab. 4-2: Governing parameters for different samples.

	P and S samples	X and Z samples
Low confinement pressure	$\gamma_{mc1}, \gamma_{mf1}$	$\gamma_{jc1}, \gamma_{jf1}$
High confinement pressure	$\gamma_{mc2}, \gamma_{mf2}$	$\gamma_{jc2}, \gamma_{jf2}$

The values used for the reference case (see Table 4-1) were obtained following the previous procedure. The numerical simulations for the reference case are compared with the experimental results from Figure 4-11 to Figure 4-26.

For P samples, the numerical stress-strain curves are comparable with the experimental data. The residual strength is better fitted whereas the numerical results show slightly lower peak strength. The initial slope of the stress-strain curve tends to be stiffer for samples subjected to higher confinement pressure. However, the change in Young's modulus while changing the confinement pressure is not reproduced in the numerical simulations for two reasons:

- The constitutive model does not account for stress-porosity coupling.
- The Young's modulus does not depend on bedding plane orientation since both matrix and bedding are represented by the same volumetric zone. Thus, "contact stiffness" between the matrix and the bedding is omitted.

Shear bands are mainly formed at zones located near the top and the bottom of the sample, dipping approximately 45° degree downward from the horizontal plane.

The pore pressure increment is computed as the mean value for all the zones in the model. The results are compared with experimental data in Figure 4-13. The numerical pore pressure increments stay in the same order as the experimental data. In general, the numerical model predicts higher pore pressures for P samples. Figure 4-14 gives the contours of pore pressure and volumetric strain at the end of the test. As mentioned on these figures, a negative volumetric strain denotes a compacted zone. For the P115 sample, the final pore pressures are higher than their initial value ( $pp = 3$  MPa) since all zones show negative volumetric strains. Moreover, the highest pore pressures are observed in the most compacted zones.

The same plots are presented for S samples from Figure 4-15 to Figure 4-18. The numerical stress-strain curves are different from the experimental ones: the model predicts higher deviatoric stresses (both peak and residual) and lower pore pressures. In fact, the numerical model shows very similar behaviors between P and S samples whereas experimentally they do behave in a different way. When a sample is subjected to axial loading, the Young's modulus tends to minimum for samples with bedding orientation perpendicular to the loading (S sample). The apparent Young's modulus increases when the bedding plane is rotated towards the loading direction, and is maximum when the bedding orientation is parallel to the loading. This is corroborated by the data reported in Table 2-1. Since the Young's modulus in the model is isotropic, and the bedding plane is active only in plasticity, the elastic triaxial behaviors for both P samples and S samples cannot be reproduced correctly using the same parameter set. As long as the Young's modulus is chosen to fit the stress-strain curve for P samples, the S samples behavior produced by the model can be only approximate. A further discussion on this issue is presented in Section 4.4.2, where a lower reference Young's modulus is used (4 GPa instead of 12 GPa).

Results for X samples are presented from Figure 4-19 to Figure 4-22. The stress-strain curve is better reproduced for the X25 sample whereas numerical results show higher strength for the X24 sample. Obvious shear bands are observed for both X24 and X25 samples. The numerical pore pressure increments stay in the same order as the experimental data. The initial pore pressure increment in the experiments varies between the two samples: a smaller initial slope is observed for the X25 sample, although it is subjected to a higher confinement pressure. Figure 4-22 shows volumetric strain and pore pressure contours at the end of the simulation. In order to better visualize the model behavior, only zones with positive volumetric strains (dilated zones) are colored. As a consequence of the dilation effect, the pore pressures in these zones decrease from their initial value. For the X24 sample, negative pore pressures are observed in zones undergoing significant plastic shear strains.

The Z sample models (from Figure 4-23 to Figure 4-26) produce a similar behaviour. Numerical and experimental stress- strain curves remain comparable. For the Z19 sample, clear shear bands develop along the diagonal direction. Positive volumetric strains develop in zones located along the shear bands, yielding a noticeable pore pressure drop in these zones. This explains why in the Z19 sample, the pore pressure tends to decrease after the peak (Figure 4-26).

In this first parametric study, special attention was given on the softening behavior of the numerical samples subjected to triaxial loading. The critical strain, which defines the evolution of material resistance from peak to residual, has been calibrated. Overall, the numerical model shows results comparable with the experimental data, though noticeable discrepancies are observed for the S samples.

In order to improve the model behavior and to better calibrate the model response, further sensitivity analyses are carried out (Task 2), taking into account the following items:

- Use a non-zero dilation angle.
- Add a hardening phase before peak to better reproduce the initial strain-stress curves.
- Check the influence of the Biot coefficient ( $\alpha$ ) and the Skempton B coefficient ( $B_{sk}$ ).

The results of these additional sensitivity analyses are reported in the next sections (from Section 4.2 to Section 4.5).

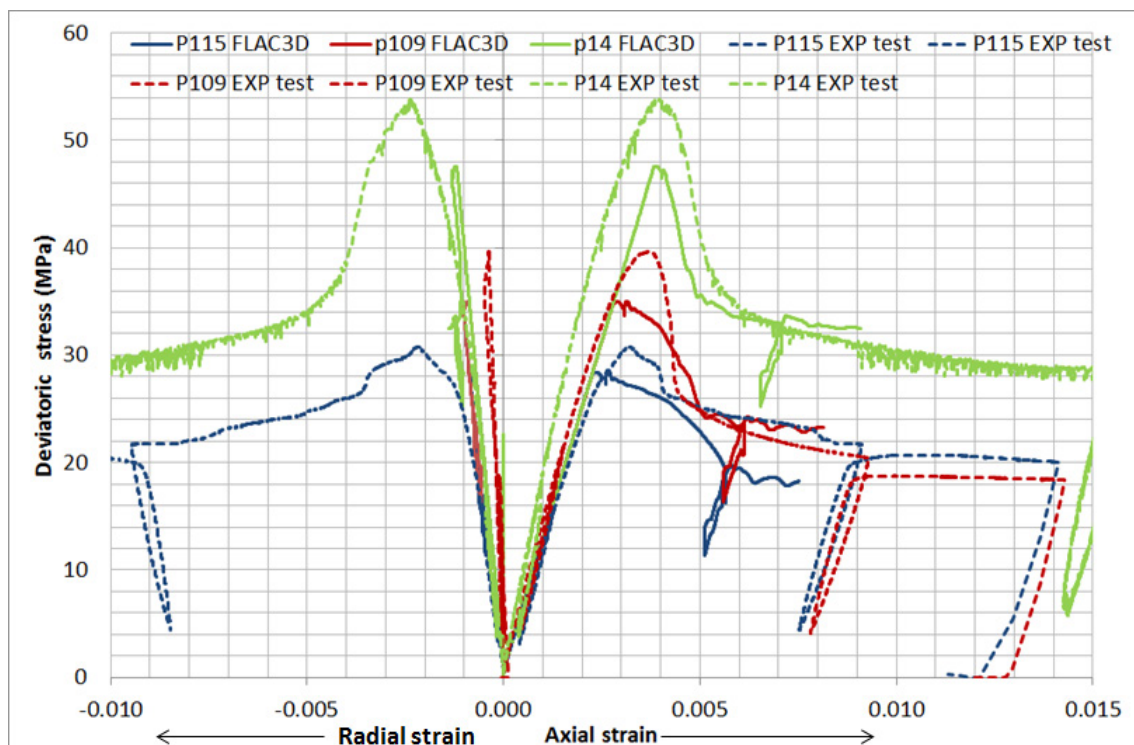


Fig. 4-11: Comparison of stress-strain evolution between FLAC3D (numerical test results) and laboratory experiments for P samples.

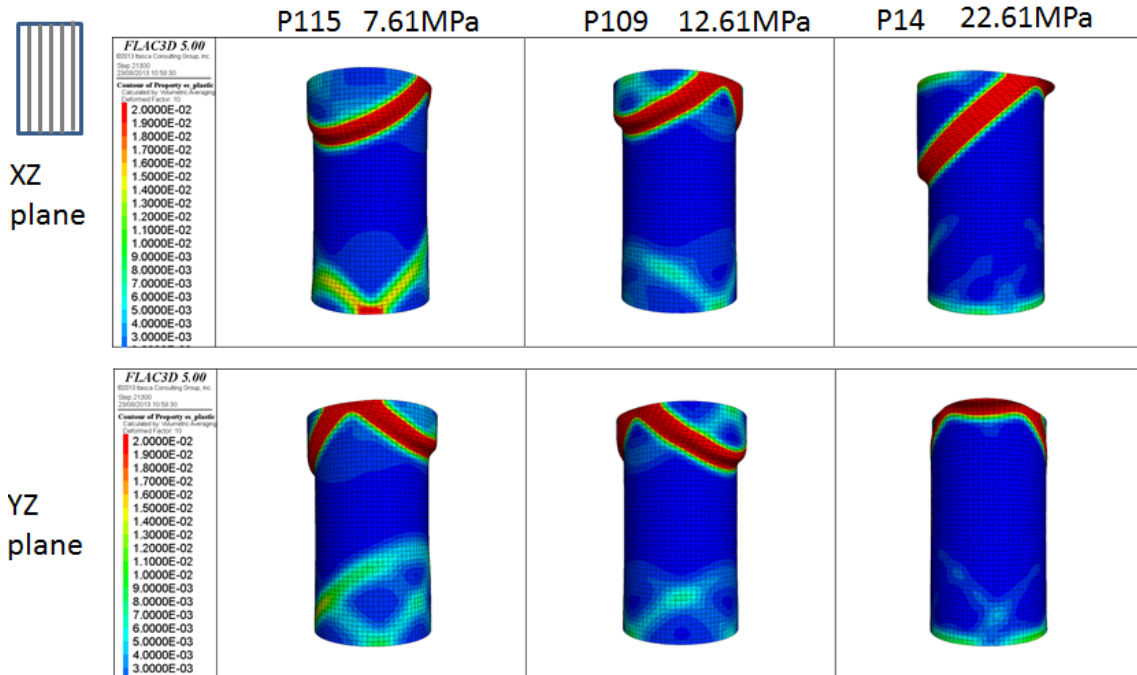


Fig. 4-12: Matrix plastic shear strain at the end of the test for P samples.  
 Magnification factor is 10. Total confining stresses for different tests are indicated with test numbers.

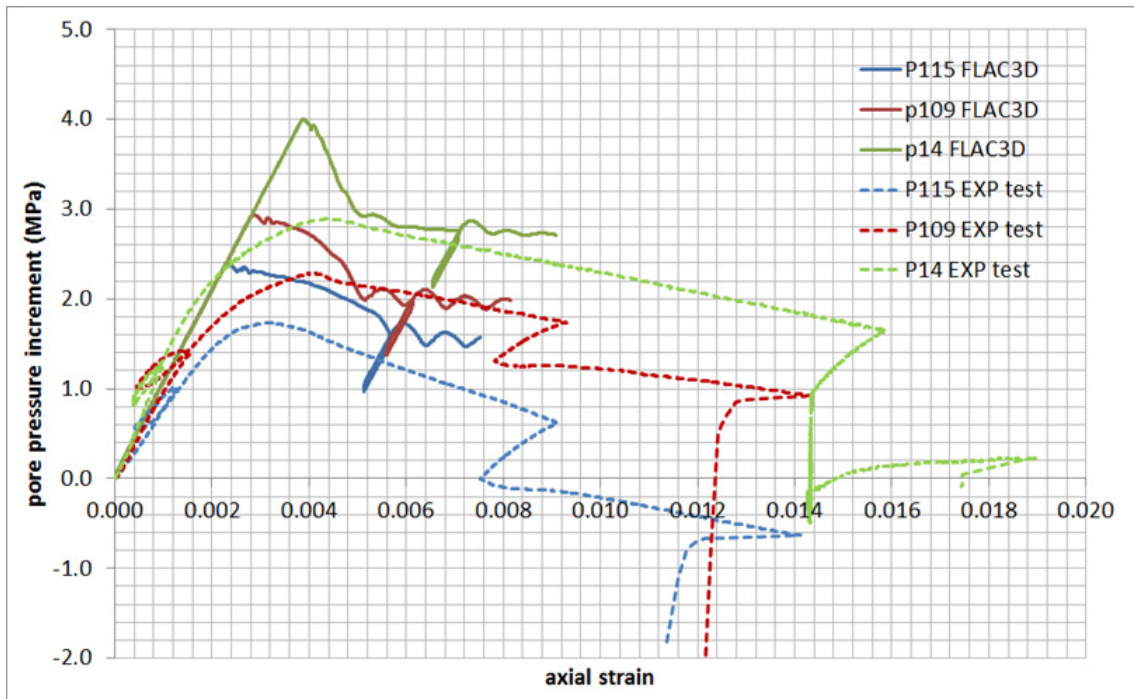


Fig. 4-13: Pore pressure increment comparison between FLAC3D and laboratory experiments (P samples).  
 Increment is relative to end of isotropic loading phase.

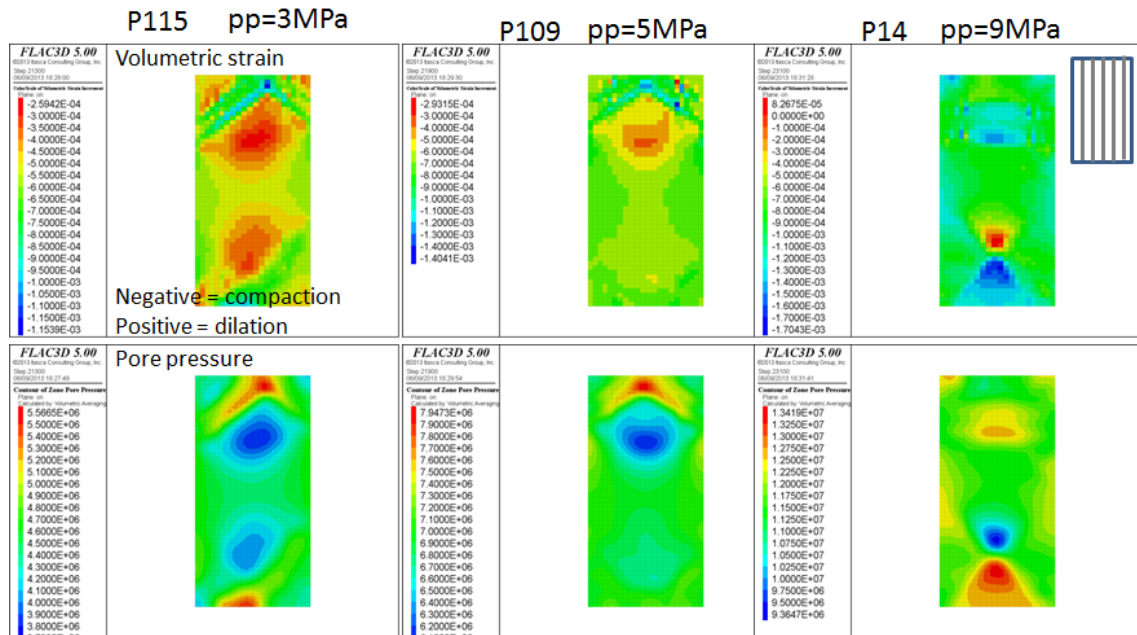


Fig. 4-14: Volumetric strain and pore pressure, P samples (YZ cutting plane).

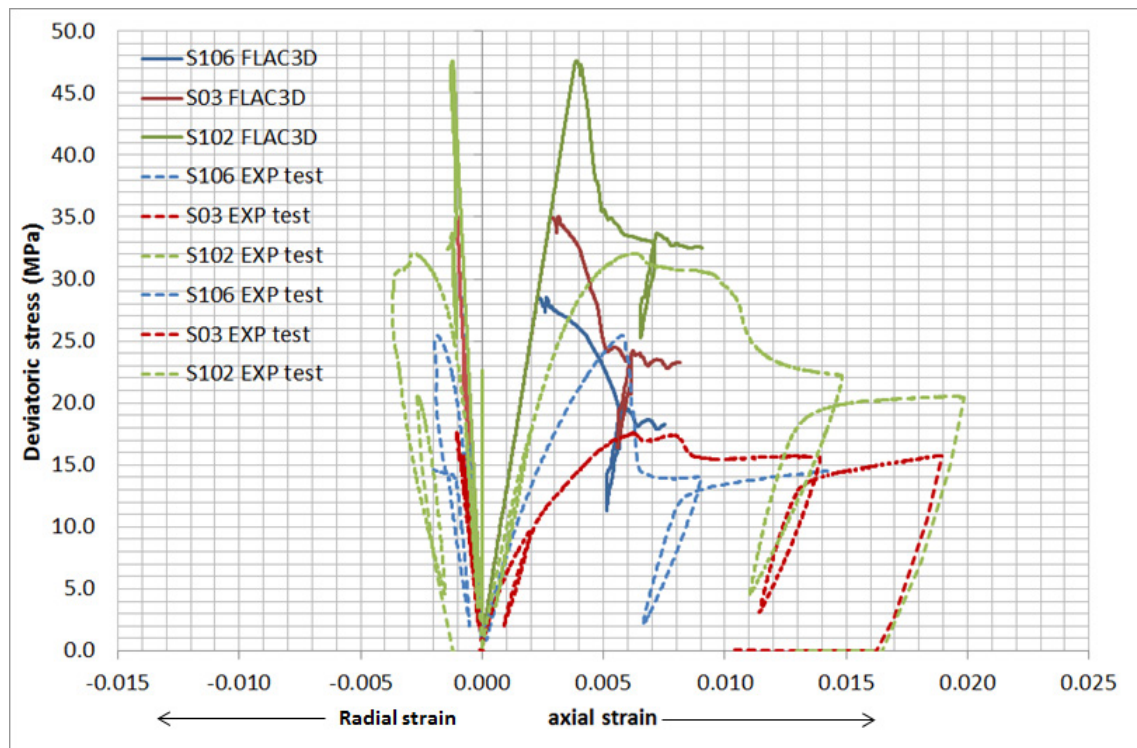


Fig. 4-15: Comparison of stress-strain evolution between FLAC3D and laboratory experiments for S samples.

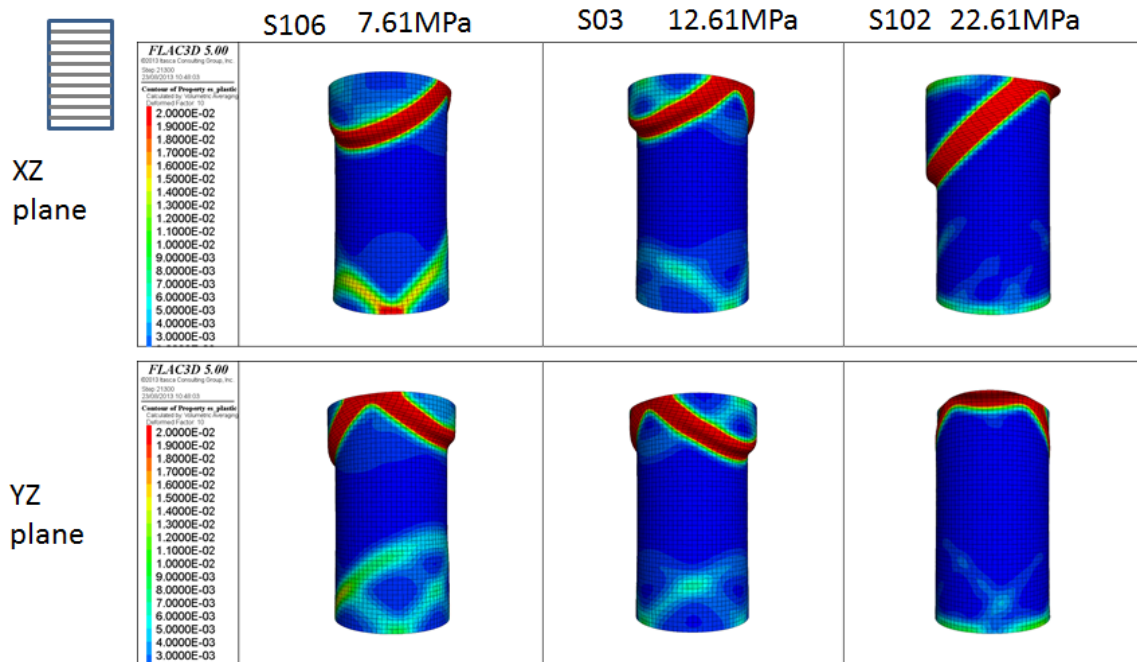


Fig. 4-16: Matrix plastic shear strain at the end of the test for S samples. Magnification factor is 10. Total confining stresses for different tests are indicated with test numbers.

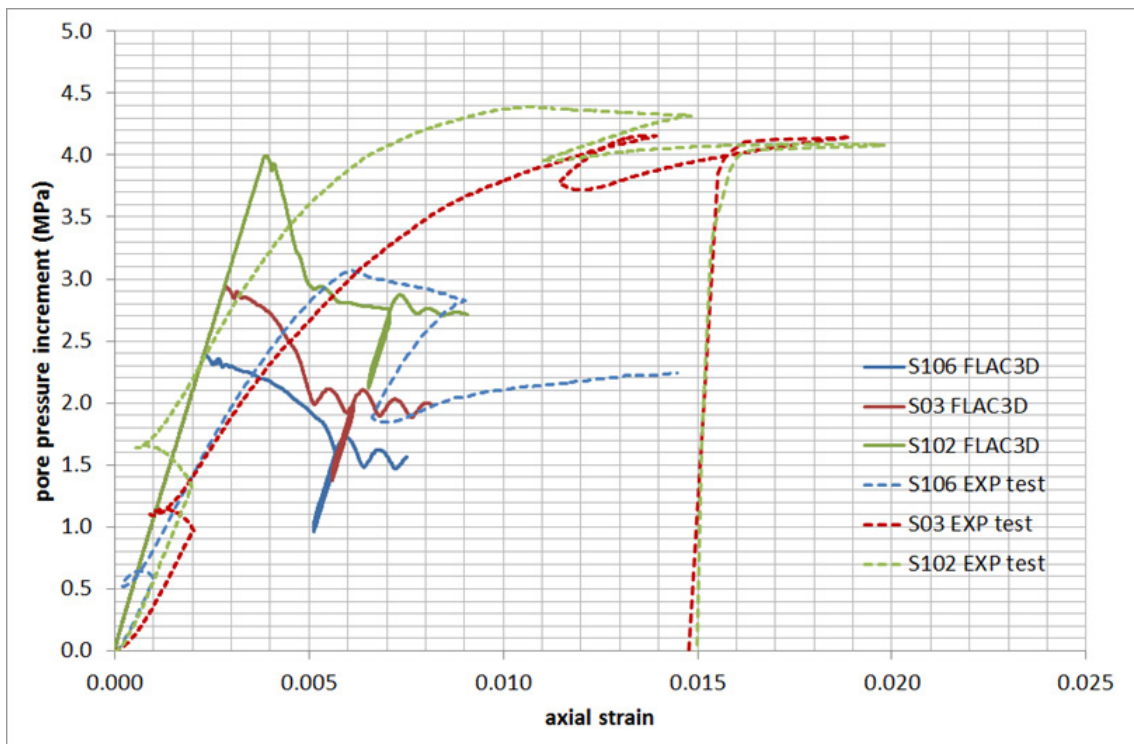


Fig. 4-17: Pore pressure increment comparison between FLAC3D and laboratory experiments (S samples).

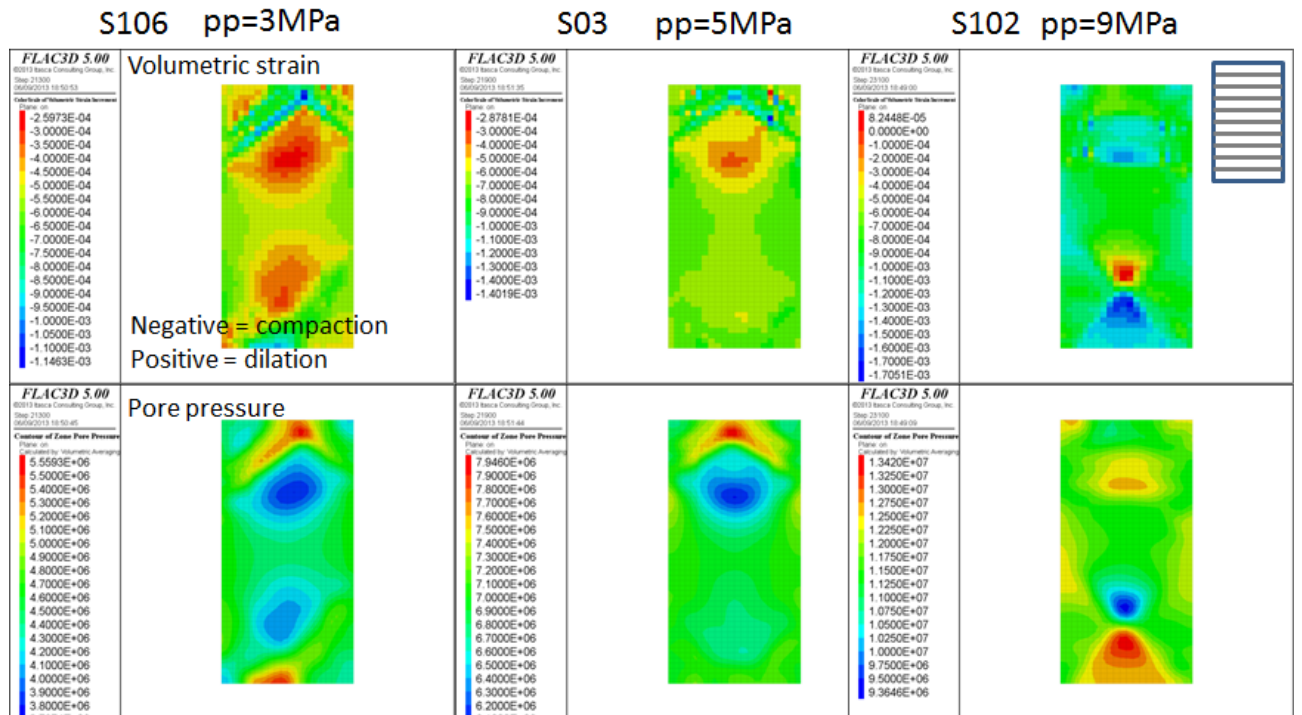


Fig. 4-18: Volumetric strain and pore pressure, S samples (YZ cutting plane).

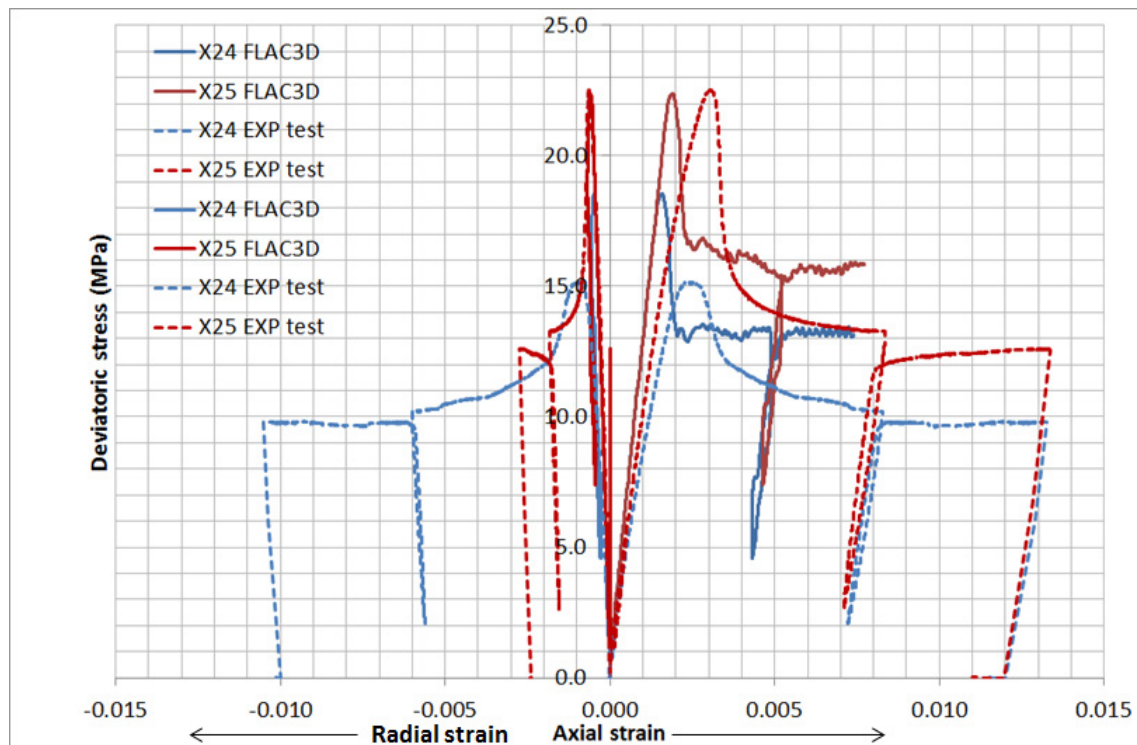


Fig. 4-19: Comparison of stress-strain evolution between FLAC3D and laboratory experiments (X samples).

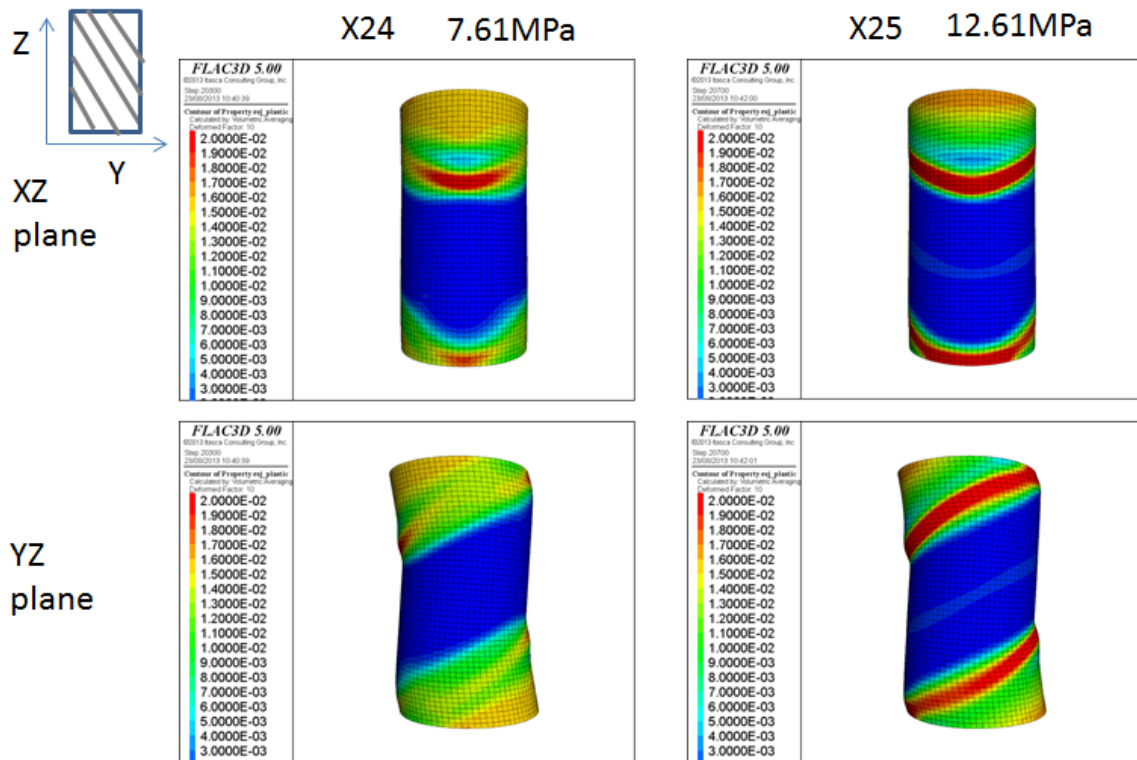


Fig. 4-20: Bedding plastic shear strain at the end of the test, X samples. Magnification factor is 10. Total confining stresses for different tests are indicated with test numbers.

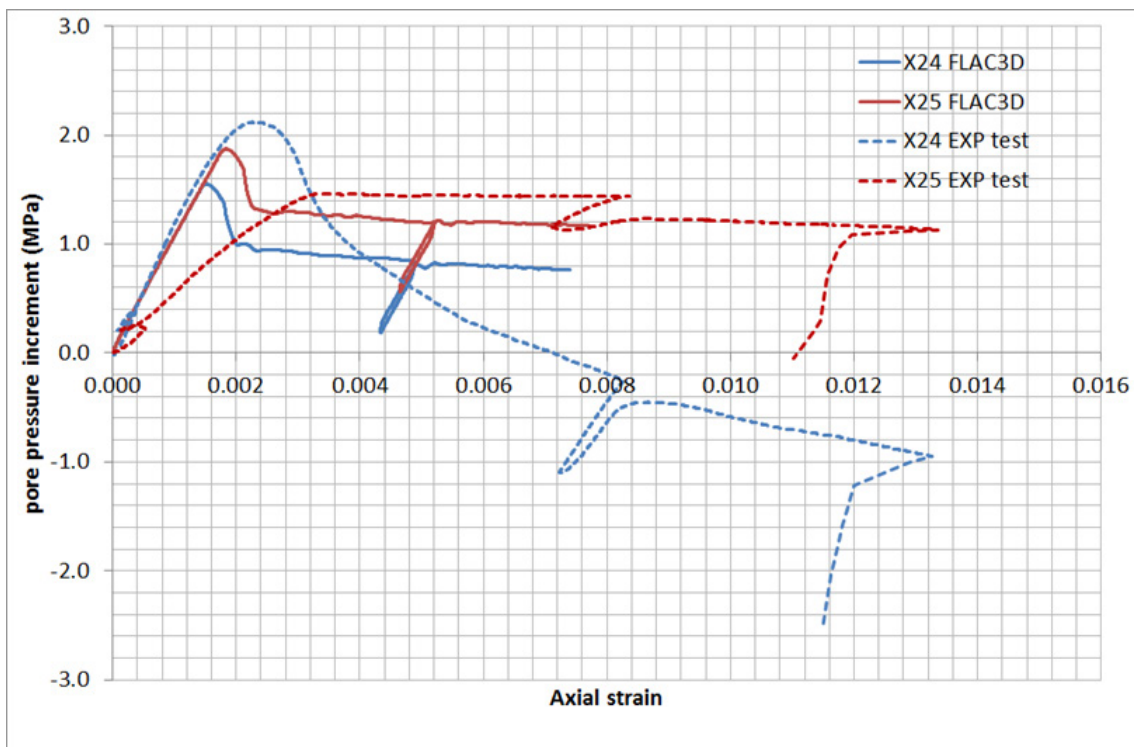


Fig. 4-21: Pore pressure increment comparison between FLAC3D and laboratory experiments (X samples).

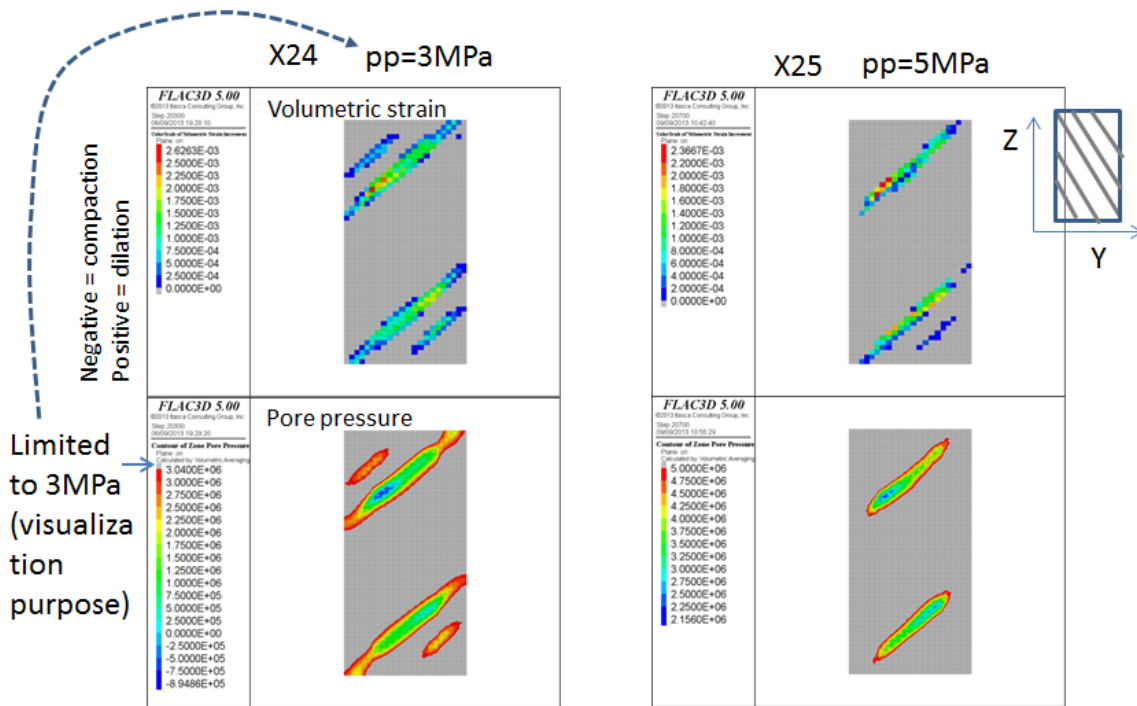


Fig. 4-22: Volumetric strain and pore pressure, X samples (YZ cutting plane).

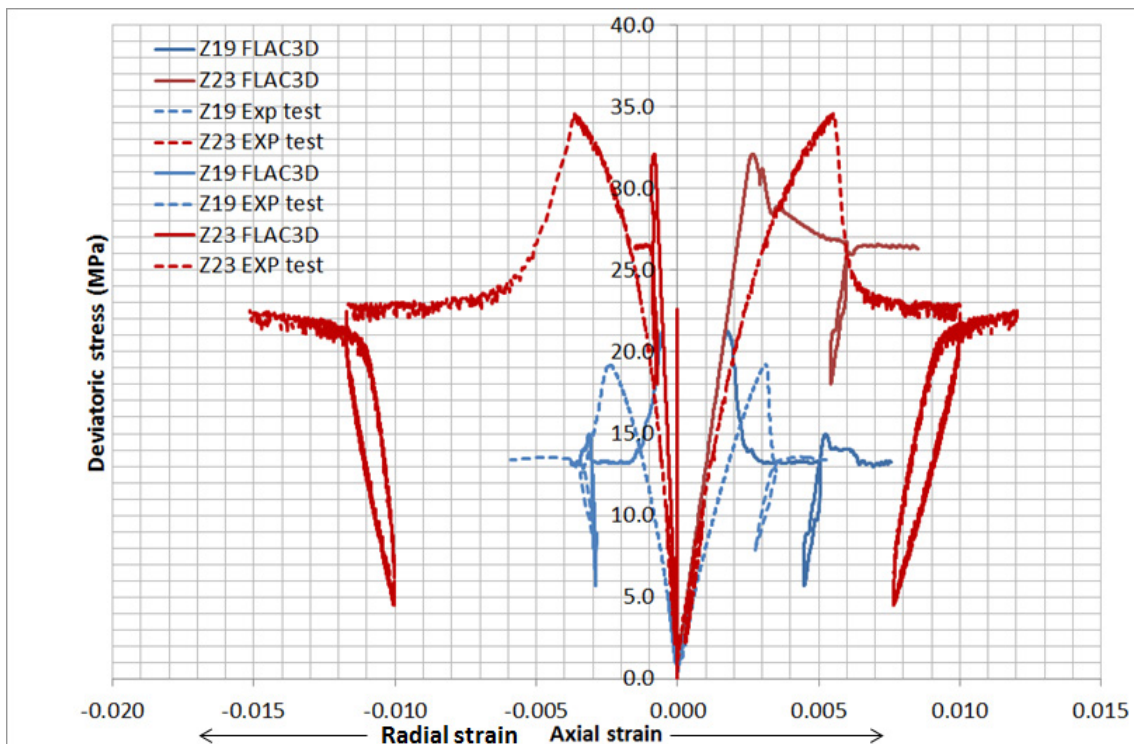


Fig. 4-23: Comparison of stress-strain evolution between FLAC3D and laboratory experiments (Z samples).

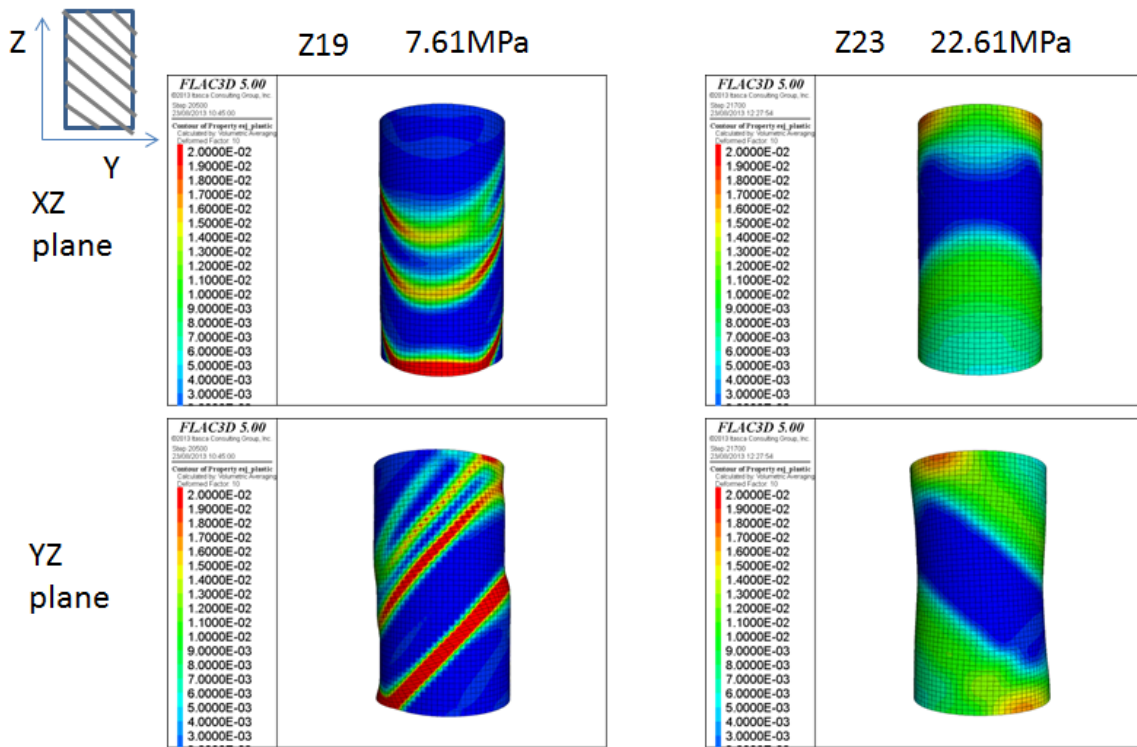


Fig. 4-24: Bedding plastic shear strain at the end of the test, Z samples. Magnification factor is 10. Total confining stresses for different tests are indicated with test numbers.

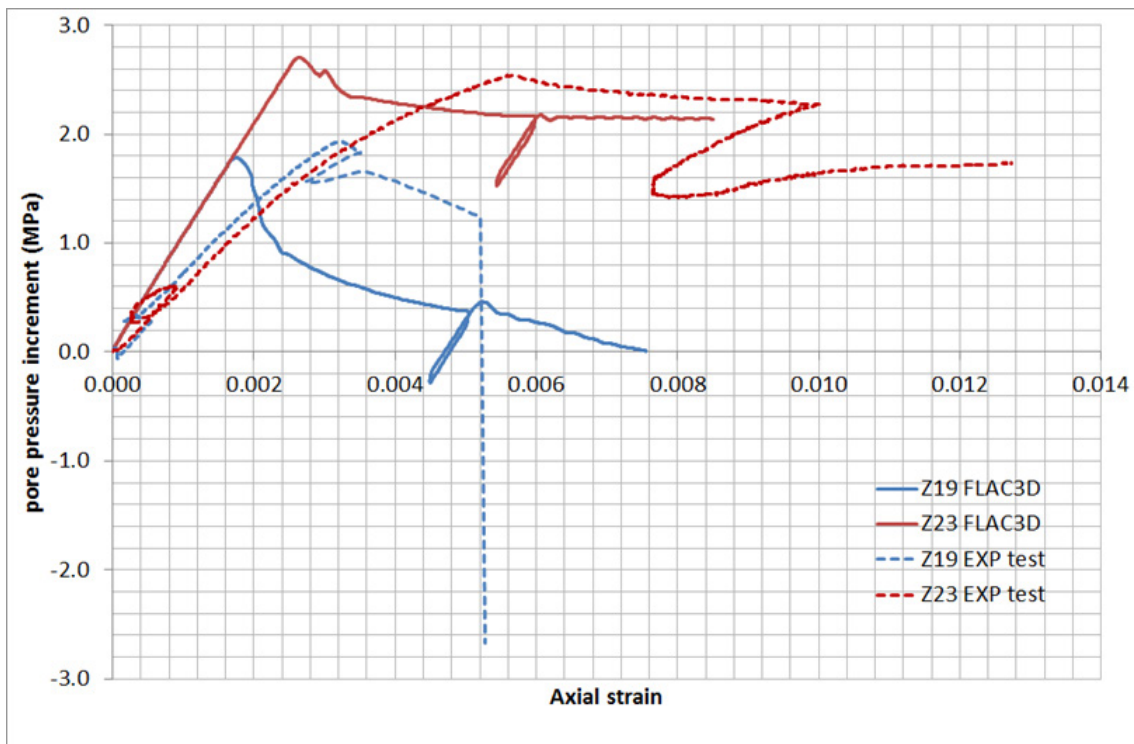


Fig. 4-25: Pore pressure increment comparison between FLAC3D and laboratory experiments (Z samples).

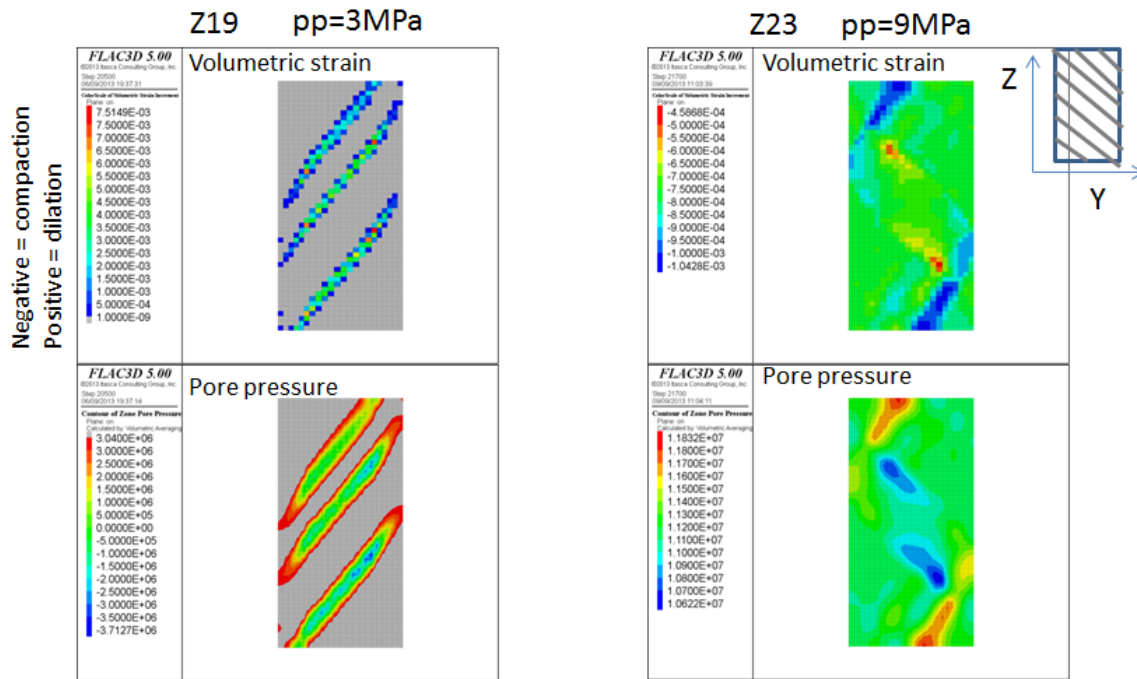


Fig. 4-26: Volumetric strain and pore pressure, Z samples (YZ plane).

#### 4.2 Variation of dilation angle

The results using a nonzero dilation angle are illustrated in Figure 4-27 and Figure 4-28 for P and Z samples, respectively. The dilation angle is set to 3° for all the parametric cases. By definition, the dilation angle affects behavior during plastic deformation only. As expected, the model using a 3° dilation angle yield a higher residual strength, and the difference decreases when the confinement pressure increases. For Z samples, the residual strength is only slightly increased. Since the reference numerical model (no dilation) predicts already a rather high residual strength, as shown in Section 4.1.3, we recommended using a zero dilation angle for further simulations.

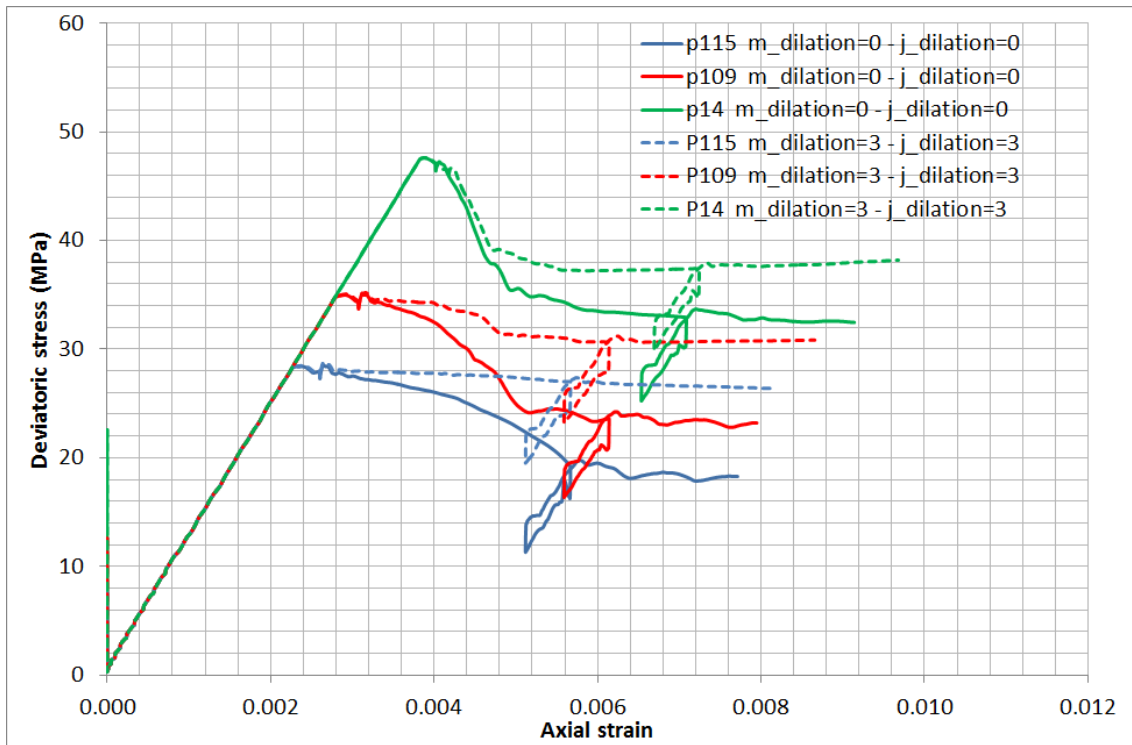


Fig. 4-27: Influence of the dilation angle for P samples.

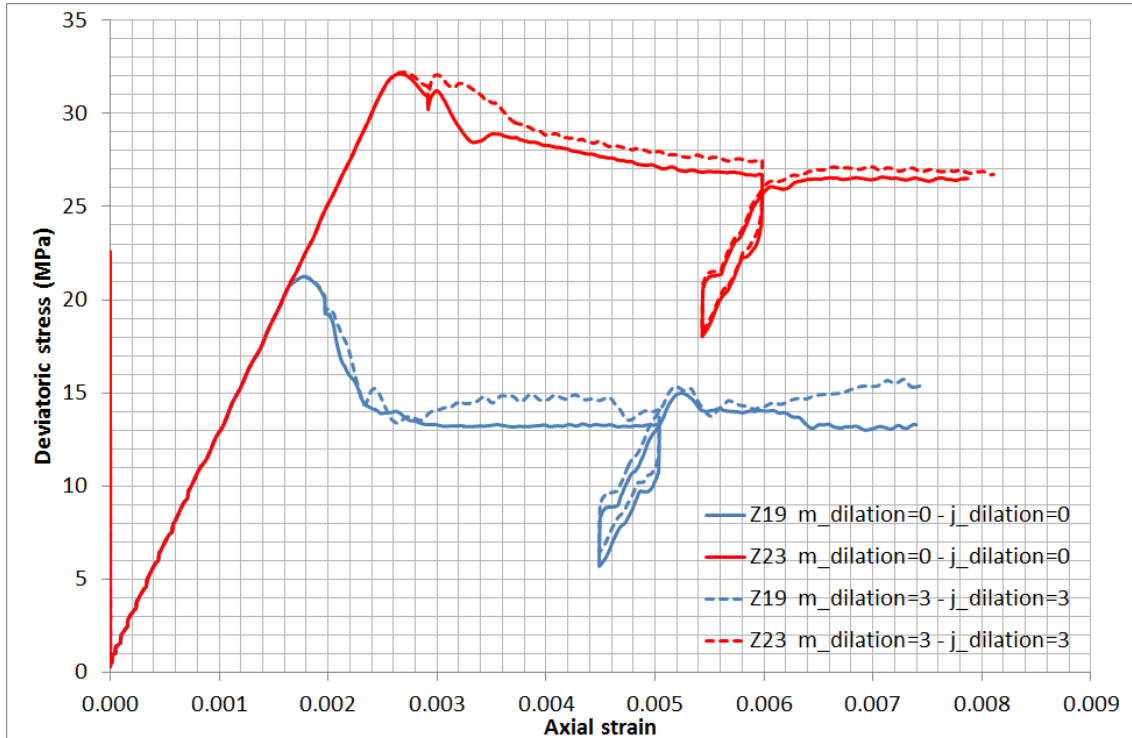


Fig. 4-28: Influence of the dilation angle for Z samples.

### 4.3 Introducing hardening behavior

In order to better reproduce the stress-strain path before peak, a hardening behavior is added to the model. As illustrated in Figure 4-29, when plastic strain occurs, the cohesion is increased from  $C_{initial}$  and will reach  $C_{peak}$  when the plastic strain reaches  $\gamma^{peak}$  (peak plastic shear strain – we will name this "peak strain" in the remainder of the report). Eight parameters are needed:  $C_{ini,m1}$ ,  $C_{ini,m2}$ ,  $C_{ini,j1}$  and  $C_{ini,j2}$  for initial cohesion and  $\gamma_{peak,m1}$ ,  $\gamma_{peak,m2}$ ,  $\gamma_{peak,j1}$  and  $\gamma_{peak,j2}$  for peak strain.

The softening evolution from peak to residual is kept unchanged. The critical strain is now expressed as:

$$\gamma^{residual} = \gamma^{peak} + \gamma^{residual,ref} \quad (\text{Eq 4-2})$$

Where  $\gamma^{residual,ref}$  is the critical strain used in the reference simulations (see Table 4-1).

Table 4-3 details the variations of cohesion obtained after pre-calibration. Only the initial cohesions are new. Other values are unchanged. The variations of cohesion from 0 plastic strain to peak strain is considered non-linear. The complete curve, cohesion vs. plastic shear strain, is shown in Figure 4-30. The hardening behavior has the following features:

- For matrix material: the initial cohesions are close to the residual ones, for both segment 1 and segment 2. Also, the cohesion varies rapidly from its initial value to its peak value over a small plastic shear strain increment (stiffer slope).
- For bedding material: smaller initial cohesions are used. This allows plastic deformation to develop even under small stress loading. The material undergoes rather large plastic shear strains before reaching its peak strength.

The regularization rule used to adjust the critical strain (softening part) is not applied for the hardening part. Physical phenomena are not the same between hardening and softening:

- The material should undergo the same *shear strain* increment before reaching peak strength, thus there is no need to apply strain regularization for the hardening part.
- During post-peak plastic shear strain may increase dramatically, leading to the formation of shear bands. During shear band propagation, the material should undergo the same *shear displacement across the shear band*. Thus, regularization of the critical strain is needed to account for the development of an equal-shear displacement along the shear bands.

The variation of the friction angle from zero plastic strain to peak shear strain is considered linear, since this variation remains small (see Table 4-4).

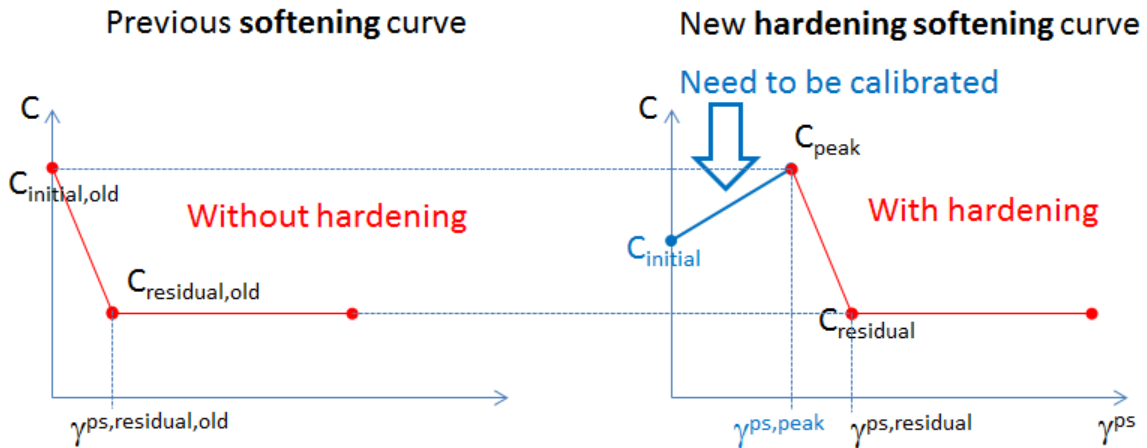


Fig. 4-29: Previous softening curve (left) and new hardening softening curve (right).

Tab. 4-3: Hardening-softening parameters at initial, peak and residual state (cohesion).

	initial		peak		residual	
	cohesion	$\gamma$	cohesion	$\gamma$	cohesion	$\gamma$
MC1	3.5 MPa	0	5.7 MPa	$2.5^{\circ-4}$	3.1 MPa	$202.5^{\circ-4}$
MC2	8.5 MPa	0	14.1 MPa	$3^{\circ-4}$	8.1 MPa	$63^{\circ-4}$
JC1	0.2 MPa	0	4.1 MPa	$12^{\circ-4}$	1.8 MPa	$42^{\circ-4}$
JC2	1.5 MPa	0	7.6 MPa	$18^{\circ-4}$	5.4 MPa	$48^{\circ-4}$

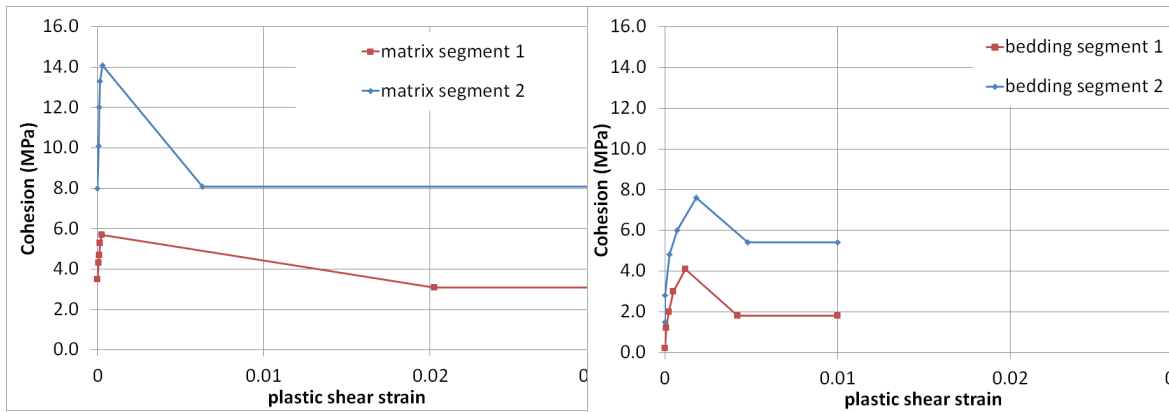


Fig. 4-30: Evolution of cohesion for matrix (left) and for bedding (right).

Tab. 4-4: Hardening-softening parameters at initial, peak and residual state (friction angle).

	initial		peak		residual	
	Friction angle	$\gamma$	Friction angle	$\gamma$	Friction angle	$\gamma$
MF1	32°	0	35°	2.5°-4	29°	202.5°-4
MF2	18°	0	18°	3°-4	19°	63°-4
JF1	24°	0	25°	12°-4	24°	42°-4
JF2	17°	0	17°	18°-4	17°	48°-4

Results accounting for hardening behavior are presented from Figure 4-31 to Figure 4-34 with dashed lines representing the hardening-softening behavior, while solid lines denote the reference cases (softening behavior only).

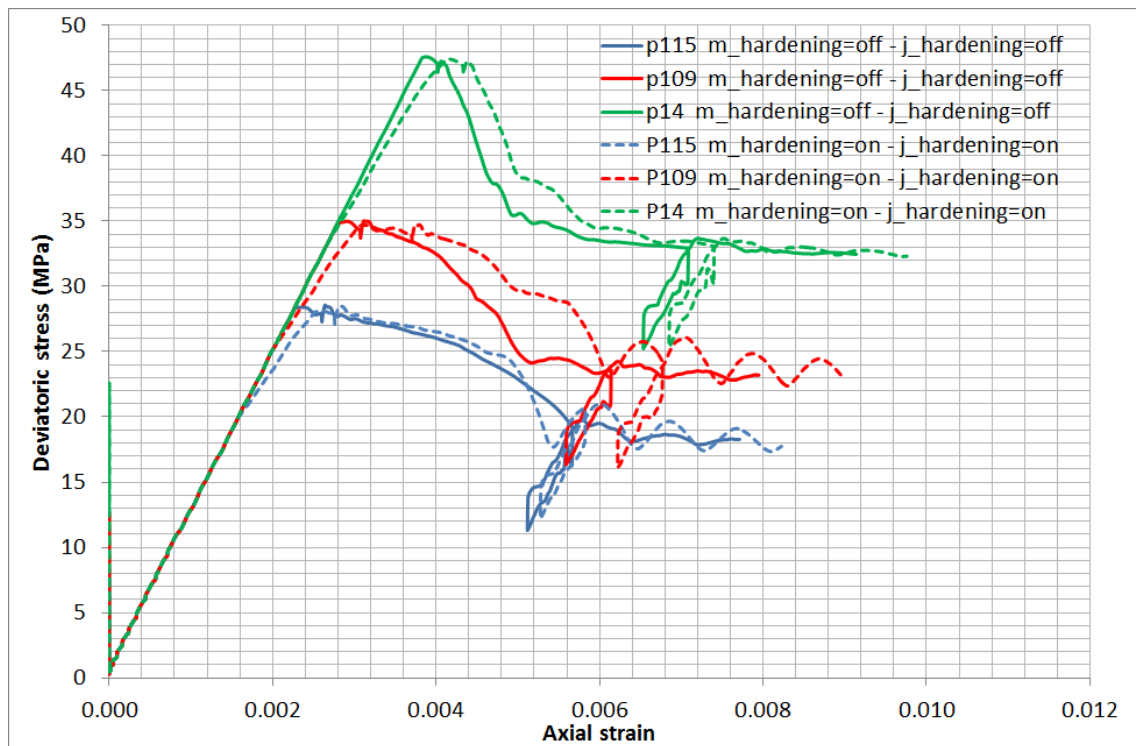


Fig. 4-31: Stress-strain curve accounting for hardening behavior (P samples).

Solid lines indicate the reference cases (only softening), dashed lines indicate results where both hardening (pre-peak) and softening (post-peak) behavior is considered.

For P samples, the stress-strain curves are similar with respect to the reference case since the hardening behavior is simulated by a rather stiff curve (see Figure 4-31). Since  $C_{initial}$  is very close to  $C_{residual}$  (for P samples), the curves tend to bend for loads close to the residual strength. The evolution of the deviatoric stress is not much changed after peak. The pore pressure increment (Figure 4-32) follows the same evolution observed for the stress-strain curve.

The influence of the hardening behavior on triaxial loading is more pronounced for Z samples. The stress-strain curve varies in a way similar to the curve presented in Figure 4-30. Plastic deformation takes place at a rather low stress level (approximately 8 MPa for the Z19 sample and 16 MPa for the Z23 sample). The sample then undergoes noticeable (plastic) strains before reaching peak.

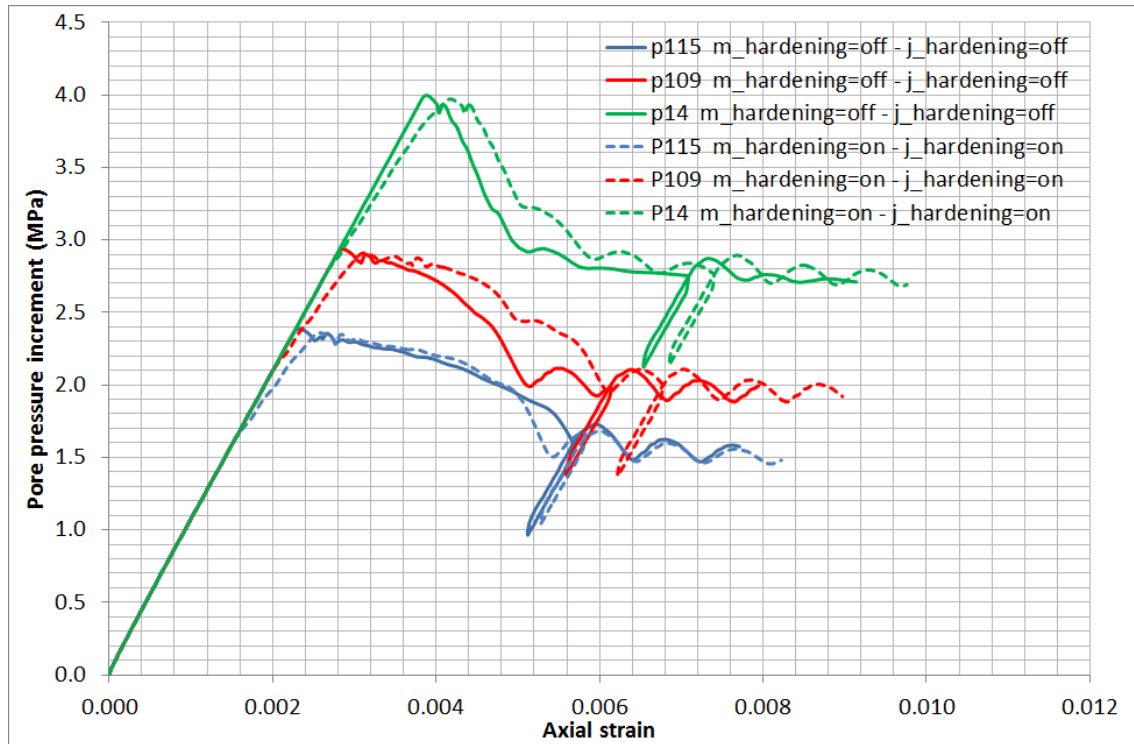


Fig. 4-32: Pore pressure increment accounting for hardening behavior (P samples).

Solid lines indicate the reference cases (only softening), dashed lines indicate results where both hardening (pre-peak) and softening (post-peak) behavior is considered.

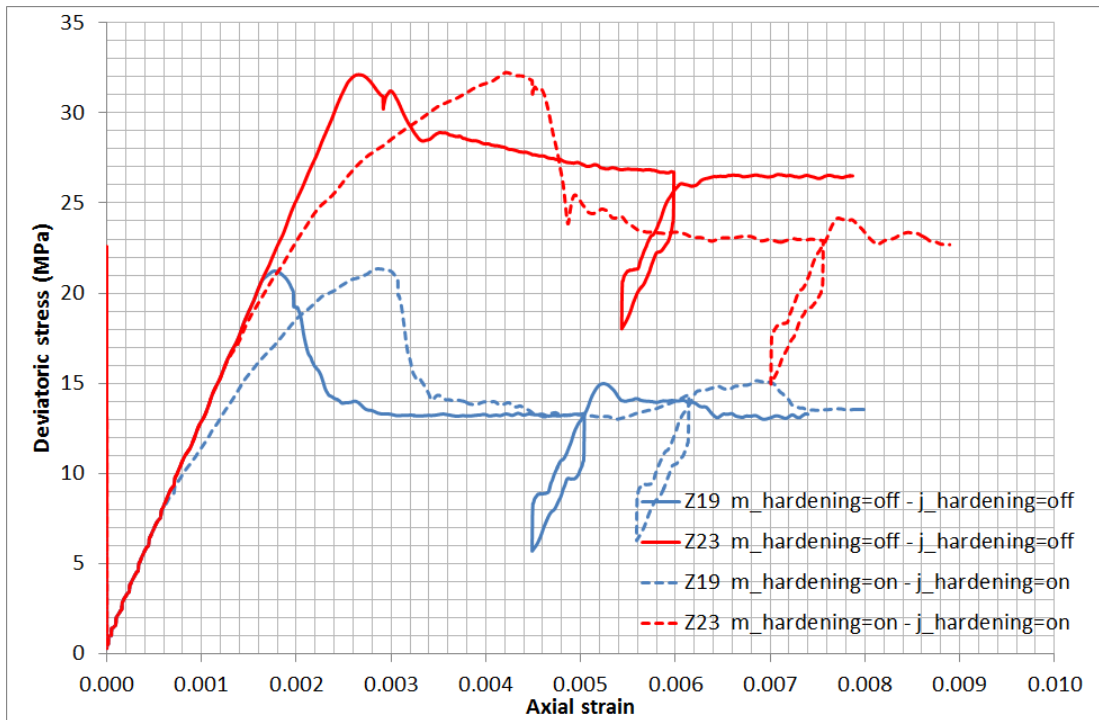


Fig. 4-33: Stress-strain curve accounting for hardening behavior (*Z* samples).

Solid lines indicate the reference cases (only softening), dashed lines indicate results where both hardening (pre-peak) and softening (post-peak) behavior is considered.

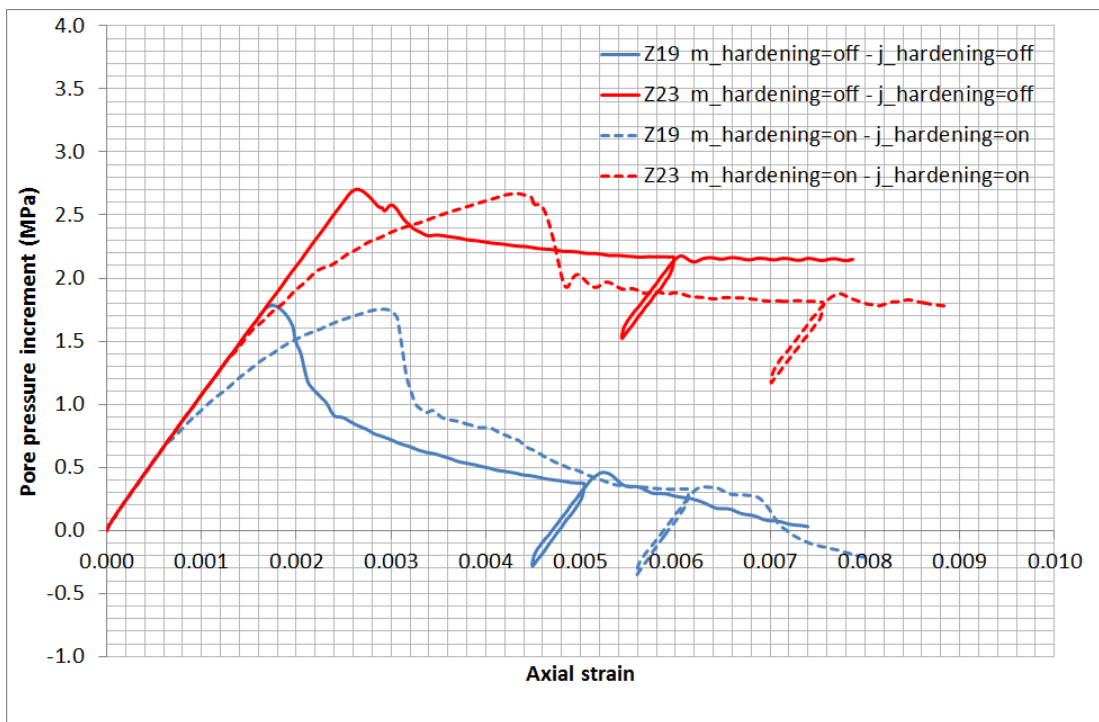


Fig. 4-34: Pore pressure increment account for hardening behavior (*Z* samples).

Solid lines indicate the reference cases (only softening), dashed lines indicate results where both hardening (pre-peak) and softening (post-peak) behavior is considered.

#### 4.4 Variation in pore pressure coupling parameters

Two parameters describing the coupling between mechanical response and fluid pressure variations are studied. They are the Biot coefficient  $\alpha$  and the Skempton coefficient  $B_{sk}$ .

The Biot coefficient  $\alpha$  is defined as the ratio of the fluid volume gained (or lost) in a material element to the volume change of that element when the pore pressure is changed. It can be determined in the same drained test as that used to determine the drained bulk modulus ( $K_d$ ) of the material. Its range of variation is between  $\frac{3n}{2+n}$  and 1, where  $n$  is the porosity. In the particular case of an incompressible solid constituent,  $\alpha = 1$ . This is the default value adopted by *FLAC3D* [1]. The Biot coefficient is set at 0.8 for all the simulations presented previously, including the reference case.

The general formulation of  $B_{sk}$  can be expressed as:

$$B_{sk} = \frac{\alpha M}{K_d + \alpha^2 M} \quad (\text{Eq 4-3})$$

Where  $\alpha$  is the Biot coefficient,  $M$  is the Biot modulus and  $K_d$  is the drained bulk modulus.

Clearly, a change in  $\alpha$  may induce a change in  $B_{sk}$ . In order to test independently the influence of  $\alpha$  and  $B_{sk}$ , the following approach is used.

- Influence of the Biot coefficient: change  $\alpha$  and adjust  $M$  in order to keep  $B_{sk}$  constant. The parameter set is reported in Table 4-5. The case using  $\alpha = 0.8$  is the reference case. The bulk modulus  $K_d$  and  $K_u$  are calculated using the following equation:

$$K = \frac{E}{3(1-2\nu)} \quad (\text{Eq 4-4})$$

The drained Young's modulus is set at 12 GPa, respectively 15 GPa for undrained Young's modulus, and Poisson's ratio is 0.27. Note that these stiffness values are much more representative for a data set parallel to bedding (P-samples) as indicated in Table 2-2. The direct consequence in combination with Equations 4-3 and 4-4 is that the calculated  $B_{sk}$  values are very low. Variation of higher  $B_{sk}$  values (and lower stiffness) is explored further below (Section 4.4.3).

Tab. 4-5: Parameters set for cases using different Biot coefficient.

$\alpha$	$M$	$B_{sk}$	$K_d$	$K_u$
0.8	3.4 GPa	0.25	8.7 GPa	10.9 GPa
0.9	3.16 GPa	0.25	8.7 GPa	10.9 GPa
1.0	2.98 GPa	0.25	8.7 GPa	10.9 GPa

- Influence of  $B_{sk}$ : change  $B_{sk}$  and adjust  $M$  in order to keep  $\alpha$  constant. For the case where  $\alpha$  is kept constant,  $K_u$  is slightly modified by:

$$K_u = \alpha^2 M + K_d \quad (\text{Eq 4-5})$$

Tab. 4-6: Parameters set for cases using different  $B_{sk}$ .

$\alpha$	$M$	$B_{sk}$	$K_d$	$K_u$
0.8	3.4 GPa	0.25	8.7 GPa	10.9 GPa
0.8	3.16 GPa	0.236	8.7 GPa	10.7 GPa
0.8	2.98 GPa	0.225	8.7 GPa	10.6 GPa

Note that, the Skempton coefficient  $B_{sk}$  is not input directly in FLAC3D but that it can be obtained by choosing an appropriate value for the fluid bulk modulus or for the Biot modulus (here, the Biot modulus is specified).

#### 4.4.1 Biot coefficient

For each numerical sample, three different Biot coefficients are studied (0.8, 0.9 and 1.0). The results of P sample triaxial tests using different Biot coefficients are presented from Figure 4-35 to Figure 4-37. The effect of the changed coefficient is minimal. In order to verify the "apparent"  $B_{sk}$  in the numerical model, it can be computed using the following relation:

$$B_{sk} = \frac{\Delta p}{-\frac{\sigma_1 - \sigma_3}{3}} \quad (\text{Eq 4-6})$$

where  $\Delta p$  is the excess pore pressure. Thus,  $B_{sk}$  can be derived from the results represented in Figure 4-35 and Figure 4-36. The computed  $B_{sk}$  is shown in Figure 4-37. It matches well the values reported in Table 4-5, i.e.,  $B_{sk} = 0.25$ .

Similar behaviors are observed for Z samples. Small variations in behavior are observed, only during the residual phase. The Skempton  $B_{sk}$  is also checked for Z samples. The computed

$B_{sk}$  values stay very close to the "input values". However, it appears that  $B_{sk}$  drops from the target value to a lower value after peak strength for Z19 samples. This is an effect of shear band formation, which induces a pore pressure drop. However, the verification of  $B_{sk}$  is significant only during the initial elastic loading phase, where the pore pressure is expected to increase rather uniformly over the whole sample.

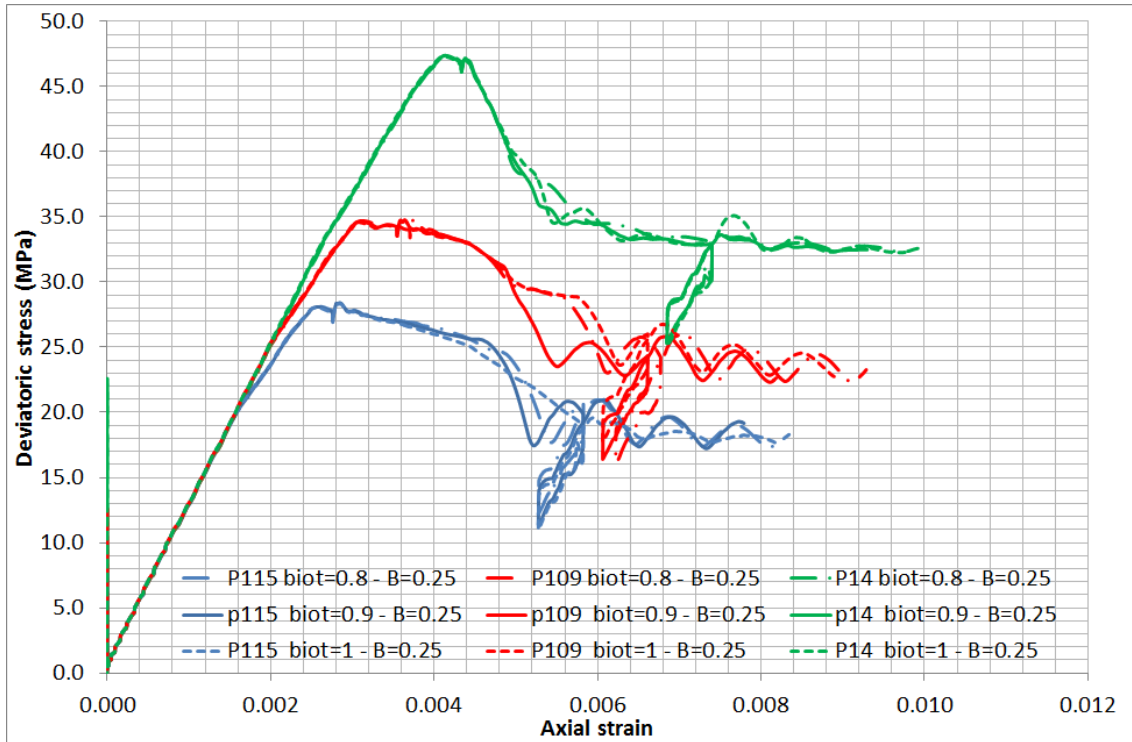


Fig. 4-35: Resulting stress-strain curves from variation of Biot coefficient  $\alpha$  (P samples).

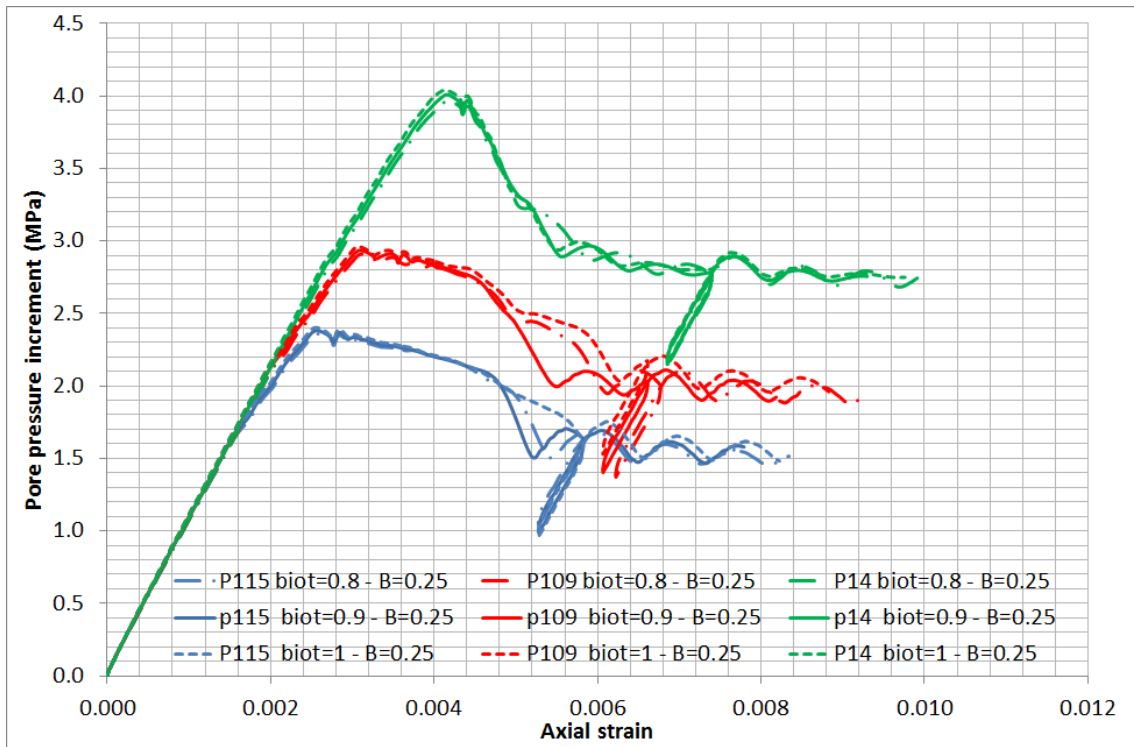


Fig. 4-36: Resulting pore pressure increments from variation of Biot coefficient  $\alpha$  (P samples).

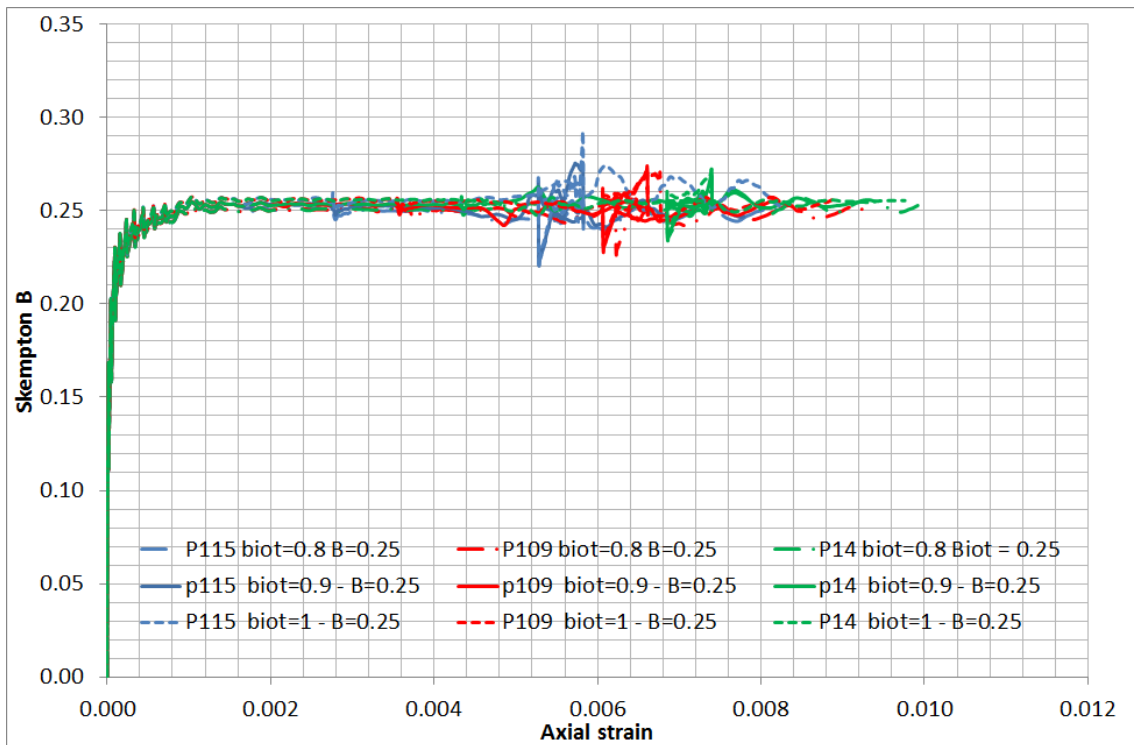


Fig. 4-37: Verification of  $B_{sk}$  for cases using different Biot coefficients (P samples).

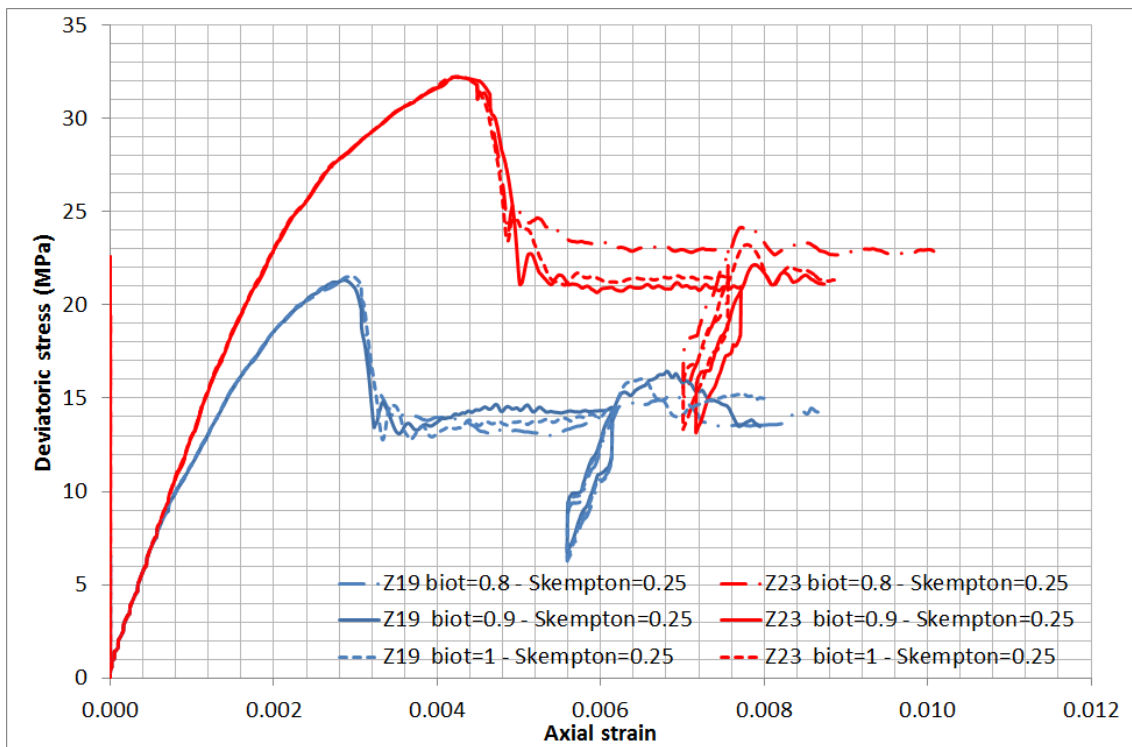


Fig. 4-38: Stress-strain curve using different Biot coefficients (Z sample).

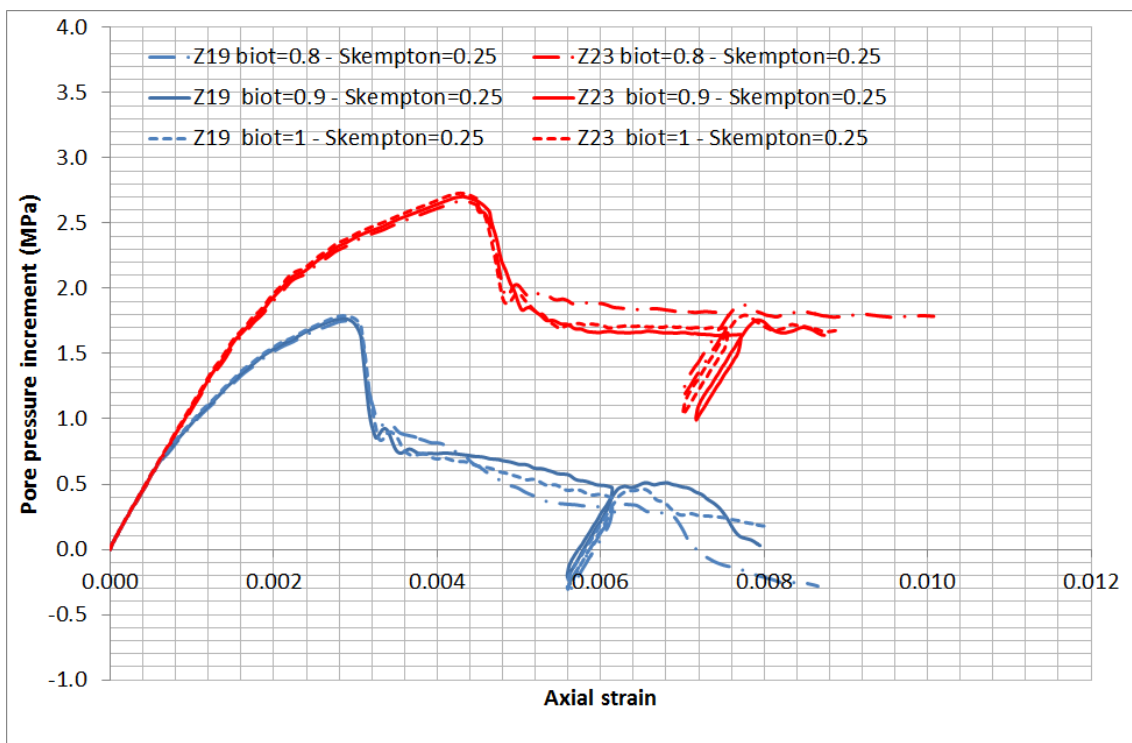


Fig. 4-39: Pore pressure increments from variation of Biot coefficient  $\alpha$  (Z samples).

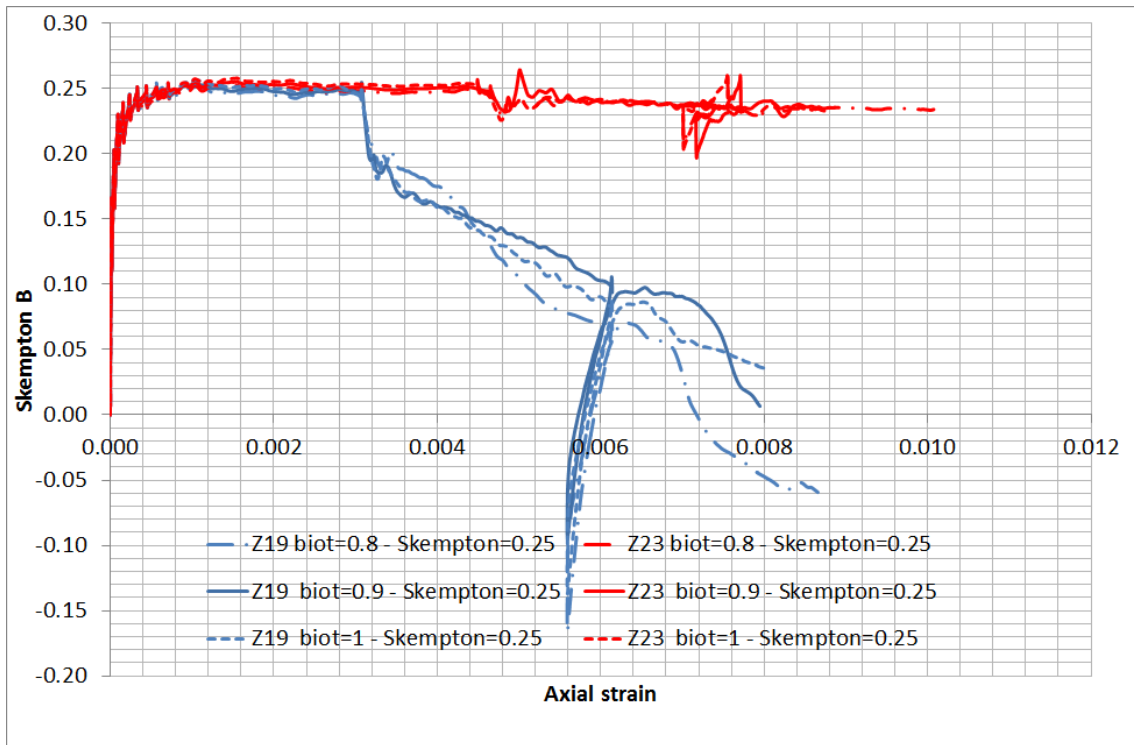


Fig. 4-40: Verification of  $B_{sk}$  for cases using different Biot coefficients (Z samples).

#### 4.4.2 Skempton B – lower value (0.225 to 0.25)

The results of numerical simulation using different  $B_{sk}$  are presented from Figure 4-41 to Figure 4-43 for P samples, and from Figure 4-44 to Figure 4-46 for Z samples. One should keep in mind that  $B_{sk}$  is not input explicitly in the numerical model. Instead, an appropriate Biot modulus is given to reach the target  $B_{sk}$  (see Table 4-6).

The variation of  $B_{sk}$  at low values and over a very narrow range has little effect on the evolution of the deviatoric stress. The peak stress and the residual stress are almost unchanged. However, the change in  $B_{sk}$  induces noticeable changes in pore pressure increment. A model using a higher  $B_{sk}$  predicts higher pore pressure increments. This is to be expected, considering Equation 4-6. Figure 4-43 checks the value of  $B_{sk}$  and shows that the model behaves in the desired way. Similar behavior is observed for Z samples. Clearly,  $B_{sk}$  shows noticeable influence on the pore pressure increment. For a constant Biot coefficient ( $\alpha$ ), a higher  $B_{sk}$  means a higher Biot Modulus. This results in a higher fluid bulk modulus. Thus, the model predicts higher pore pressure increment.

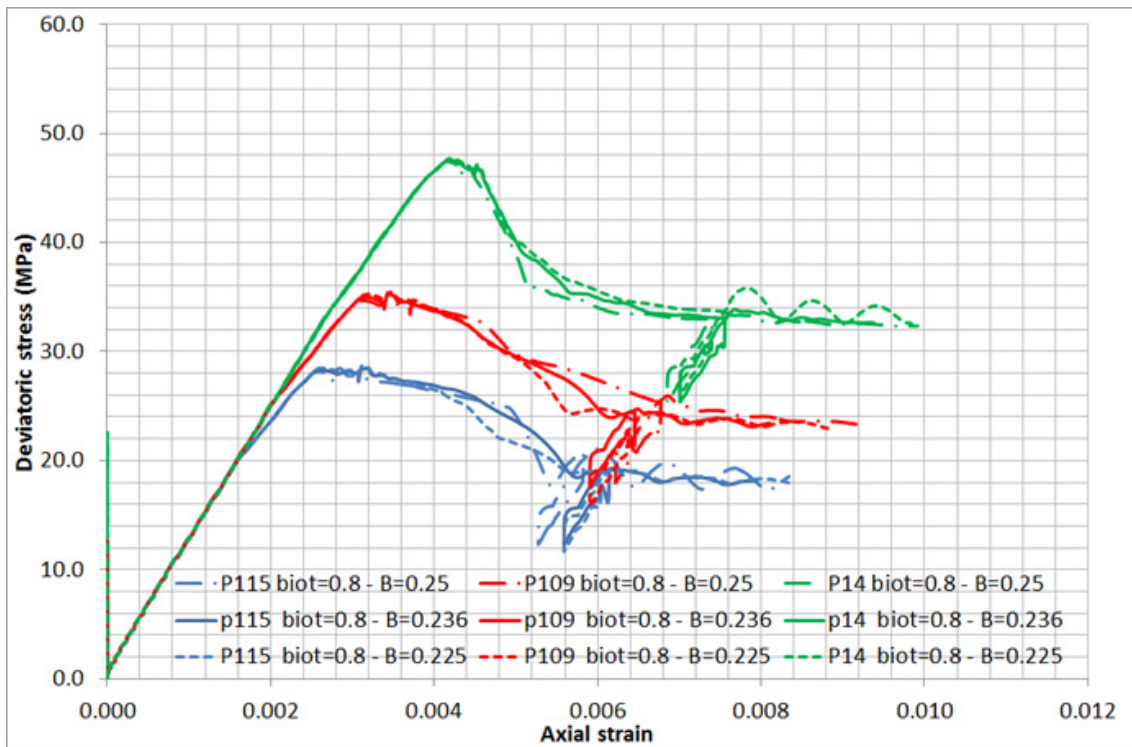


Fig. 4-41: Stress-strain curve for different  $B_{sk}$  (P samples).

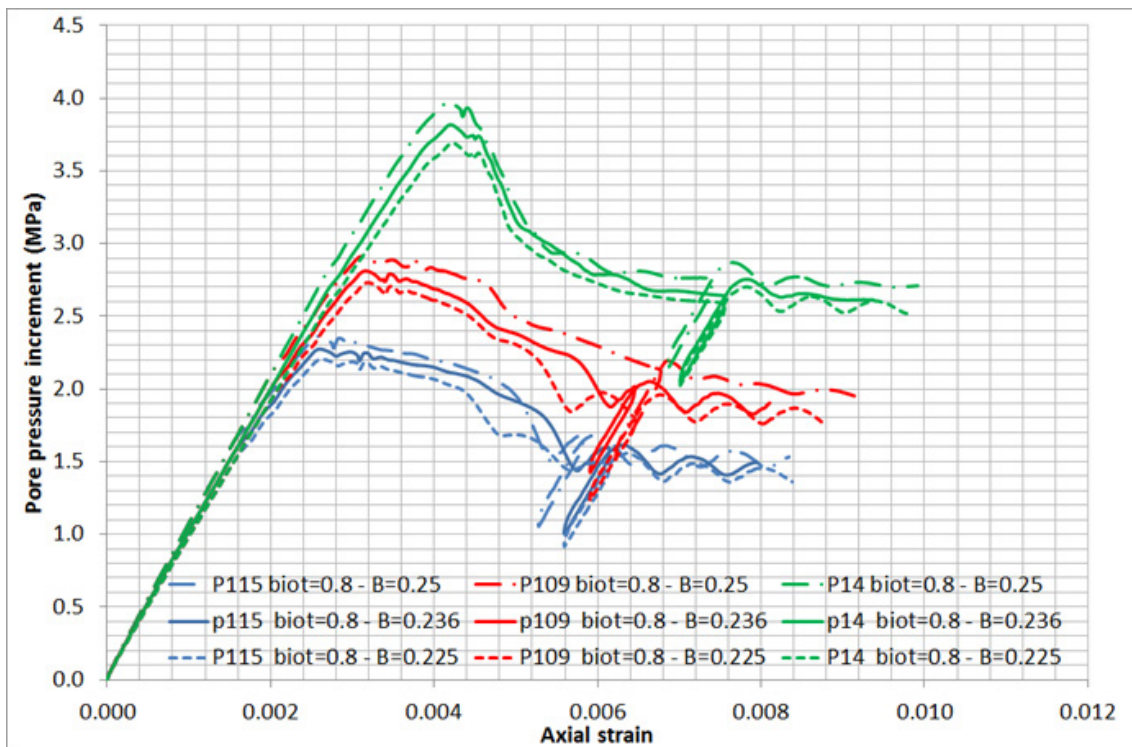


Fig. 4-42: Pore pressure increment for different  $B_{sk}$  (P samples).

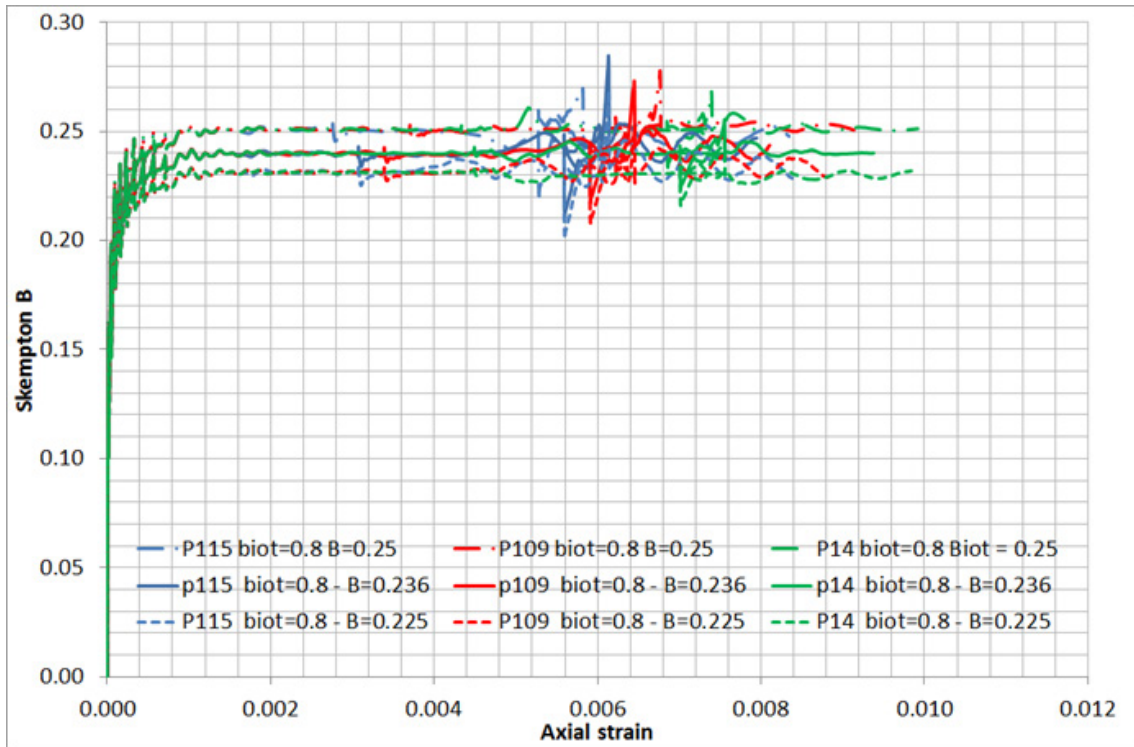


Fig. 4-43: Verification of  $B_{sk}$  for cases using different  $B_{sk}$  (P samples).

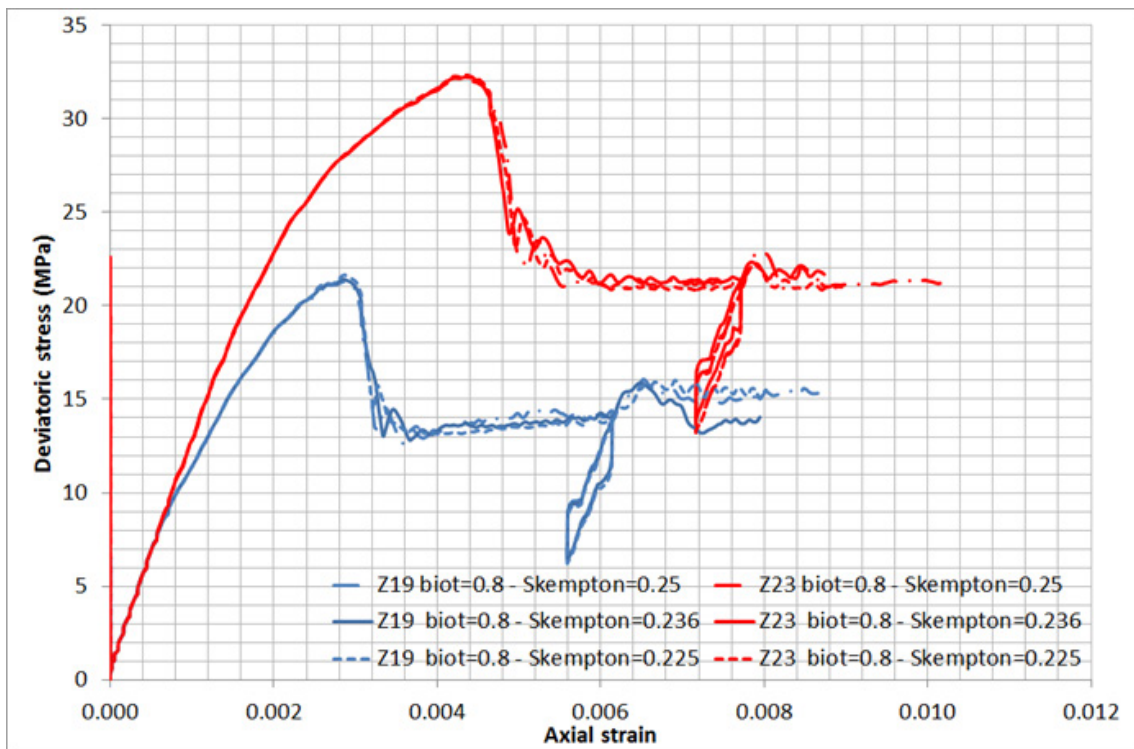


Fig. 4-44: Stress-strain curve for different  $B_{sk}$  (Z samples).

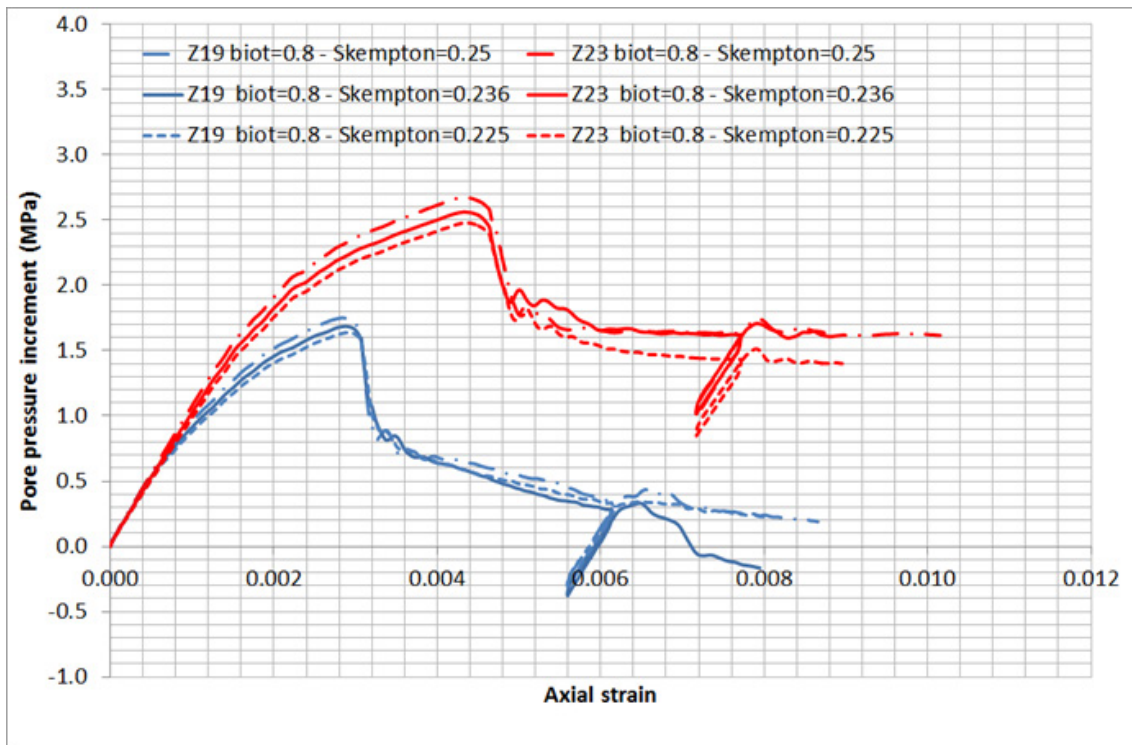


Fig. 4-45: Pore pressure increment for different  $B_{sk}$  (Z samples).

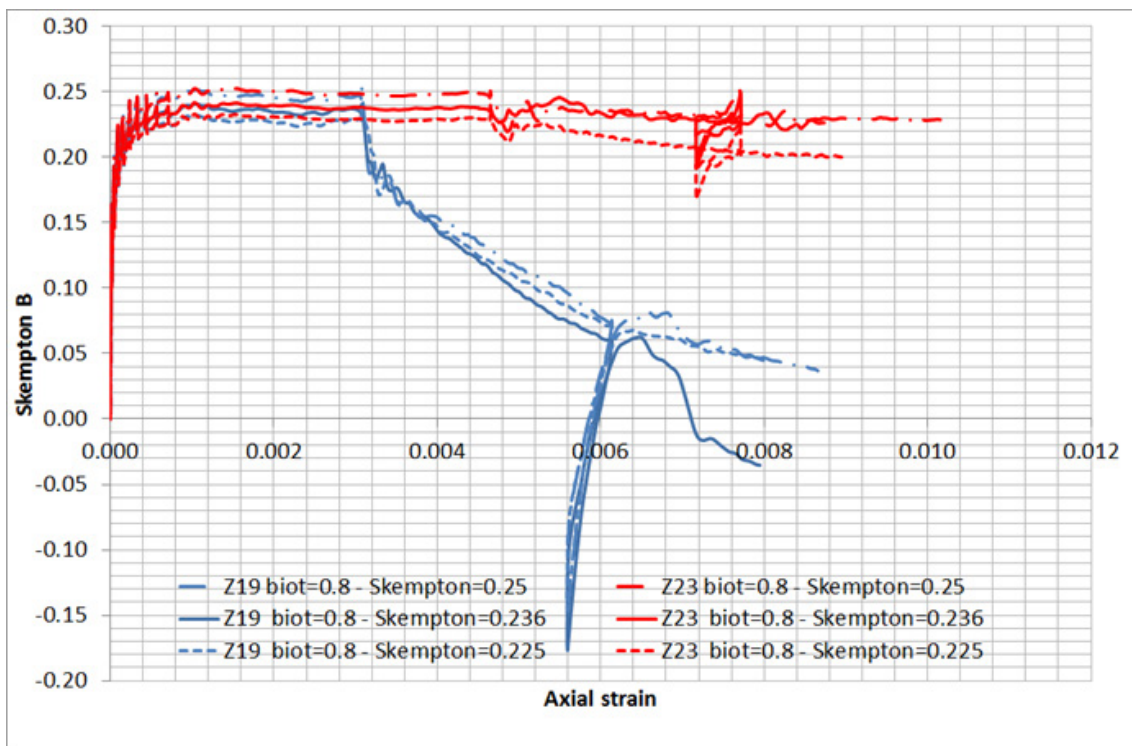


Fig. 4-46: Verification of  $B_{sk}$  for cases using different  $B_{sk}$  (Z samples).

#### 4.4.3 Skempton B - higher value (0.7 to 0.9)

The previous results have shown that variation of  $B_{sk}$  has a noticeable influence on the pore pressure increment. Special attention is paid in this section on the influence of  $B_{sk}$  using much higher values. As reported in Table 4-7,  $B_{sk}$  is varied from 0.7 to 0.9 while the Biot coefficient is kept constant ( $\alpha = 0.8$ ). An appropriate Biot modulus is calculated as well. The simulations using higher  $B_{sk}$  are carried out for P samples, S samples and X samples. Simulations for Z samples are not included.

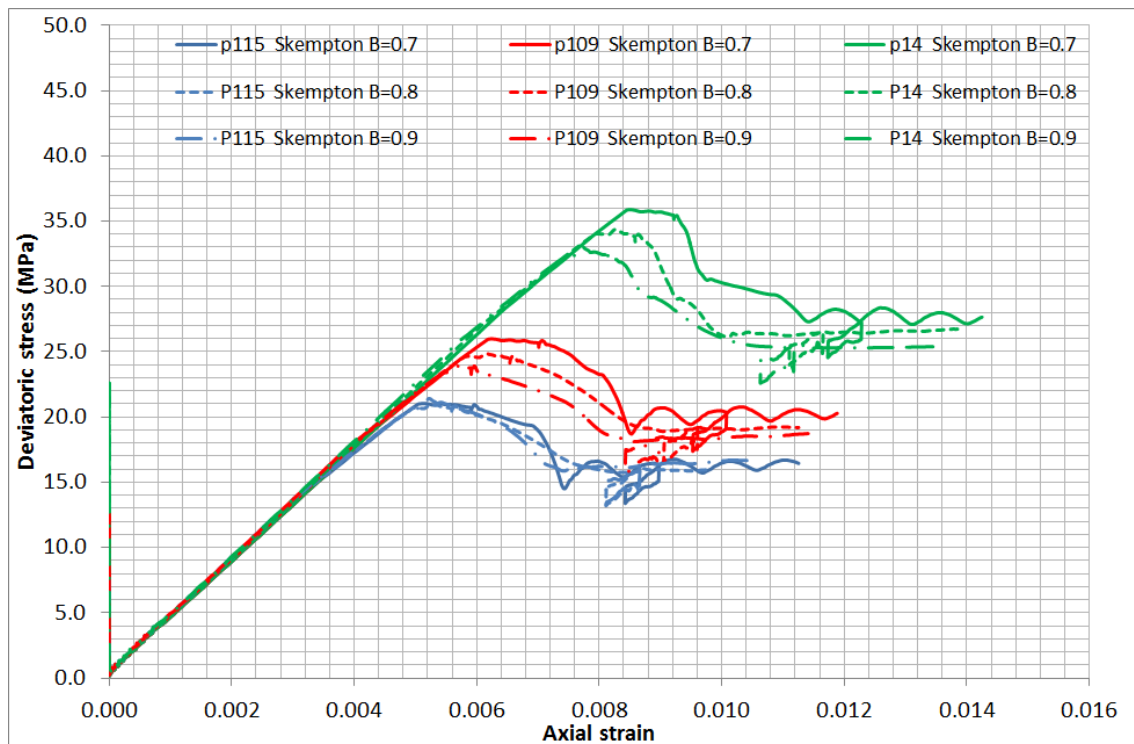
A lower Young's modulus is used here for the simulations using higher  $B_{sk}$  values:  $E = 4$  GPa (drained), instead of 12 GPa for previous simulations. This lower bulk modulus implies a smaller initial slope for the stress-strain curve. The reason for this change is to better calibrate the model behavior for S samples rather than for P samples (cf. Table 2-2).

Results in terms of the strain-stress curve, pore pressure increment, as well as the  $B_{sk}$  verification are represented from Figure 4-47 to Figure 4-55. Overall, the model behavior is qualitatively similar to the one presented in Section 4.4.2 where smaller  $B_{sk}$  are used. The following remarks are observed from the additional simulations:

- A higher peak strength is observed for models using a smaller  $B_{sk}$ , although the strengths remain of the same order when varying  $B_{sk}$  between 0.7 and 0.9. Note that the peak strength is seriously degraded compared to the cases using much smaller  $B_{sk}$  (see Section 4.4.2).
- As a consequence of using higher  $B_{sk}$ , the increase in pore pressure is more pronounced. The maximum pore pressure increment reaches 9.7 MPa for the case P14-  $B_{sk} = 0.9$  and 4.8 MPa for the case X25-  $B_{sk} = 0.9$ .
- As expected, the initial slope of the stress-strain decreases compared to previous results using greater Young's modulus (compare Figure 4-31 and Figure 4-47). Also, the peak strength and the residual strength are reduced if higher  $B_{sk}$  is used.
- P samples and S samples show similar behavior.
- A stiffer slope of the pore pressure increment is observed for cases using higher  $B_{sk}$ . The model using higher  $B_{sk}$  induces a higher Biot modulus. Thus, the change in pore pressure is higher.
- The computed  $B_{sk}$  (obtained from the post treatment after simulation) stays very close to the "input" one.

Tab. 4-7: Parameter set for  $B_{sk}$  tests.

$\alpha$	$M$	$B_{sk}$	$K_d$	$K_u$
0.8	5.77 GPa	0.7	2.9 GPa	6.59 GPa
0.8	8.06 GPa	0.8	2.9 GPa	8.06 GPa
0.8	11.7 GPa	0.9	2.9 GPa	10.4 GPa

Fig. 4-47: Stress-strain curve for different  $B_{sk}$  (P samples).

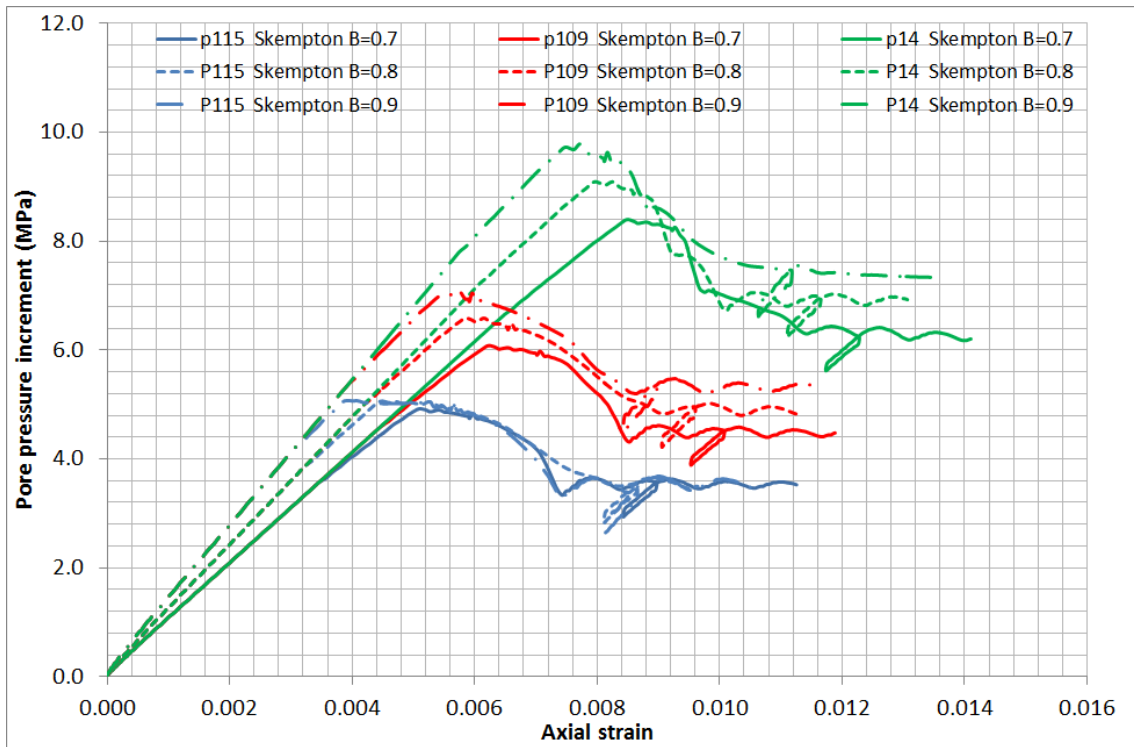


Fig. 4-48: Pore pressure increment for different  $B_{sk}$  (P samples).

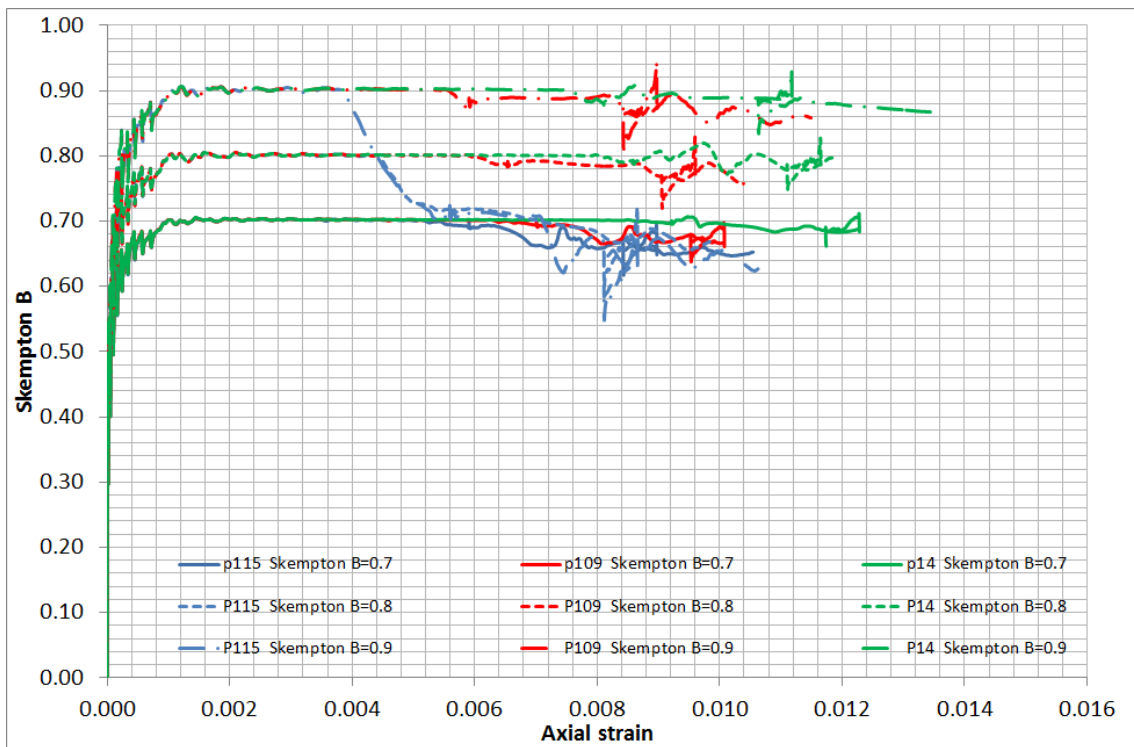


Fig. 4-49: Verification of  $B_{sk}$  for cases using different  $B_{sk}$  (P samples).

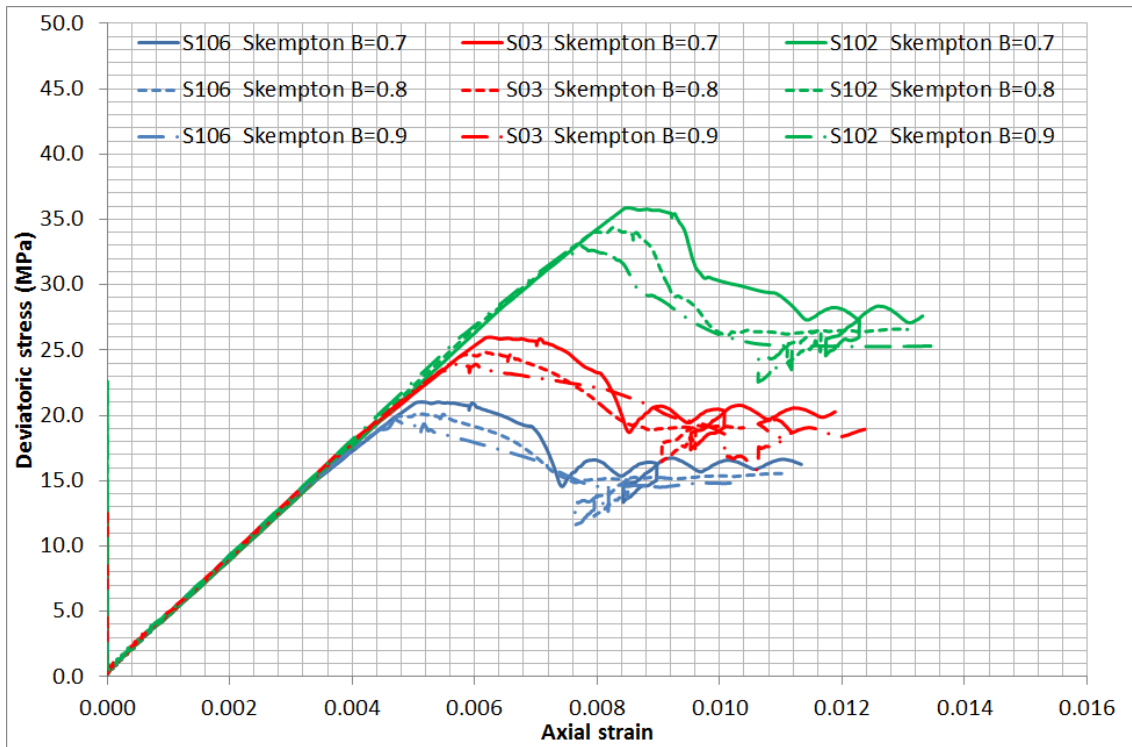


Fig. 4-50: Stress-strain curve for different  $B_{sk}$  (S samples).

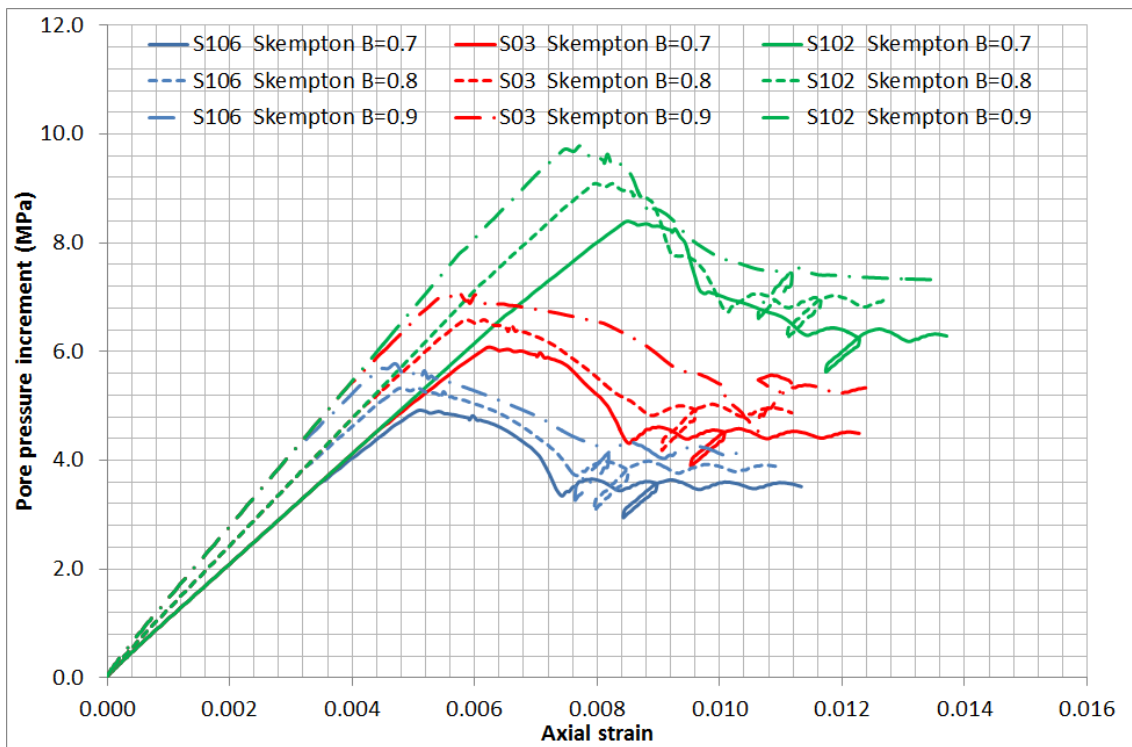


Fig. 4-51: Pore pressure increment for different  $B_{sk}$  (S samples).

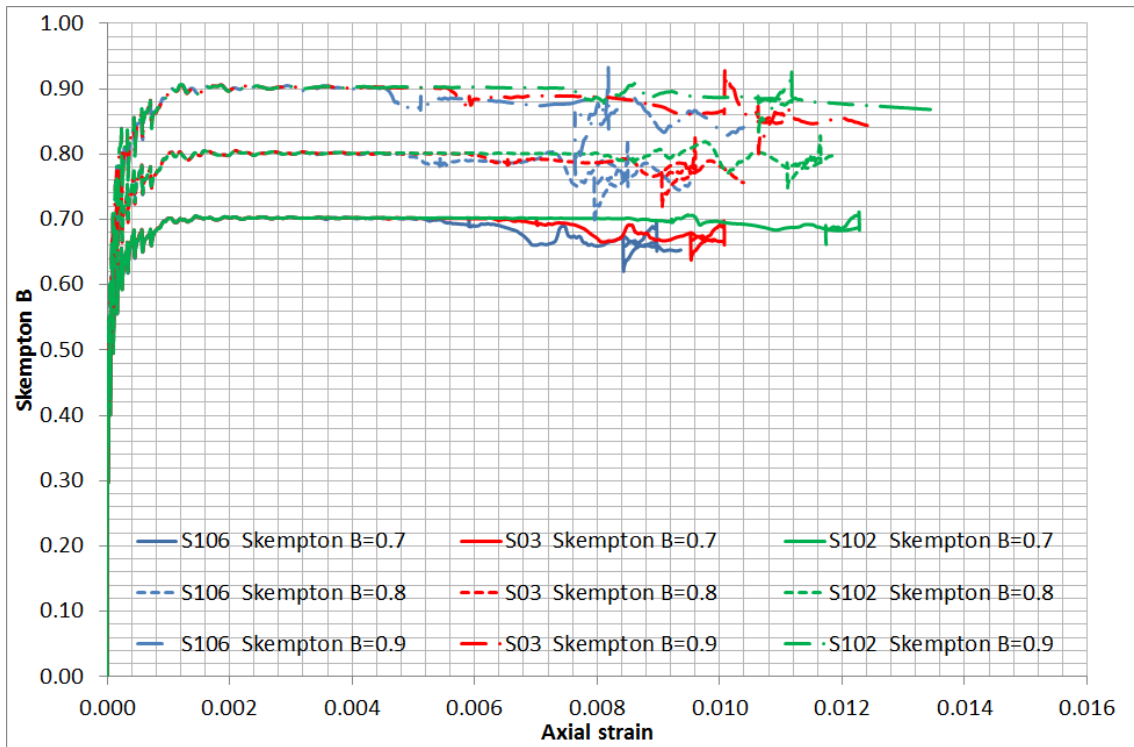


Fig. 4-52: Verification of  $B_{sk}$  for cases using different  $B_{sk}$  (S samples).

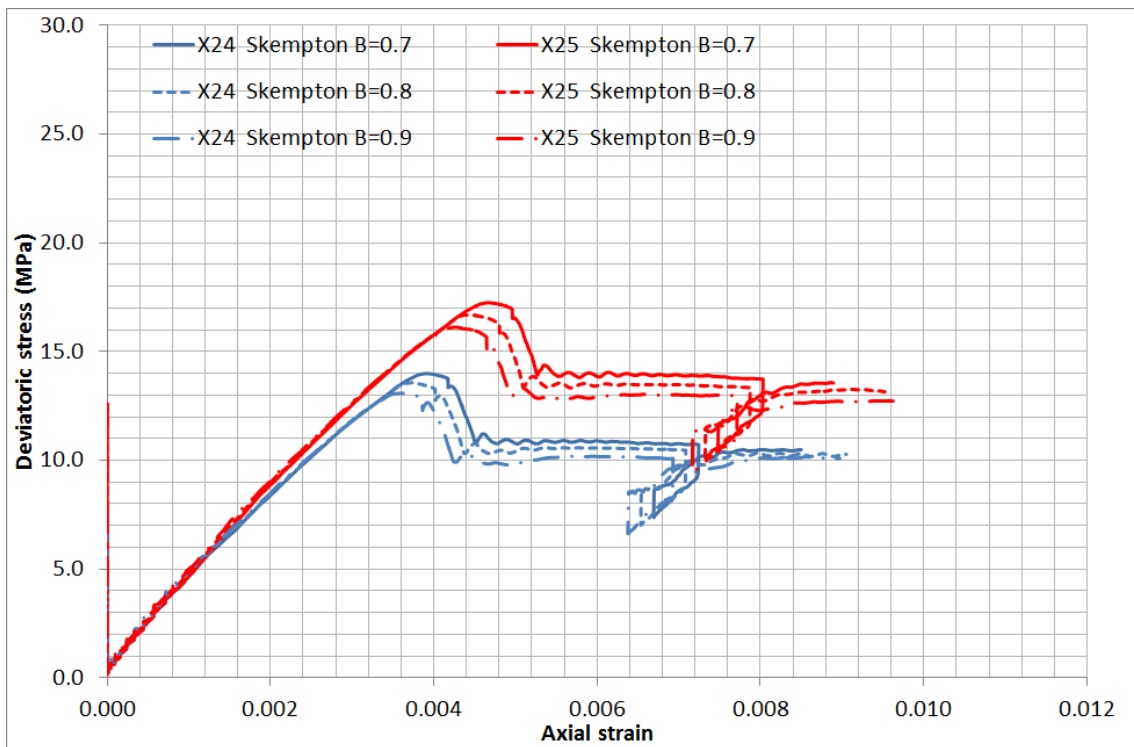


Fig. 4-53: Stress-strain curve for different  $B_{sk}$  (X samples).

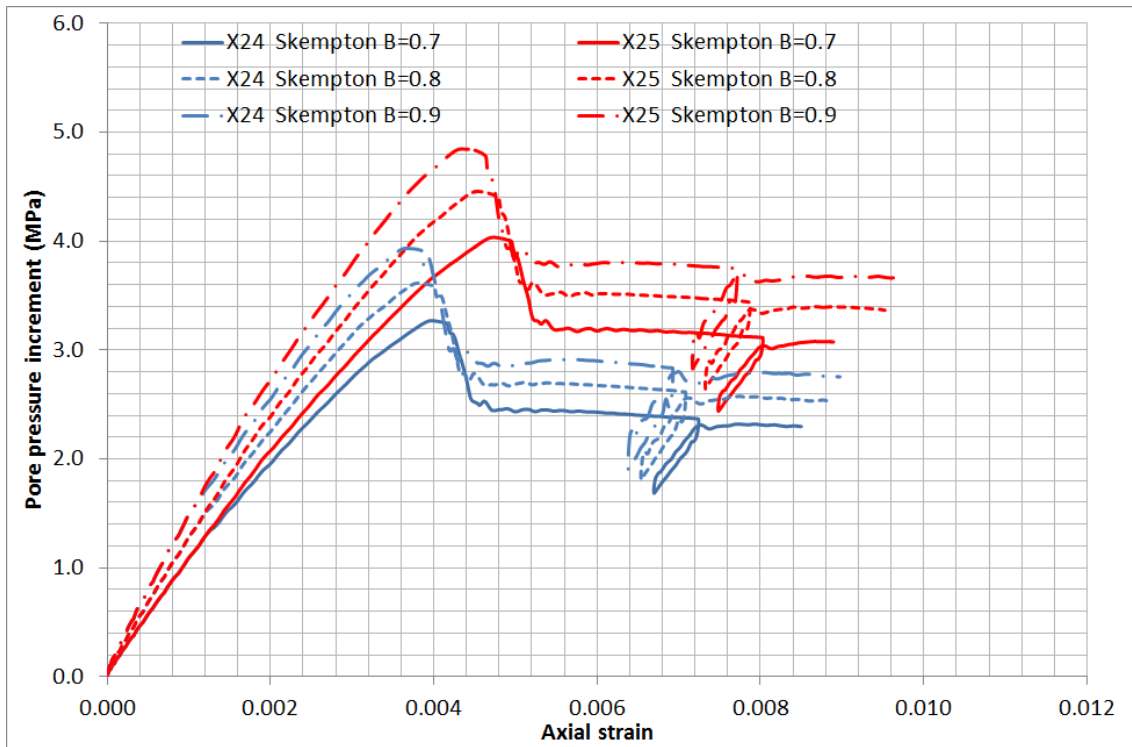


Fig. 4-54: Pore pressure increment for different  $B_{sk}$  (X samples).

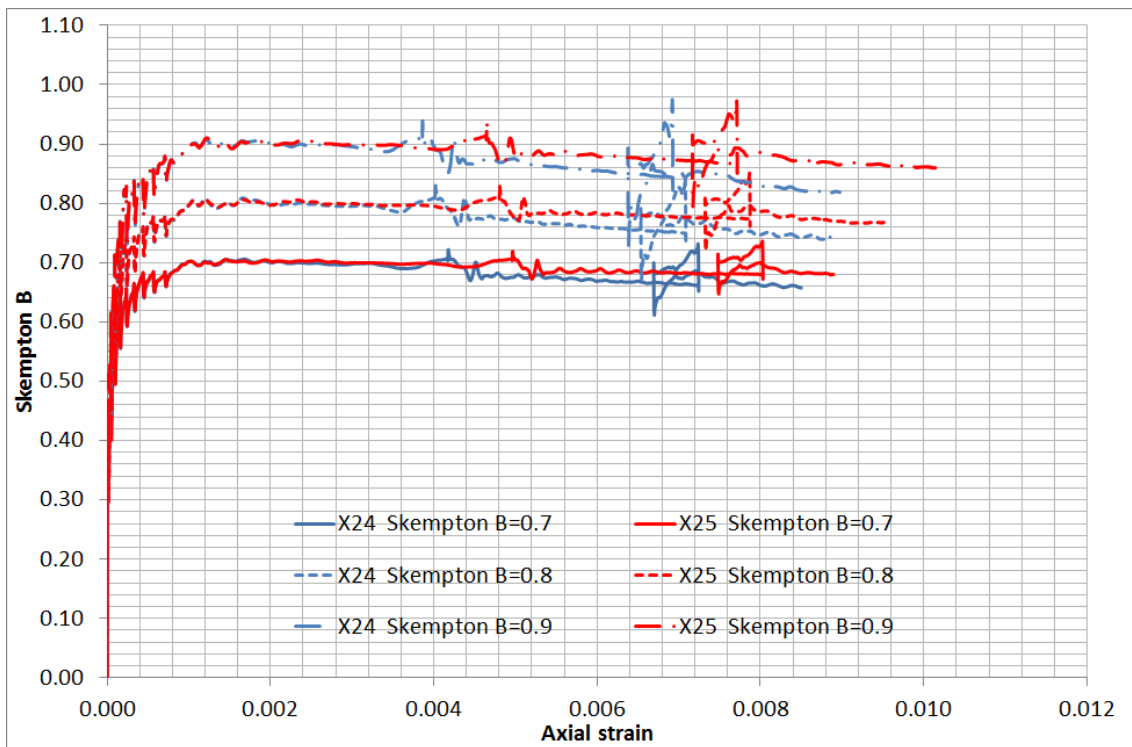


Fig. 4-55: Verification of  $B_{sk}$  for cases using different  $B_{sk}$  (X samples).



## 5 Comparison between FLAC3D and laboratory experiments

The results from sensitivity studies in Section 4 are used in this section to formulate two parameter sets as input to better reproduce the laboratory results. The two parameter sets both incorporate softening and hardening behaviour as investigated in Chapters 4.1 and 4.3, respectively, but they differ in the stiffness (i.e. different Young's modulus and coupling factor  $B_{sk}$ ).

### 5.1 Parameter set 1 – "stiff" Opalinus Clay

Table 5-1 gives the parameter set used. According to the experimental data (stress-strain curve and pore pressure increment),  $B_{sk}$  is fixed at 0.2. The Biot modulus ( $M = 2.6$  GPa) is adjusted in order to fit the Biot coefficient equal to 0.8. The results are presented from Figure 5-1 to Figure 5-20 for P, S, X and Z samples.

For P samples, the numerical results fit well the experimental data in terms of stress-strain curve and pore pressure increment. Shear bands are formed near the top and the bottom of the sample. The computed  $B_{sk}$  stays around 0.2, compared to an experimental value of 0.18. The computed  $B_{sk}$  for experimental data may jump to higher values when hysteretic loading takes place. This implies that the stress-strain curve, and the pore pressure increment, will not follow the same path during unloading and reloading. This explains the higher  $B_{sk}$  during the hysteretic loading when using Equation 4-6. The check of  $B_{sk}$  makes sense only for values computed from the stress-strain curve during the "normal" elastic loading part. Computed values *during* hysteretic loading and the post-peak should not be considered.

For S samples, the numerical results are not comparable to the experimental ones, for the same reason as described in Section 4.1.3. A further discussion is given in Section 5.2 where another numerical parameter set is used.

For X and Z samples, the numerical results show noticeable improvement for the early part of the stress-strain curve, before peak. Clearly, this comes from the change in the hardening behaviour (Section 4.3). For Z samples the numerical results agree well with the experimental data, in terms of stress-strain curve (Fig. 5-16). However, lower pore pressure increments are observed in the numerical model during post-peak (Fig. 5-18). For the X24 sample, the numerical simulation yields higher peak and residual strengths.

The computed  $B_{sk}$  values remain close to 0.2 for all numerical simulations whereas it ranges from 0.18 (P samples) to 0.5 (S03) in the experiments. As with the strength and pore pressure data, the fits for the  $B_{sk}$  values using the "stiff" parameter set are much better for P Samples than for S Samples.

Tab. 5-1: "Stiff" parameter set for the FLAC3D model.

Young's modulus (drained)	12 GPa
Biot coefficient	0.8
Biot modulus	2.6 GPa
Skempton $B_{sk}$	0.2

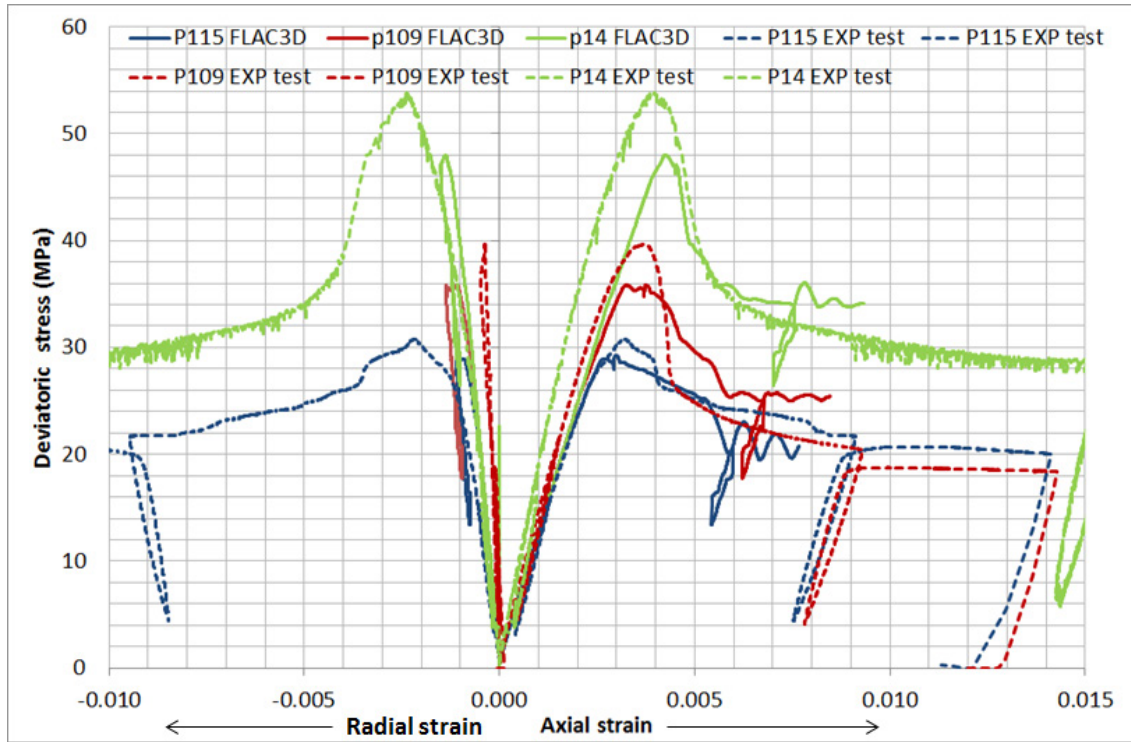


Fig. 5-1: Comparison of stress-strain evolution between FLAC3D and laboratory experiments for P samples (stiff parameter set).

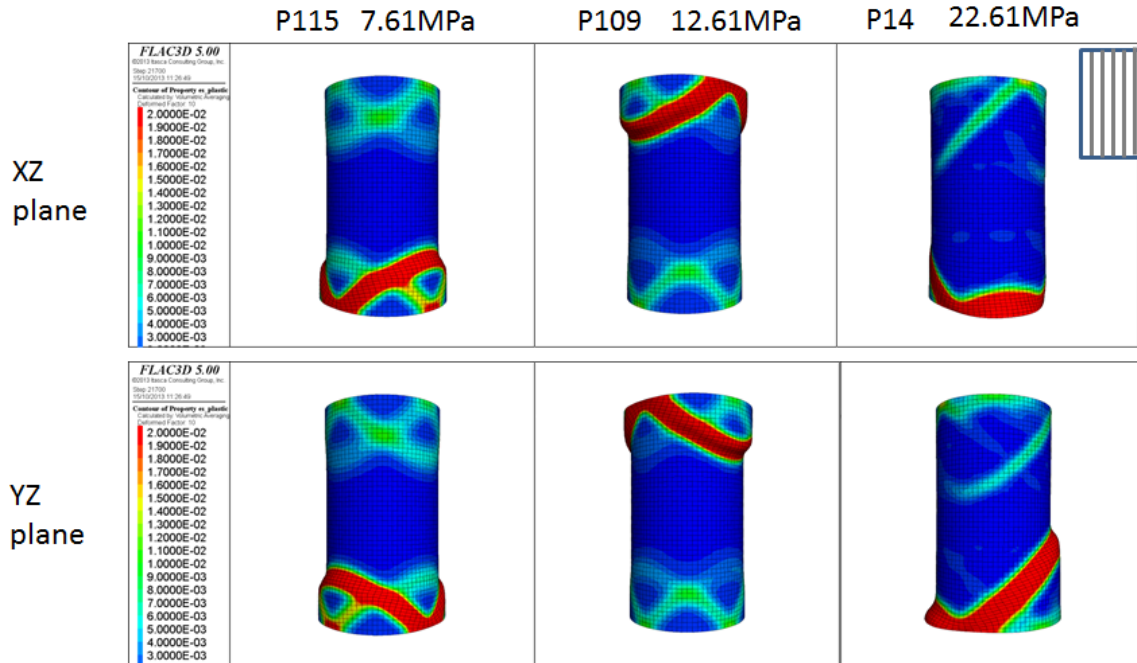


Fig. 5-2: Matrix plastic shear strain at the end of the test for P samples (stiff parameter set).

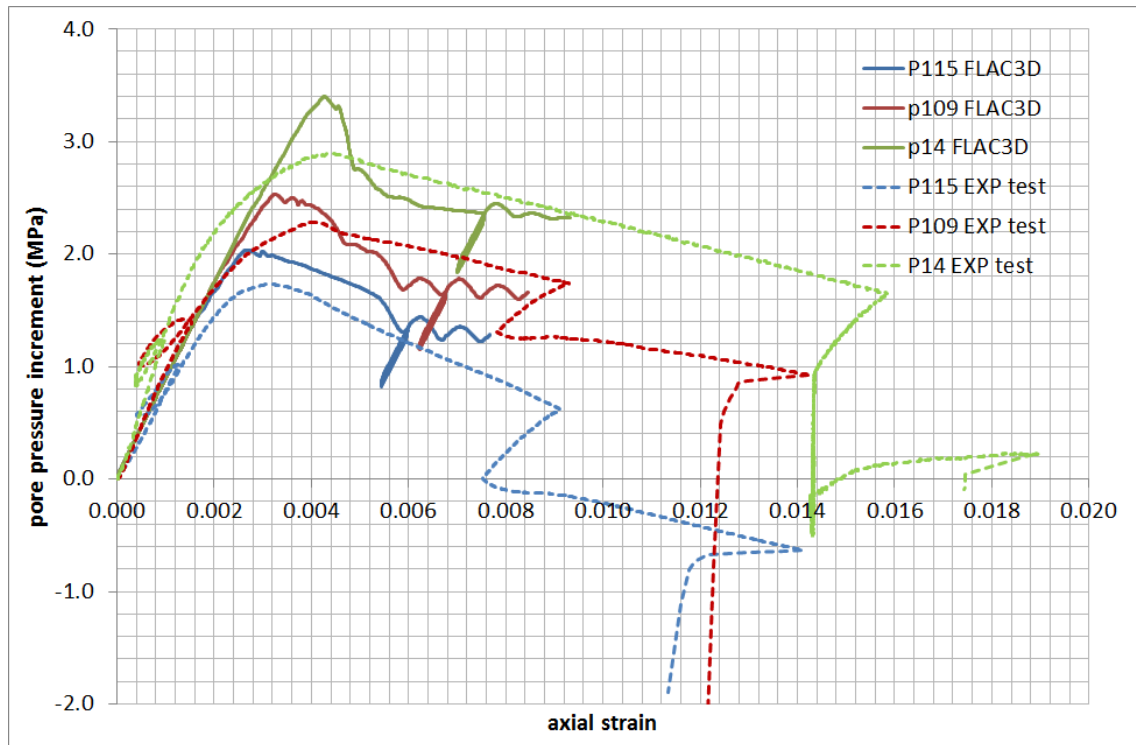


Fig. 5-3: Pore pressure increments comparison between FLAC3D and laboratory experiments for P samples (stiff parameter set).

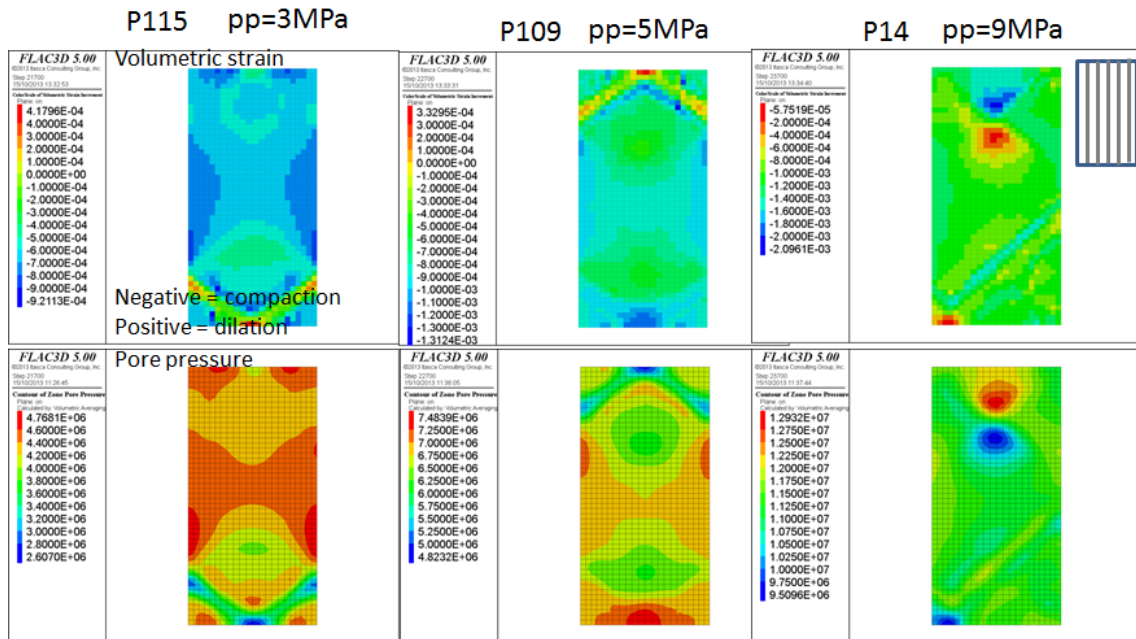


Fig. 5-4: Volumetric strain and pore pressure for P samples (stiff parameter set) YZ cutting plane shown.

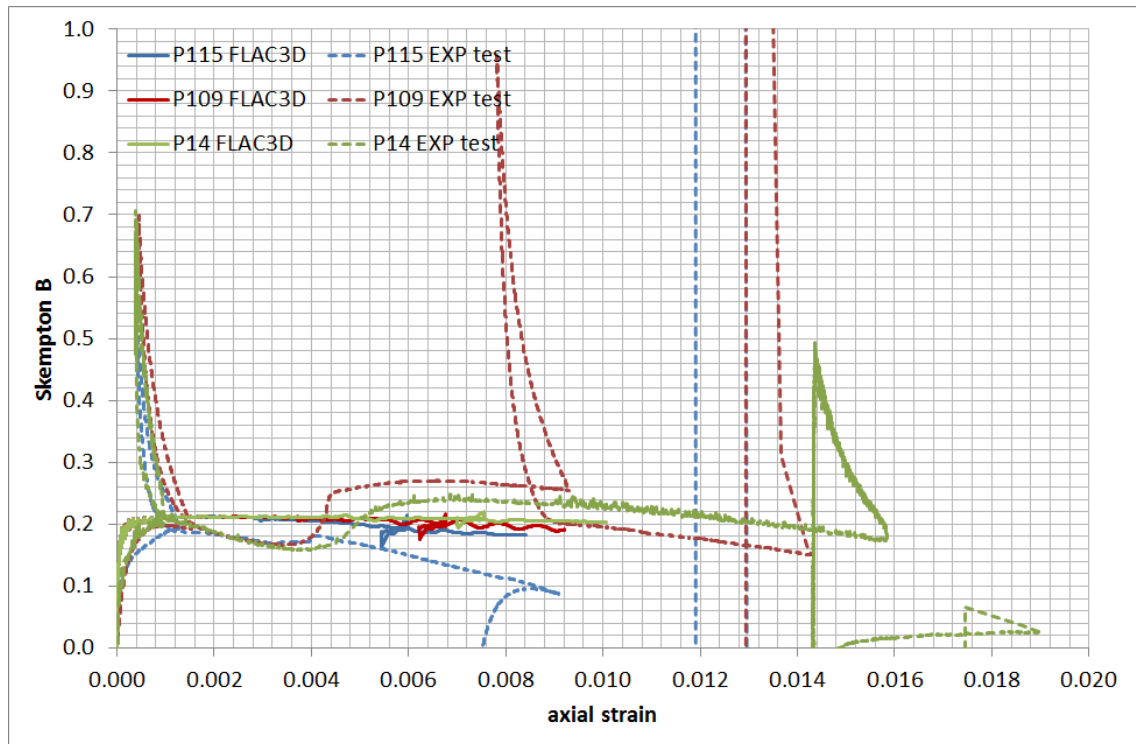


Fig. 5-5: Comparison of  $B_{sk}$  between FLAC3D and laboratory experiments for P samples (stiff parameter set).

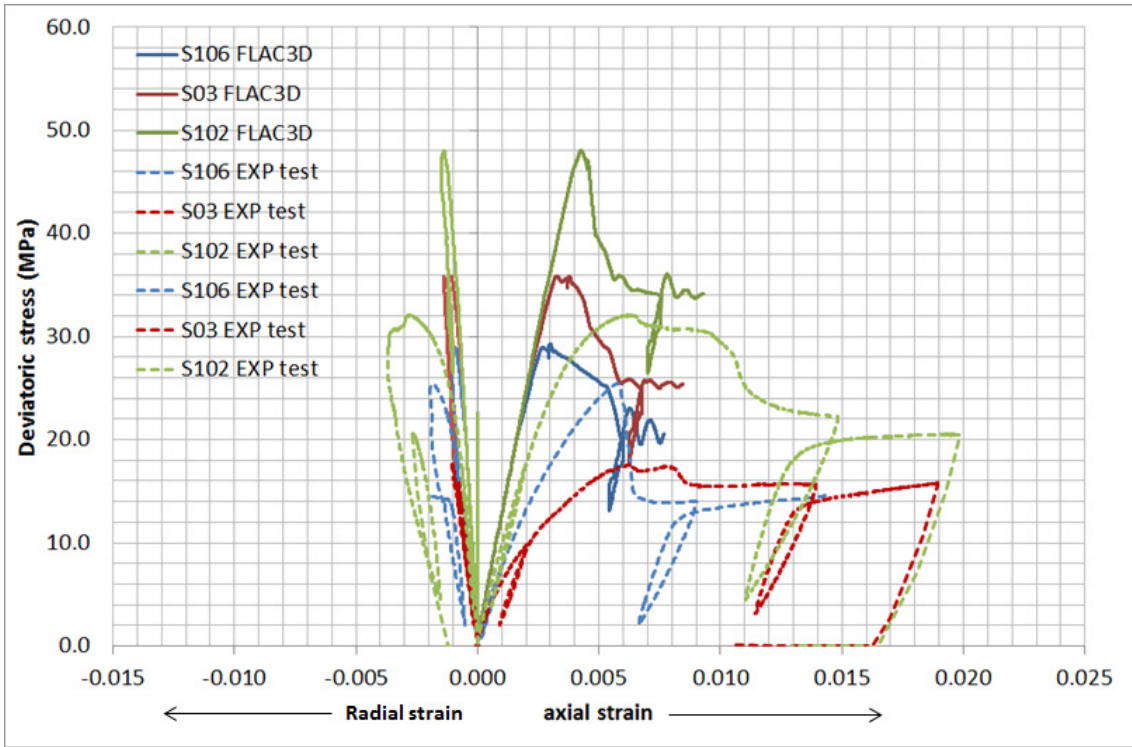


Fig. 5-6: Comparison of stress-strain evolution between FLAC3D and laboratory experiments for S samples (stiff parameter set).

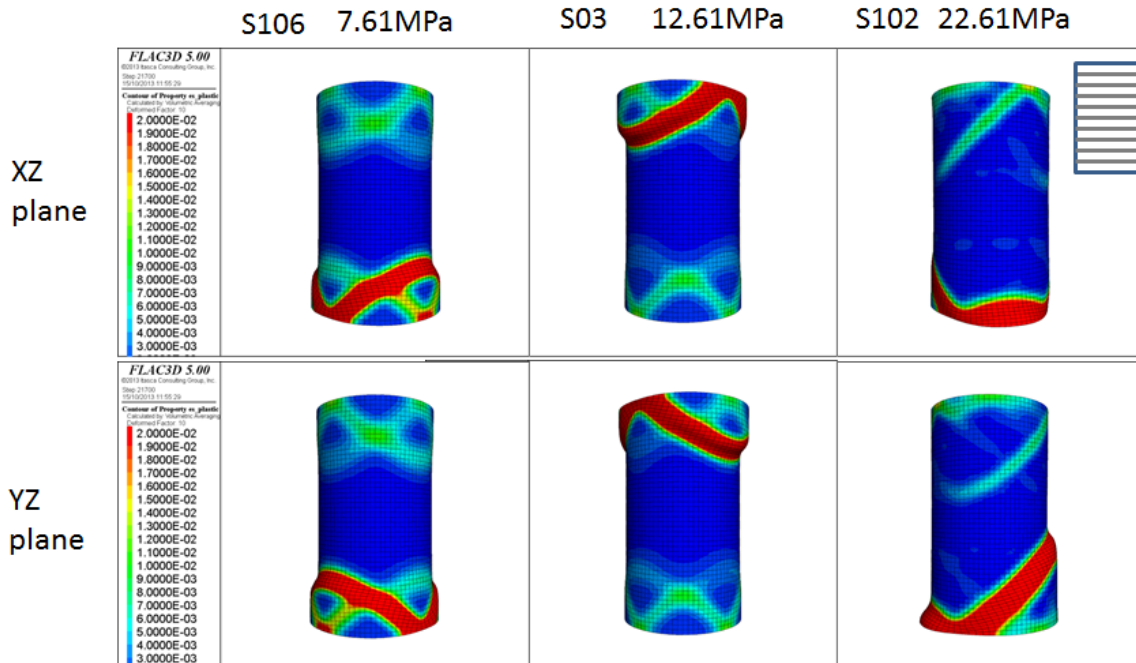


Fig. 5-7: Matrix plastic shear strain at the end of the test for S samples (stiff parameter set).

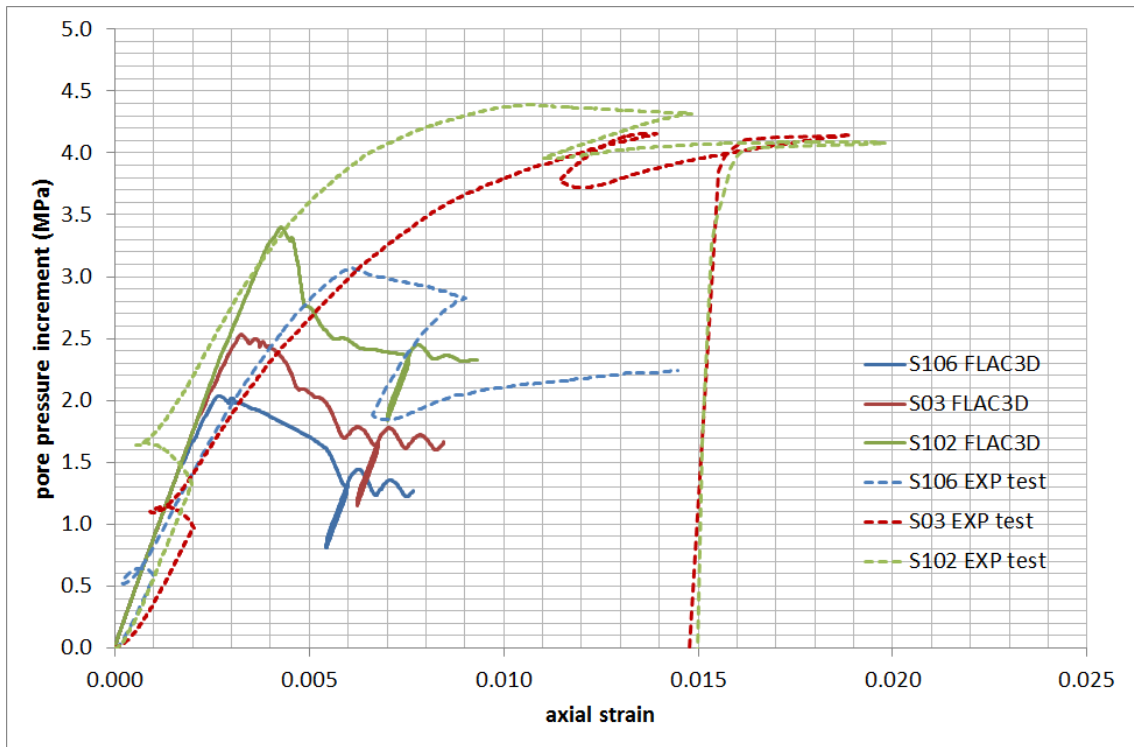


Fig. 5-8: Pore pressure increments comparison between FLAC3D and laboratory experiments for S samples (stiff parameter set).

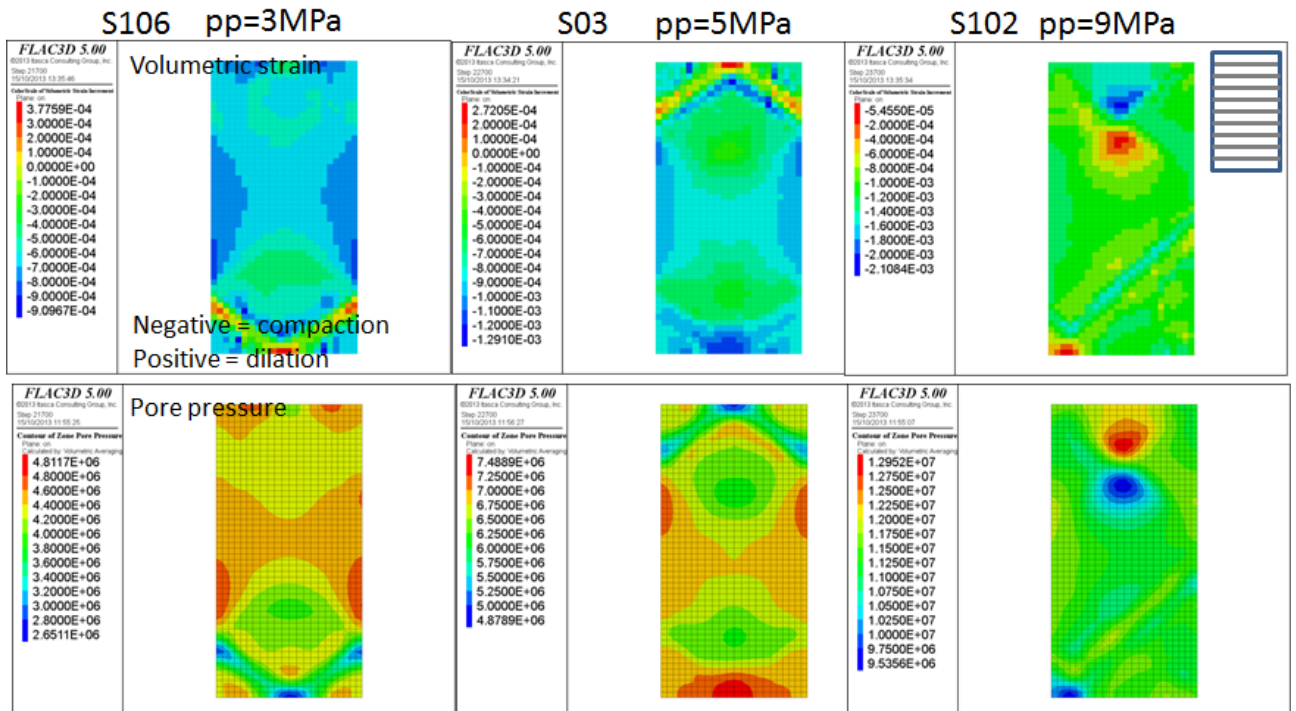


Fig. 5-9: Volumetric strain and pore pressure for S samples (stiff parameter set). YZ cutting plane shown.

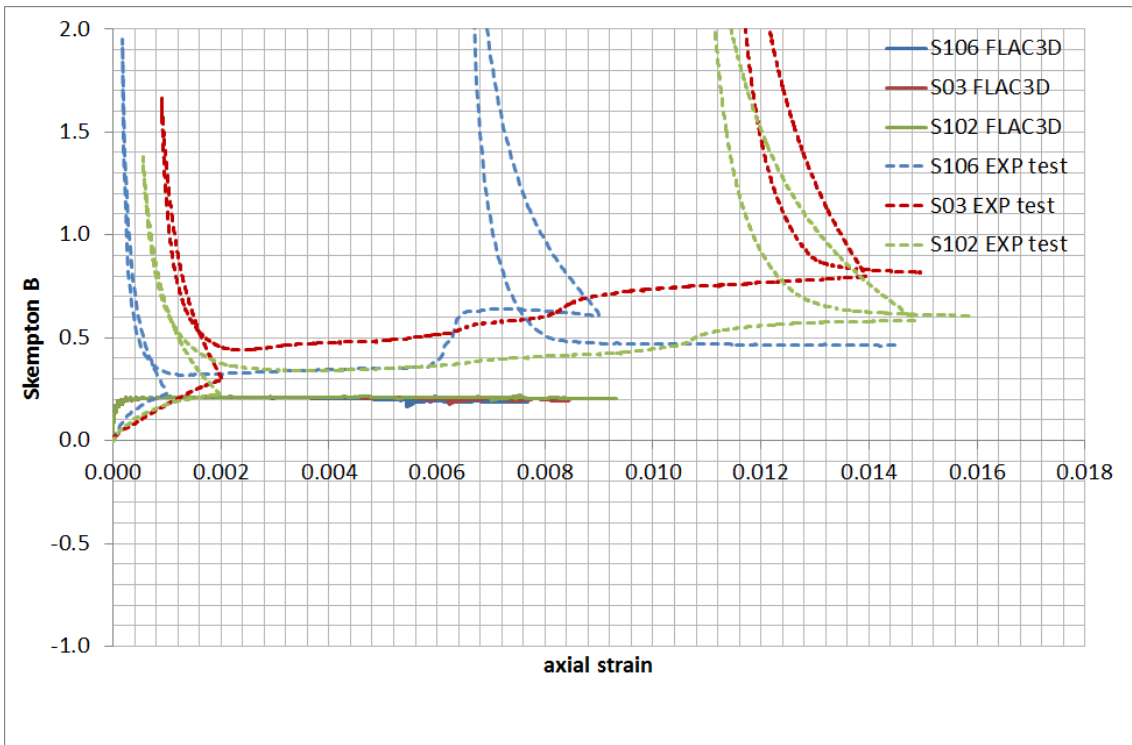


Fig. 5-10: Comparison of  $B_{sk}$  between FLAC3D and laboratory experiments for S samples (stiff parameter set).

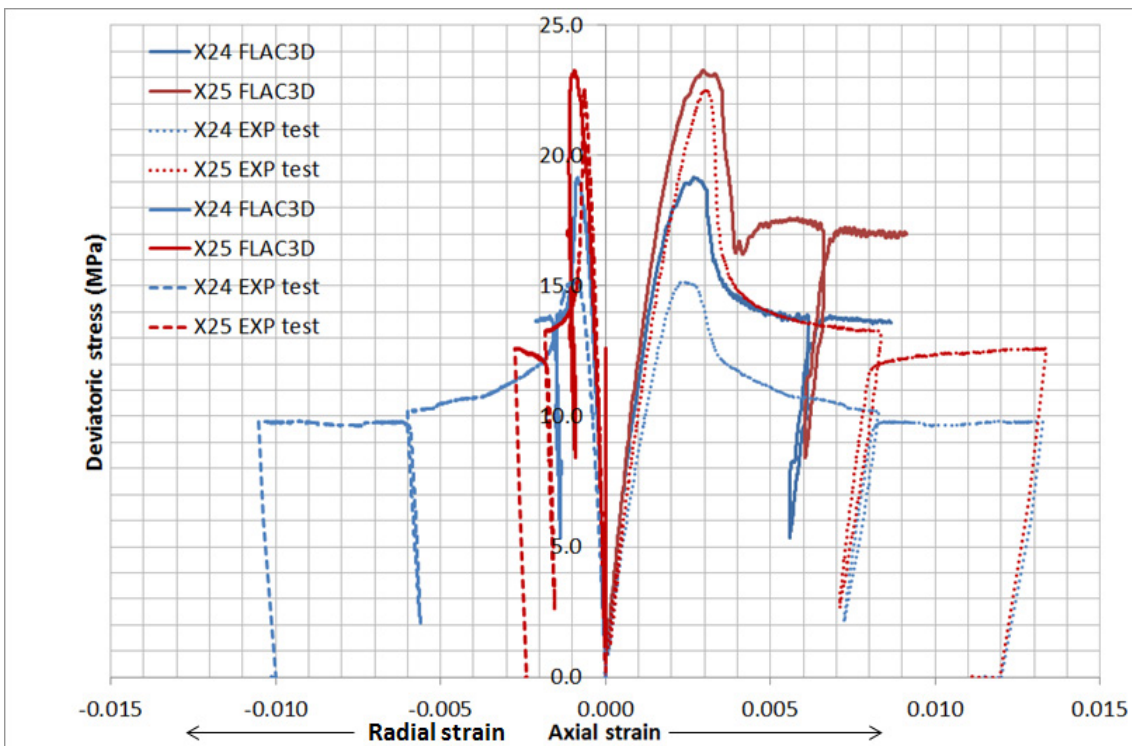


Fig. 5-11: Comparison of stress-strain evolution between FLAC3D and laboratory experiments for X samples (stiff parameter set).

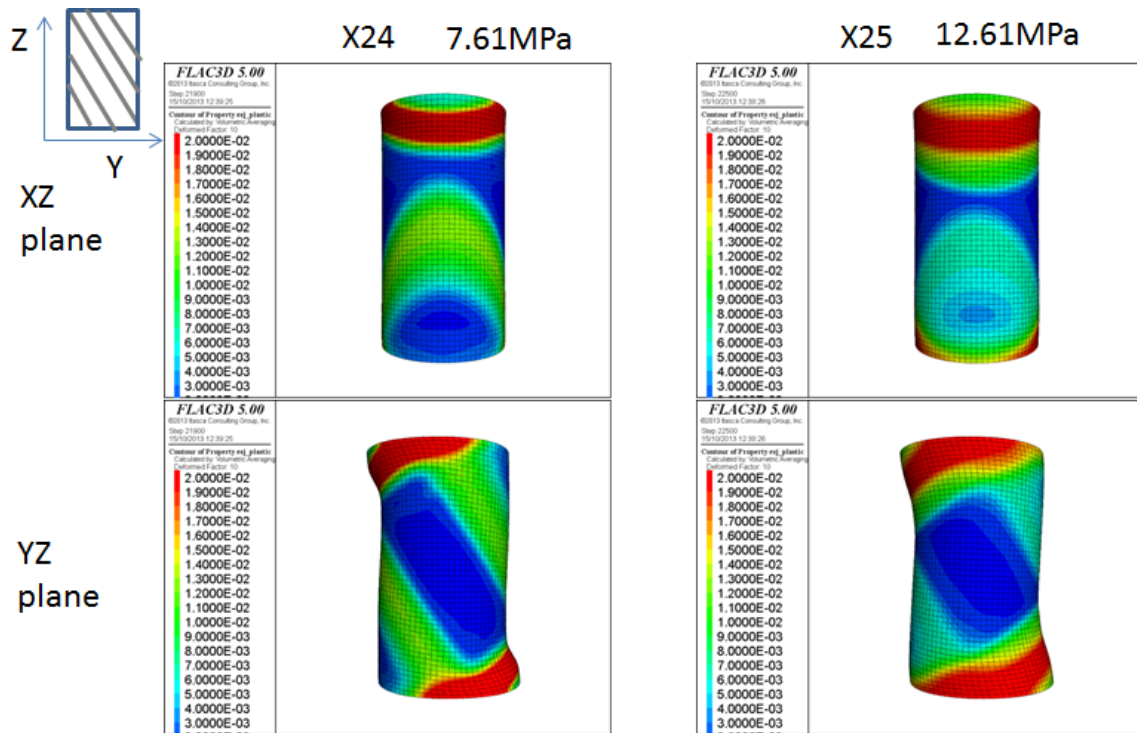


Fig. 5-12: Bedding plastic shear strain at the end of the test for X samples (stiff parameter set).

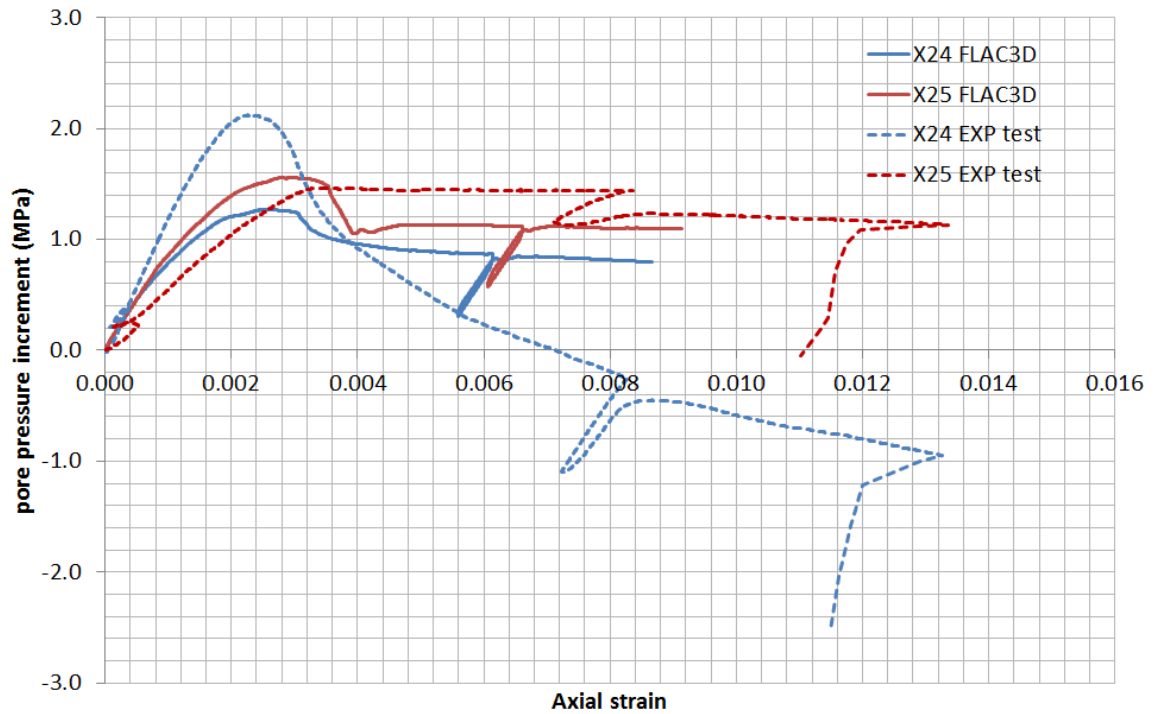


Fig. 5-13: Pore pressure increments comparison between FLAC3D and laboratory experiments for X samples (stiff parameter set).

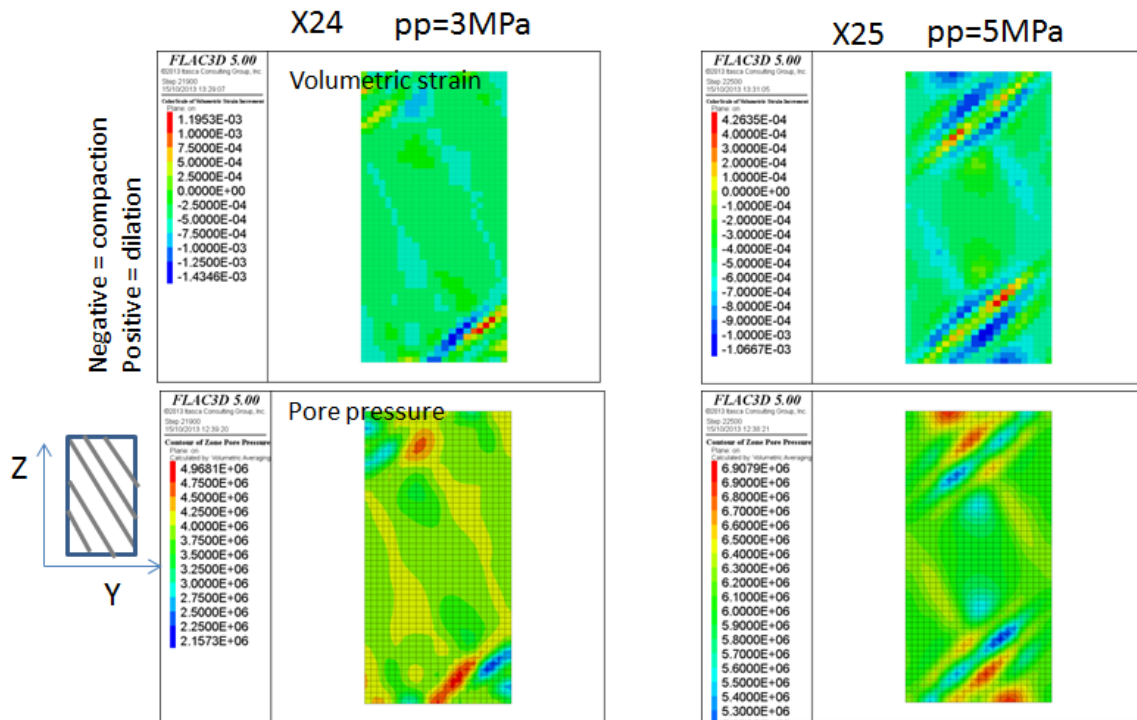


Fig. 5-14: Volumetric strain and pore pressure for X samples (stiff parameter set). YZ cutting plane shown.

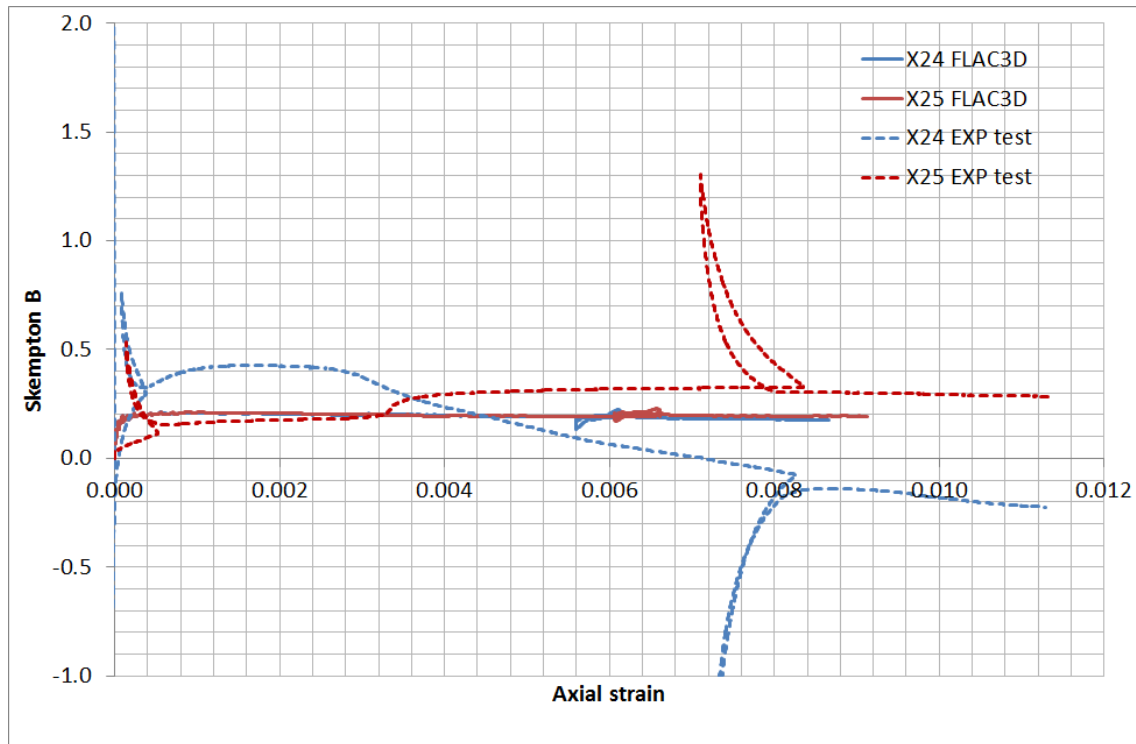


Fig. 5-15: Comparison of  $B_{sk}$  between FLAC3D and laboratory experiments for X samples (stiff parameter set).

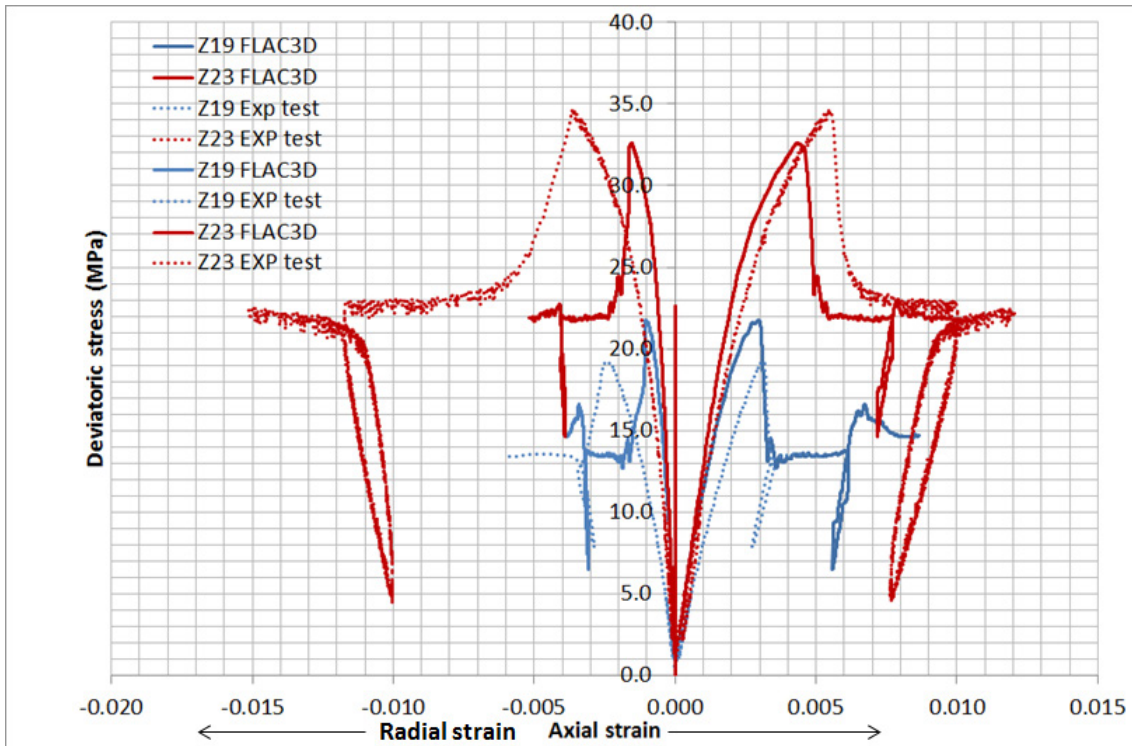


Fig. 5-16: Comparison of stress-strain evolution between FLAC3D and laboratory experiments for Z samples (stiff parameter set).

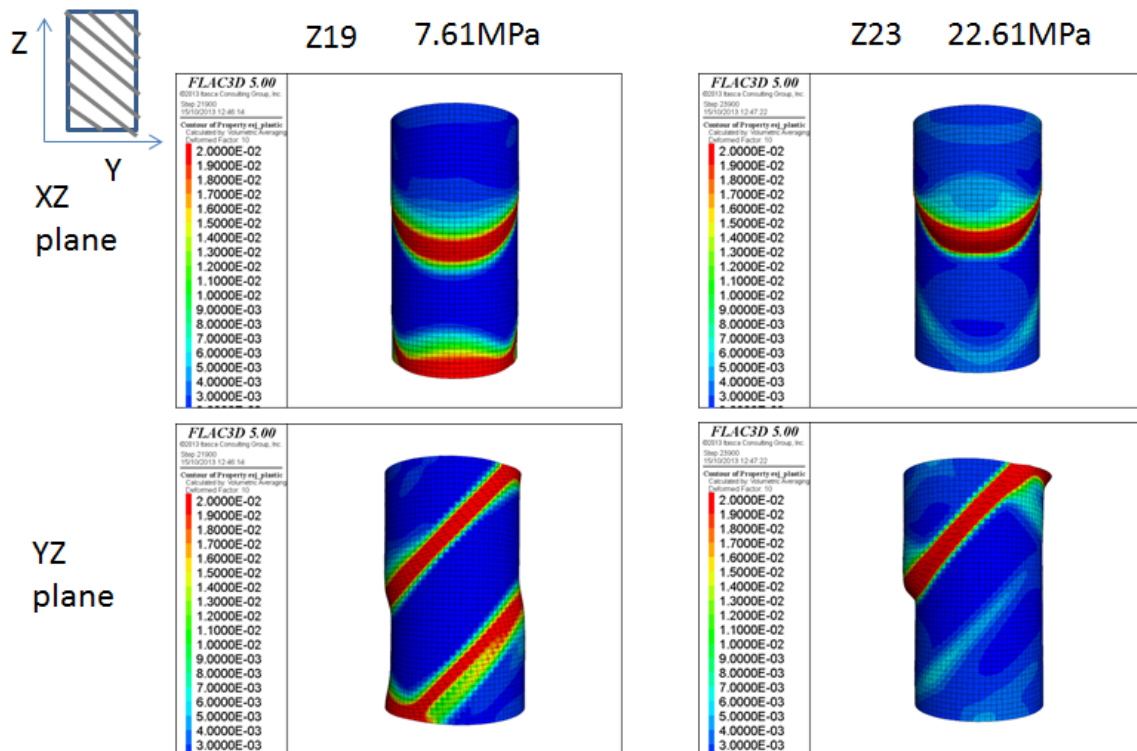


Fig. 5-17: Bedding plastic shear strain at the end of the test for Z samples (stiff parameter set).

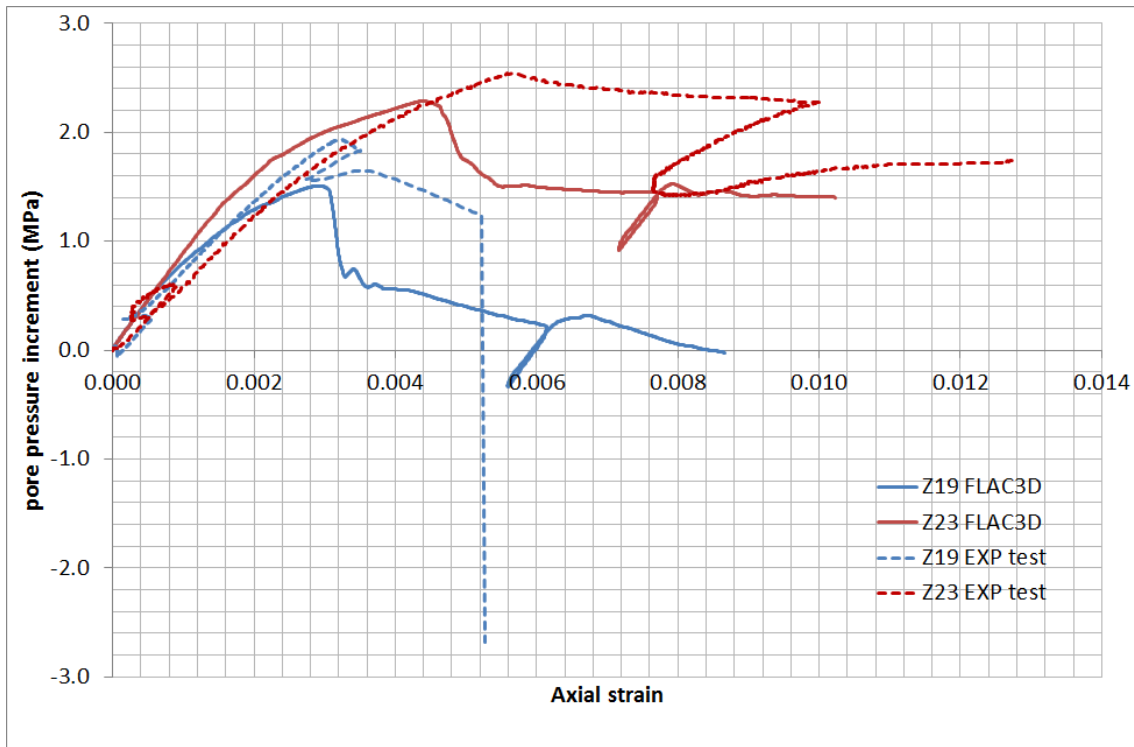


Fig. 5-18: Pore pressure increments comparison between FLAC3D and laboratory experiments for Z samples (stiff parameter set).

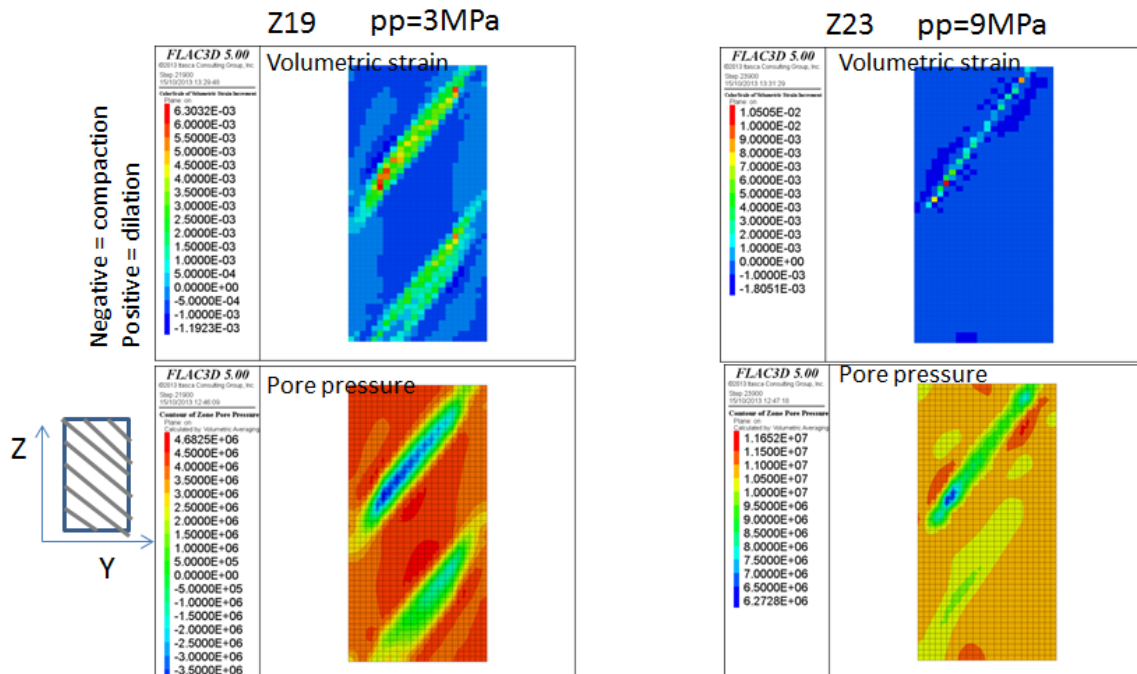


Fig. 5-19: Volumetric strain and pore pressure for Z samples (stiff parameter set). YZ cutting plane shown.

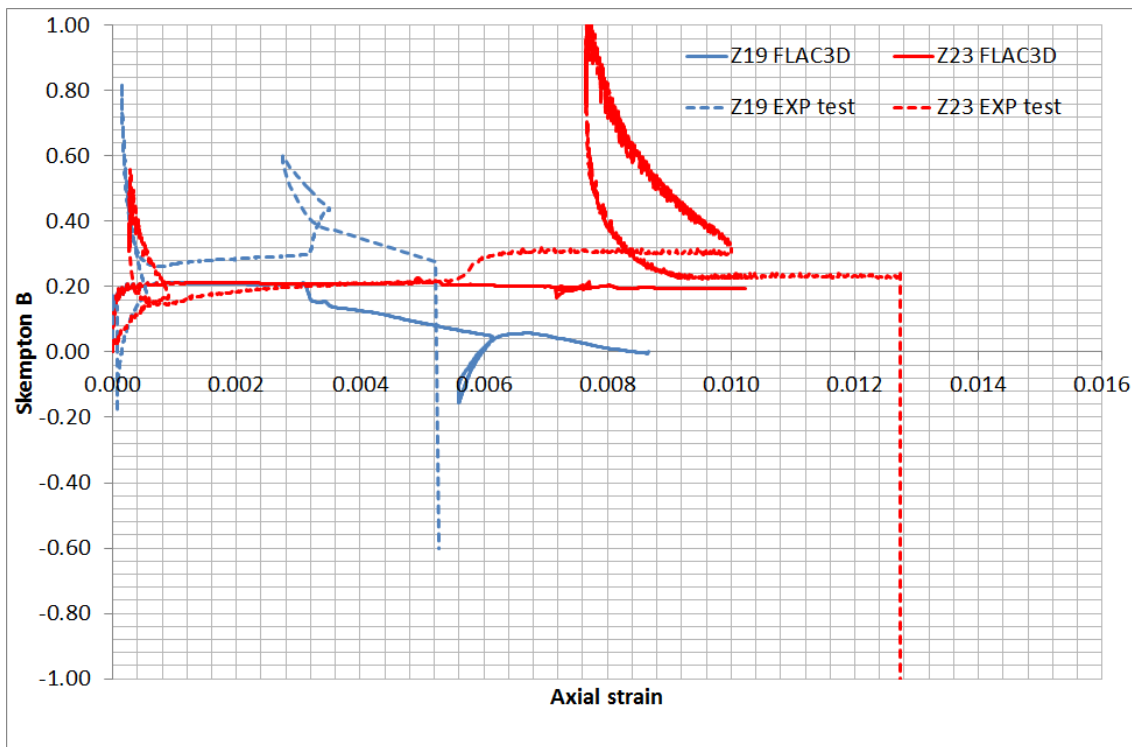


Fig. 5-20: Comparison of  $B_{sk}$  between FLAC3D and laboratory experiments for Z samples (stiff parameter set).

## 5.2 Parameter set 2 – "soft" Opalinus Clay

Table 5-2 shows the parameter set for numerical simulation where  $B_{sk}$  is fixed at 0.9 and the Biot modulus is 11.7 GPa. As mentioned before, the drained Young's modulus is set to 4 GPa, instead of 12 GPa for previous simulations.

The results are presented in terms of stress-strain evolution, pore pressure increment and  $B_{sk}$  from Figure 5-21 to Figure 5-32. In order to better compare the change in stress (and in pore pressure) when changing the Young's modulus (and  $B_{sk}$ ), previous results obtained from cases using lower  $B_{sk}$  are also presented.

For S samples, numerical stress-strain curves using a smaller Young's modulus are closer to the experimental results (Fig. 5-21). However, as should be expected, higher pore pressures are computed for the cases using  $B = 0.9$  (Fig. 5-23). It is noted that pore pressure increments recorded in laboratory experiments may deviate quite significantly from actual values inside the samples due to the long pressure equilibration period required in low-permeability rocks such as Opalinus Clay. Recall that pore pressures in the laboratory are measured at the end faces of cylindrical samples. The shear band formation (Fig. 5-22) and the pore pressure distribution (Fig. 5-24) are very similar to those obtained from the "stiff" data using a smaller  $B_{sk}$  (Chapter 5.1). The different evolution of stress and pore pressure increments with strain as a function of the parameter set used is also documented for P-samples in Figs. 5-26 and 5-27.

Tab. 5-2: "Soft" parameter set for the FLAC3D model.

Young's modulus (drained)	4 GPa
Biot coefficient	0.8
Biot modulus	11.7 GPa
$B_{sk}$	0.9

Figs. 5-28 and 5-30 compare the "X numerical" and "X experimental" results. The increase in  $B_{sk}$  yields higher pore pressure increments, which tends to reduce the peak and residual strengths. Meanwhile, the residual strength is better fitted for cases using softer Young's modulus (Fig. 5-28). Finally, the different evolution of stress and pore pressure increments with strain as a function of the parameter set used is documented for Z-samples in Figs. 5-31 and 5-32, respectively.

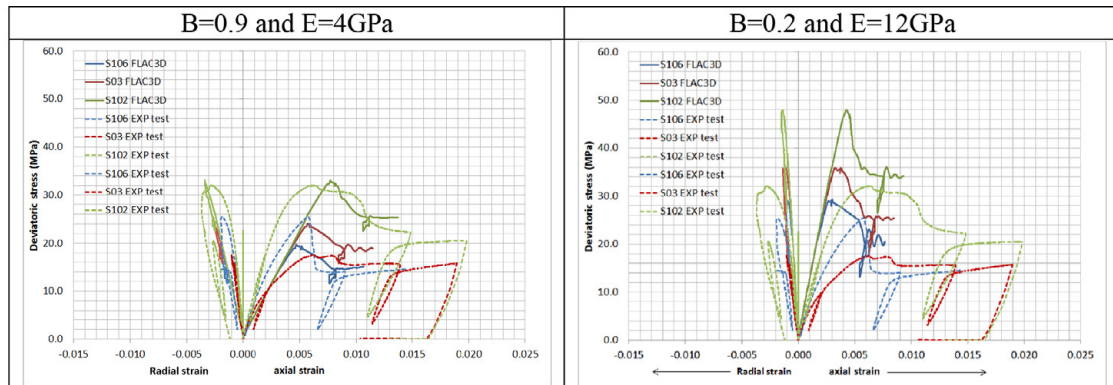


Fig. 5-21: Comparison of stress-strain evolution between FLAC3D and laboratory experiments for S samples.

Left: soft parameter set. Right: stiff parameter set.

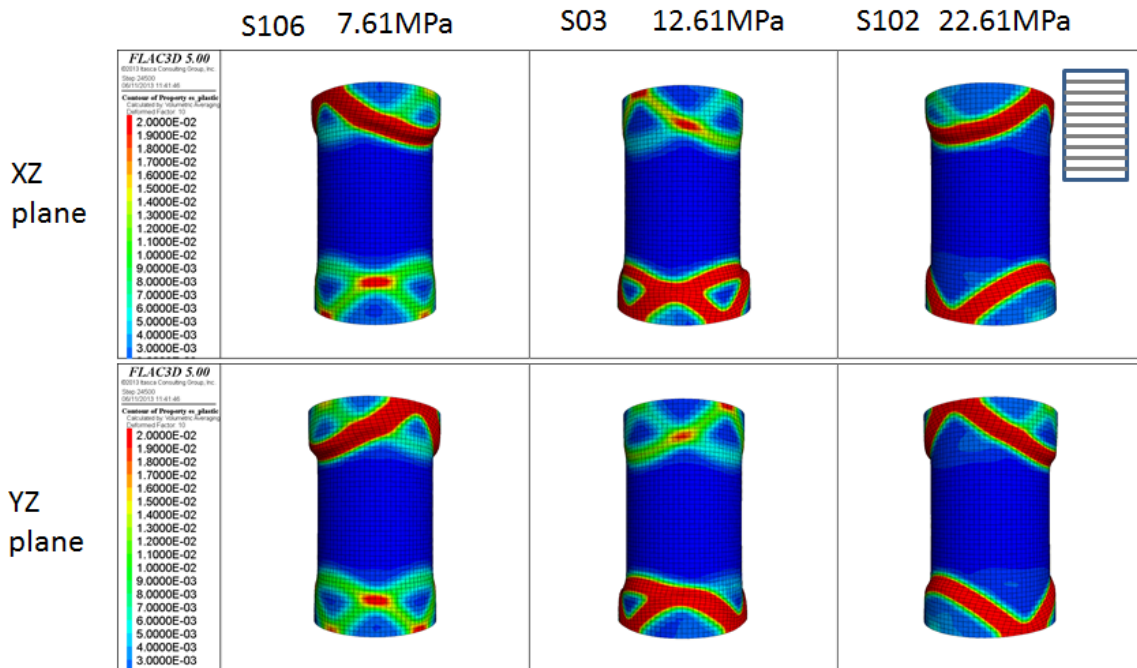


Fig. 5-22: Matrix plastic shear strain at the end of the test for S samples (soft parameter set).

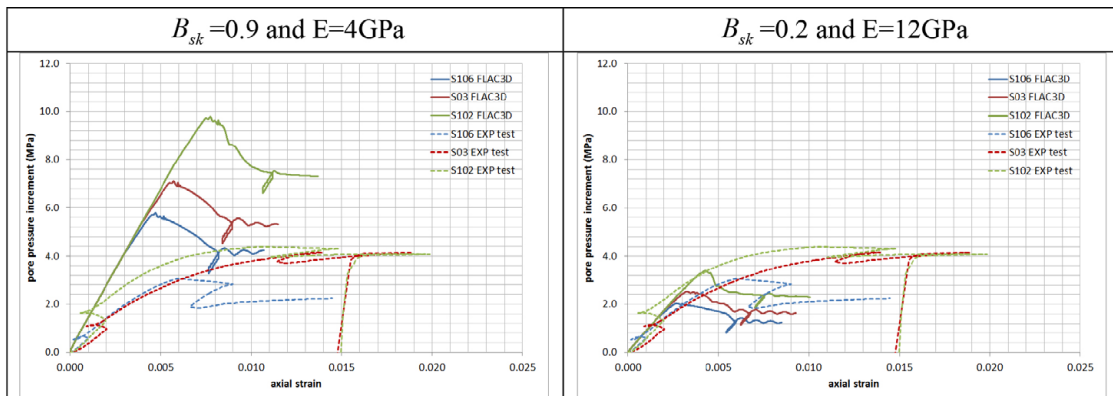


Fig. 5-23: Pore pressure increments comparison between FLAC3D and laboratory experiments for S samples.

Left: soft parameter set. Right: stiff parameter set.

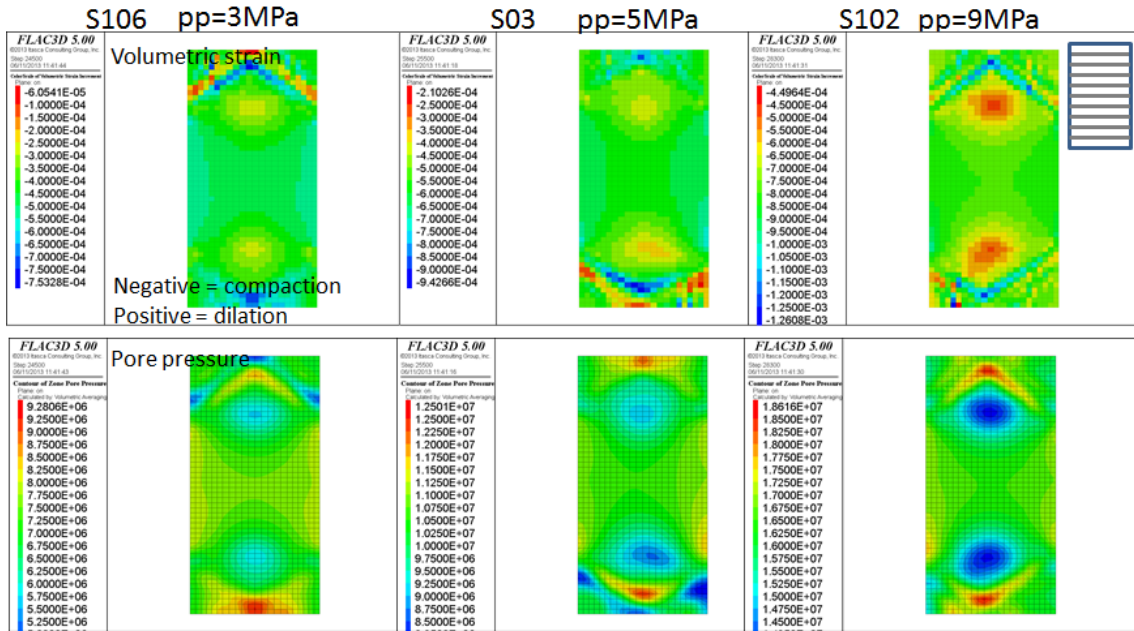


Fig. 5-24: Volumetric strain and pore pressure for S samples (soft parameter set). YZ cutting plane shown.

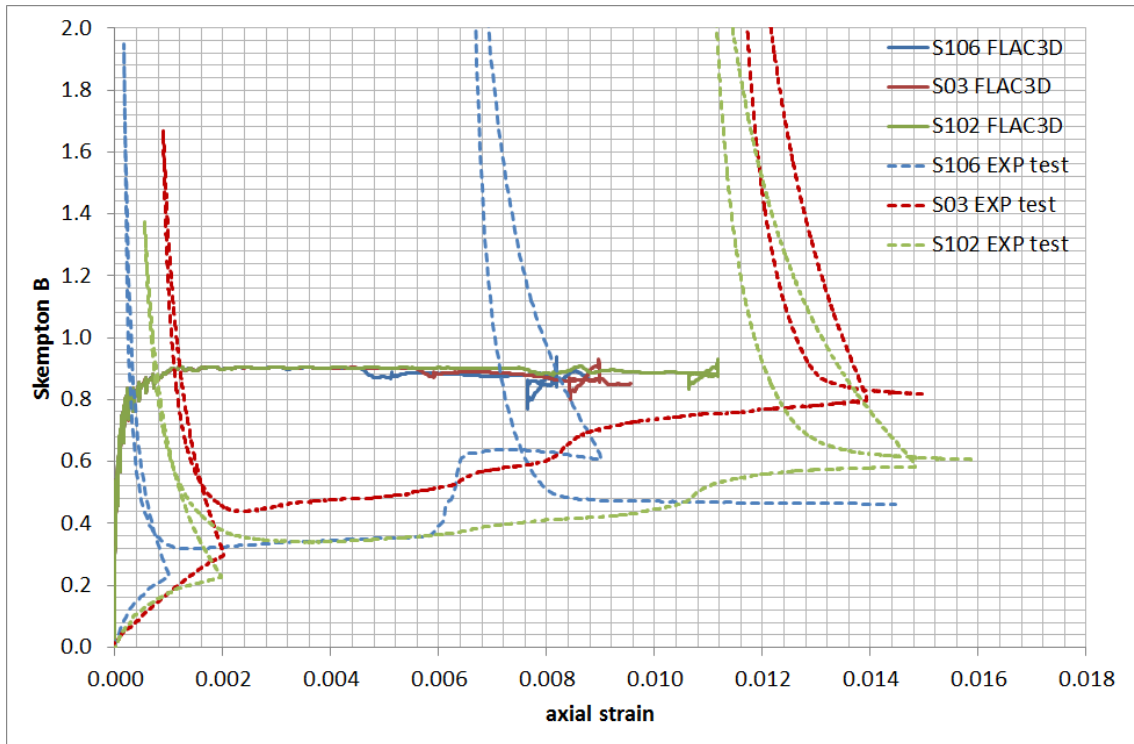


Fig. 5-25: Comparison of  $B_{sk}$  between FLAC3D and laboratory experiments for S samples (soft parameter set).

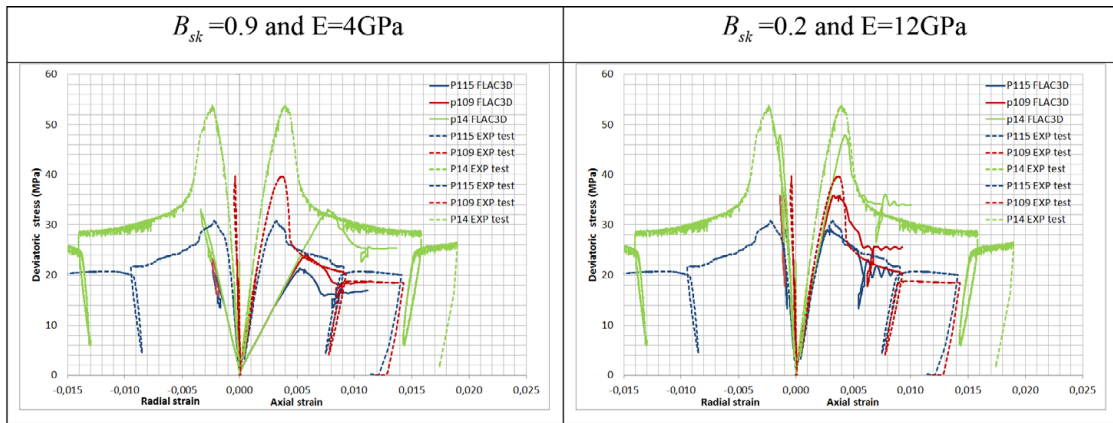


Fig. 5-26: Comparison of stress-strain evolution between FLAC3D and laboratory experiments for P samples.

Left: soft parameter set. Right: stiff parameter set.

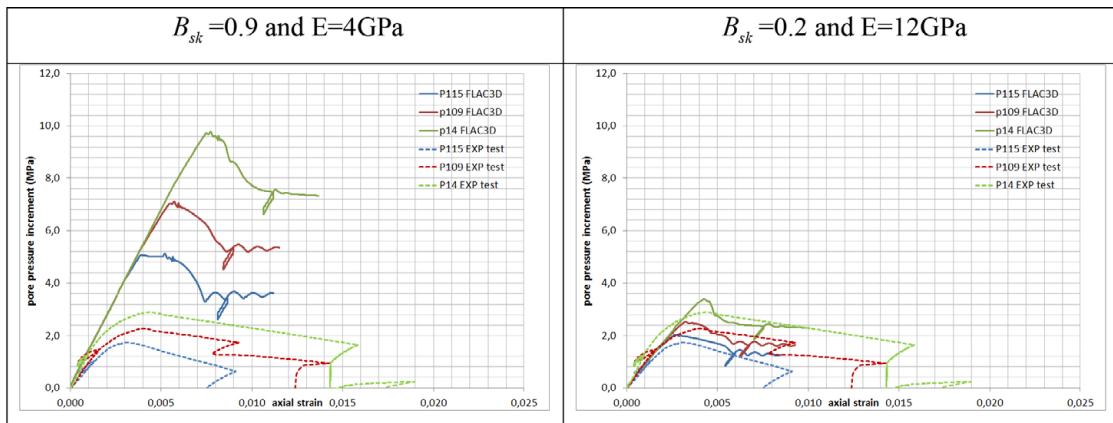


Fig. 5-27: Pore pressure increments comparison between FLAC3D and laboratory experiments for P samples.

Left: soft parameter set. Right: stiff parameter set.

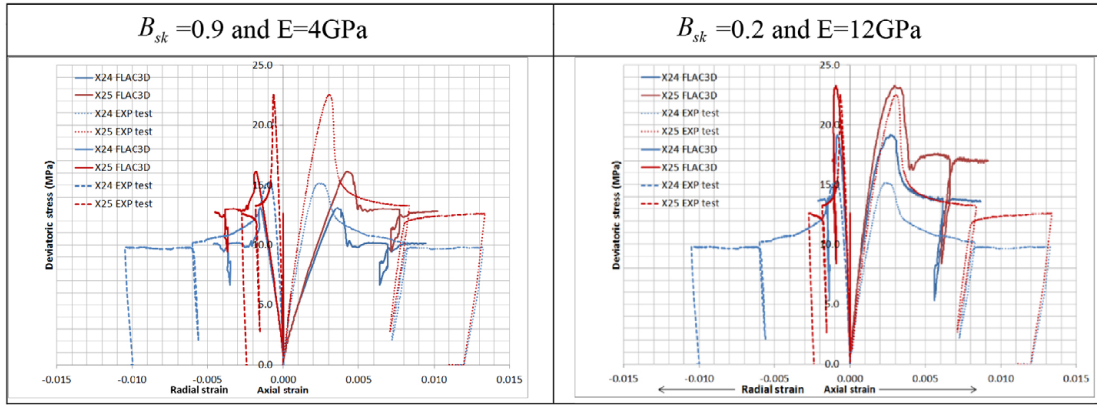


Fig. 5-28: Comparison of stress-strain evolution between FLAC3D and laboratory experiments for X samples.

Left: soft parameter set. Right: stiff parameter set.

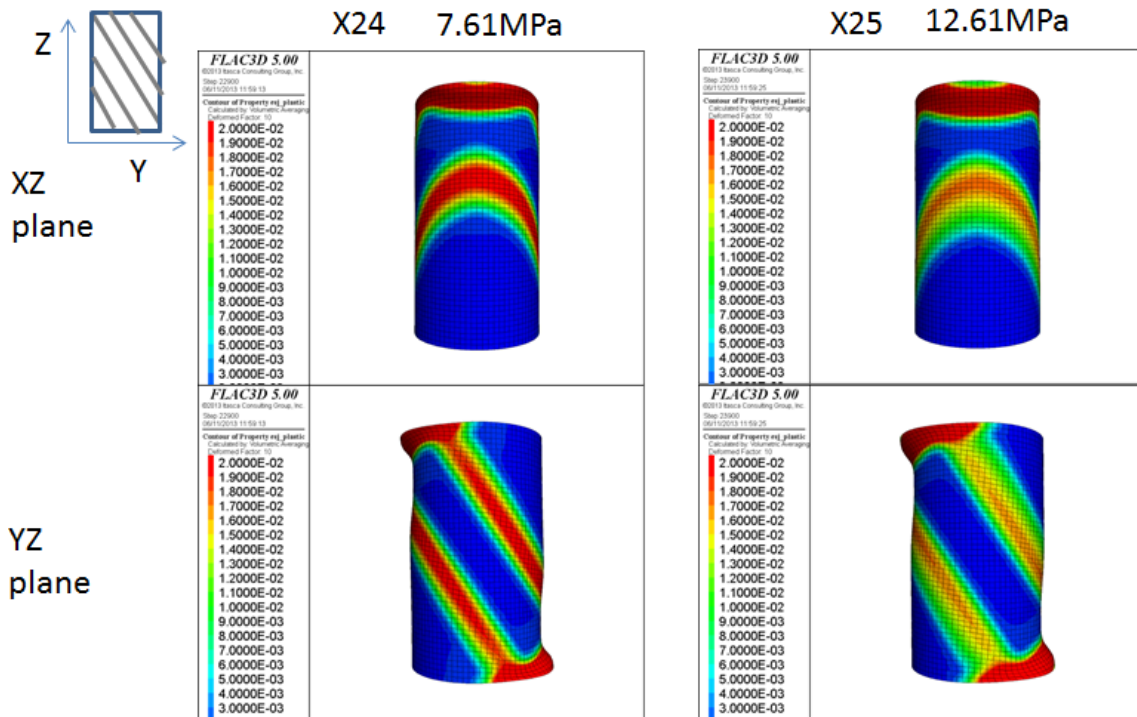


Fig. 5-29: Bedding plastic shear strain at the end of the test for X samples (soft parameter set).

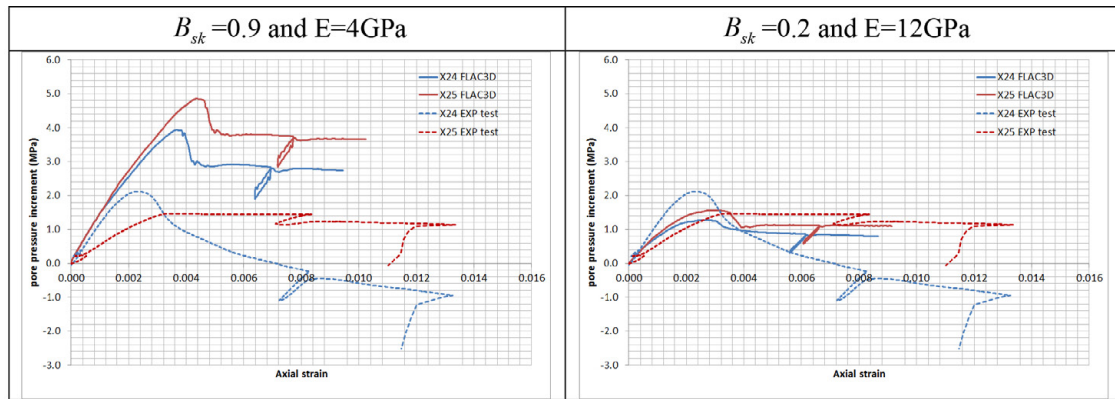


Fig. 5-30: Pore pressure increments comparison between FLAC3D and laboratory experiments for X samples.

Left: soft parameter set. Right: stiff parameter set.

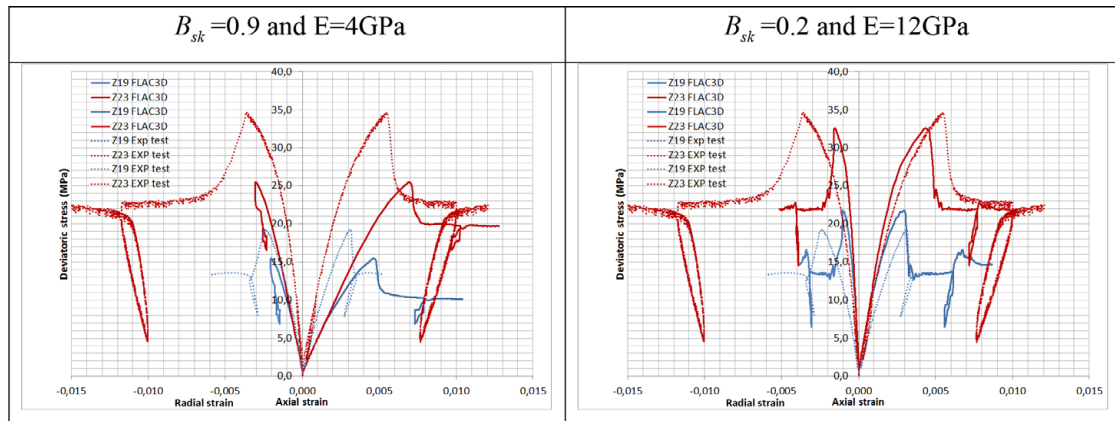


Fig. 5-31: Comparison of stress-strain evolution between FLAC3D and laboratory experiments for Z samples.

Left: soft parameter set. Right: stiff parameter set.

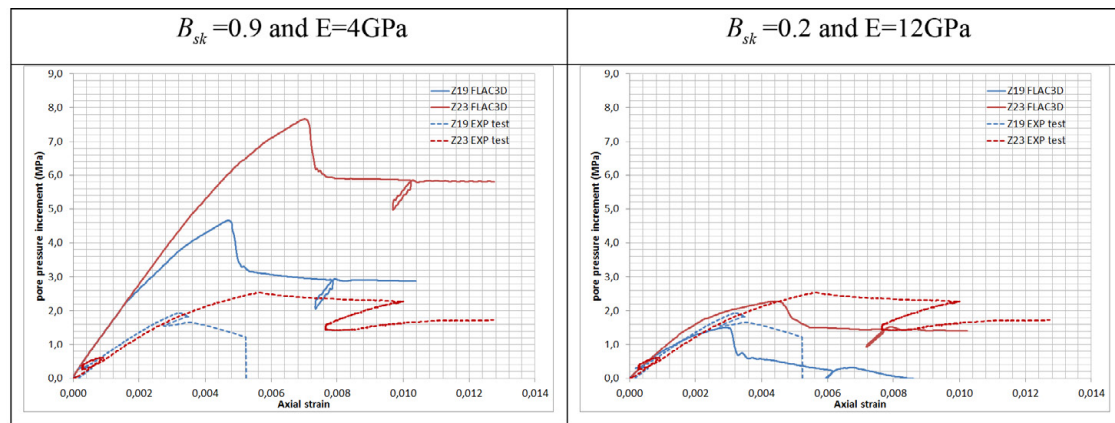


Fig. 5-32: Pore pressure increments comparison between FLAC3D and laboratory experiments for Z samples.

Left: soft parameter set. Right: stiff parameter set.

### 5.3 Shear band formation

Results in terms of shear band formation are compared between numerical samples (FLAC3D model) and experimental samples. Snapshots (captured at the end of the test) of different samples are given from Figs. 5-33 to 5-36. The contours of plastic shear strains are given for the figures showing numerical results. In order to better visualize the numerical shear band, the contour of maximum plastic shear strain is limited to 0.02 for all figures. The orientation of bedding planes is depicted by white lines in these figures. For figures of experimental samples, the observable shear bands are indicated by a red arrow.

Laboratory experiments and numerical simulations show different shear band formation behavior. For P samples, the laboratory experiments shows diagonal shear bands which go through the entire sample. For numerical samples, they are mostly formed near the top and the bottom surface (*i.e.*, with a shorter shear band length).

For S samples, inclined shear bands with a shorter length are observed for laboratory experiments. Besides these, "brittle-like cracks" are also observed along the horizontal planes (*i.e.*, bedding plane). The "S numerical" shows a form of shear band similar to the one observed for "P numerical".

For X and Z samples, the experimental shear bands are formed along the weakness plane (bedding). However, "dominant" shear bands are mostly formed along the direction perpendicular to the weakness plane, for numerical samples. It has been shown in work done by Cundall and Fairhurst (1986) that two possibilities of shear band formation coexist for materials subjected to loading oblique to their bedding plane. As shown in Fig. 5-37, the shear band may slide along the bedding or it may slide perpendicular to it (called "kink band"). However, it seems that FLAC3D produces systematically "kink bands" for X and Z samples. In order to better understand the mechanical behavior of the shear band formation, additional tests are carried out. Their results are presented in the following sections.

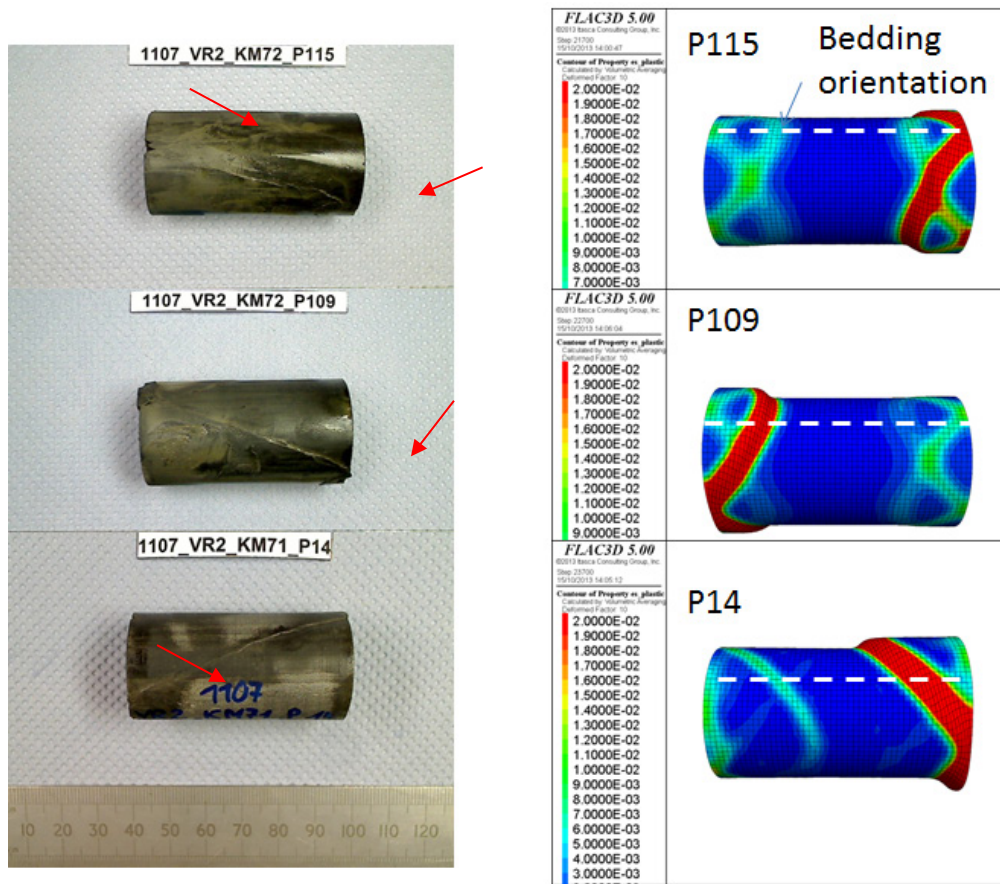


Fig. 5-33: Shear bands formation for P samples.

*Left:* samples after experimental deformation (from Jahns 2013). *Right:* numerical results.

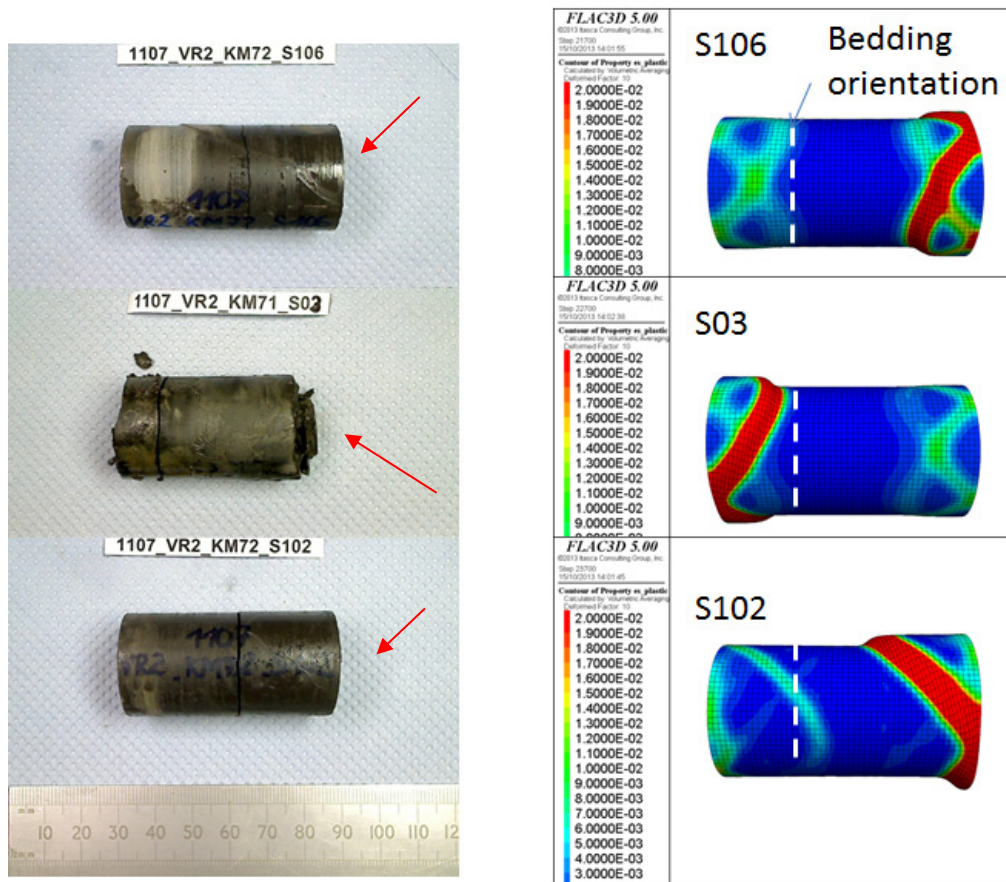


Fig. 5-34: Shear bands formation for S samples.

*Left:* samples after experimental deformation (from Jahns 2013). *Right:* numerical results.

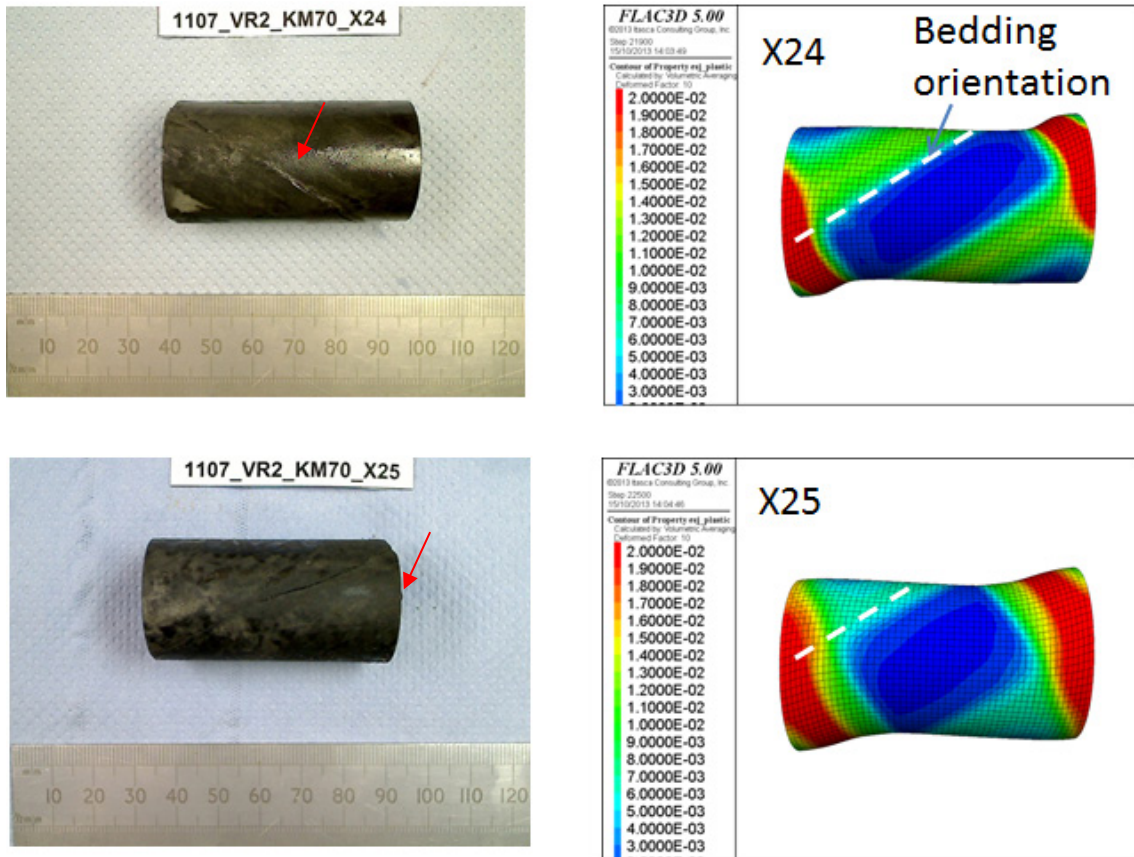


Fig. 5-35: Shear bands formation for X samples.  
*Left:* samples after experimental deformation (from Jahns 2013). *Right:* numerical results.

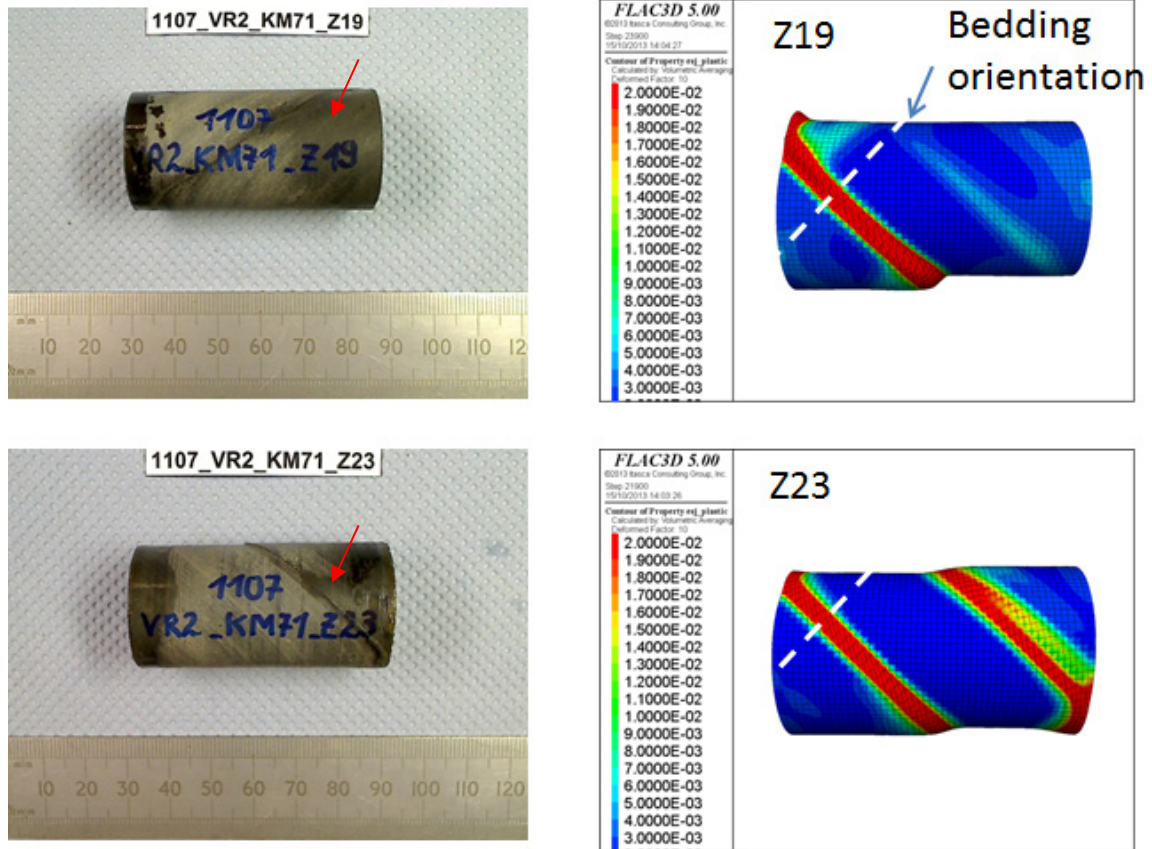


Fig. 5-36: Shear bands formation for Z samples.

*Left:* samples after experimental deformation (from Jahns 2013). *Right:* numerical results.

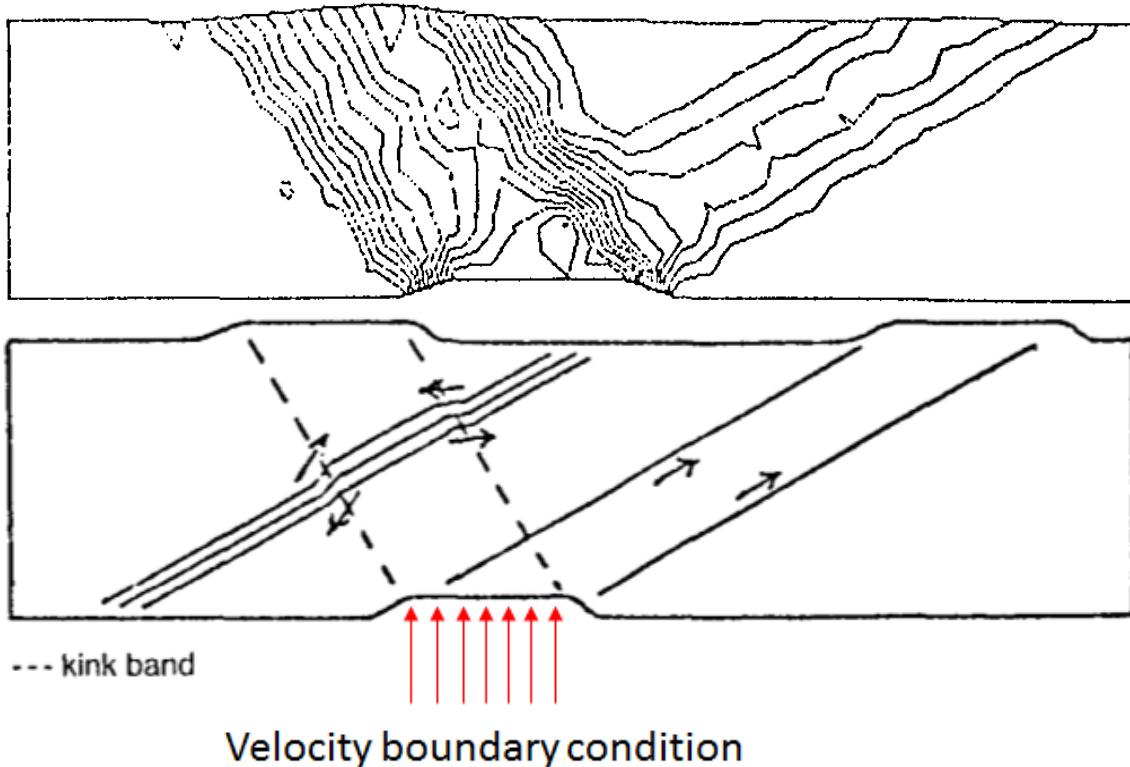


Fig. 5-37: Example of kink band formation orthogonal to the main slip direction.

Above: contours of vertical displacement, indicating two distinct sets of shear bands orthogonal to each other. Below: slip directions (arrows) and kinking (dashed lines). From Cundall & Fairhurst (1986).

#### 5.4 Boundary condition effect

As shown in Figure 3-4, roller boundary conditions are used (top and bottom surface) for all the simulations presented previously. Additional simulations are carried out where fixed boundary conditions are used: horizontal displacements are fixed to zero for grid points located at the top and the bottom surface.

Runs are carried out for P and X samples with  $B_{sk}$  fixed to 0.7. The results are reported from Figs. 5-38 to 5-47. Lower strength and lower pore pressure are observed when using "fixed" boundary conditions. In fact, the Poisson effect is prevented at "fixed" grid points. Thus, the zones located next to top and bottom surface undergo higher stresses (Fig. 5-39) and higher pore pressure increments (Fig. 5-41). Due to the boundary condition effect, the computed  $B_{sk}$  is different (Fig. 5-42). It seems that the increase in pore pressure is more pronounced than the increase in stress for cases using fixed boundary. Thus, the model tends to show higher  $B_{sk}$  for cases using fixed boundary. Finally the shear band formation is presented in Fig. 5-43. For samples using fixed boundary, the shear band can only propagate from the edge of the top and bottom surfaces, since plastic shear strain can hardly be developed at zones containing fixed grid points.

Results for X samples indicate similar behavior as observed for P samples. Higher stress and higher pore pressures are obtained when using fixed boundary. Also, the computed  $B_{sk}$  tends to

be larger for these cases. Plastic shear strains are illustrated in Fig. 5-47. Clearly, the dominant shear band is along the weakness plane when a fixed boundary is applied. Kink bands are also developed along the direction perpendicular to bedding with a smaller plastic shear strain.

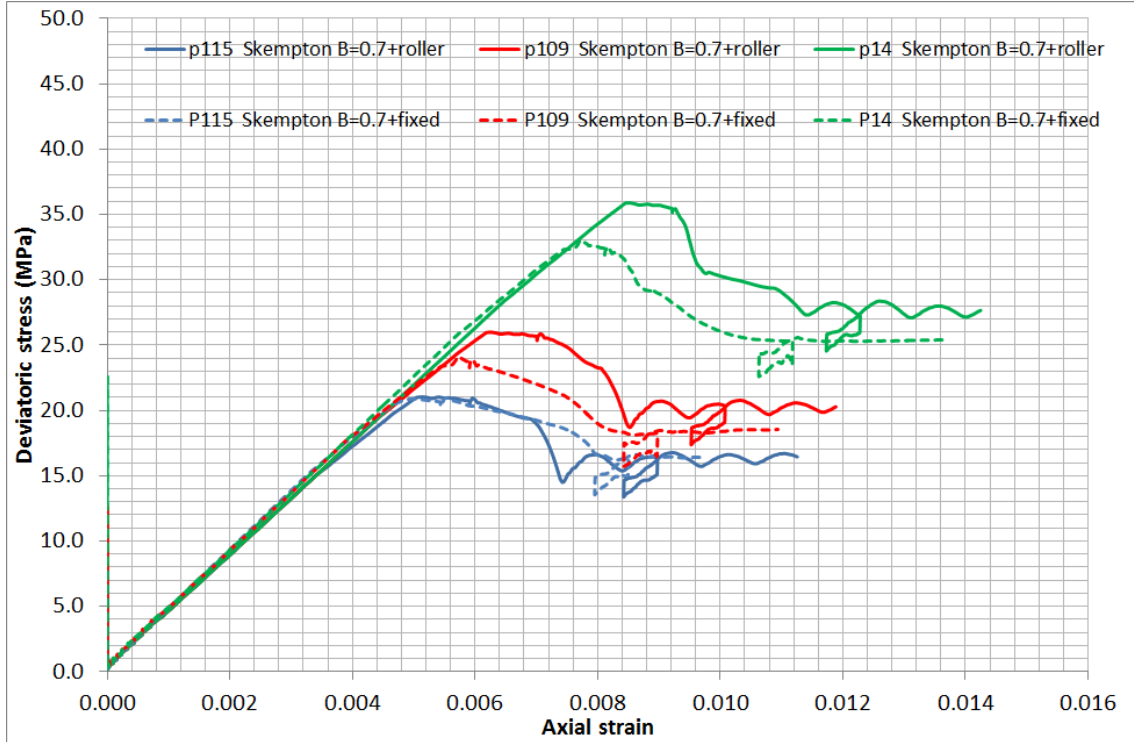


Fig. 5-38: Stress –strain curve for P samples using roller and fixed boundary (P samples).

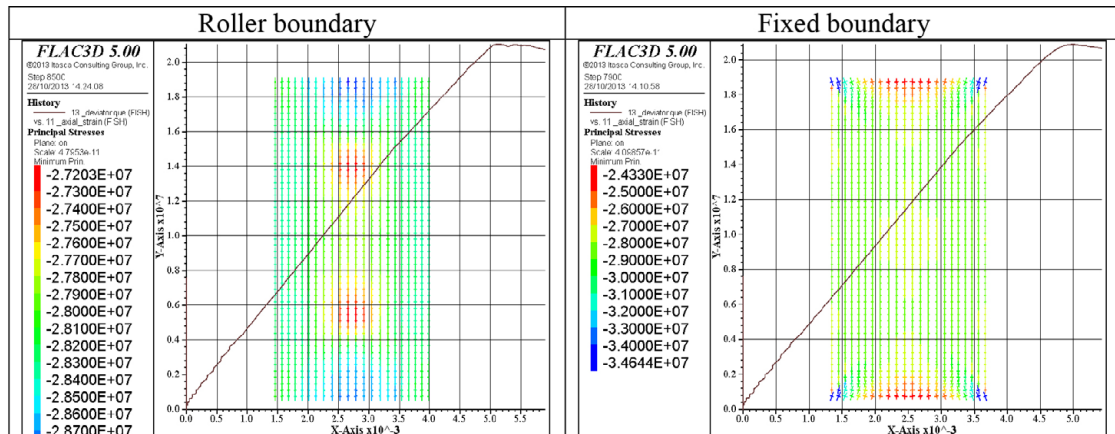


Fig. 5-39: Minor principal stress tensor (compression) just after reaching peak strength (P115).

The black line indicates stress-strain evolution from the zero point to peak, indicating that peak strength is not affected by the boundary condition.

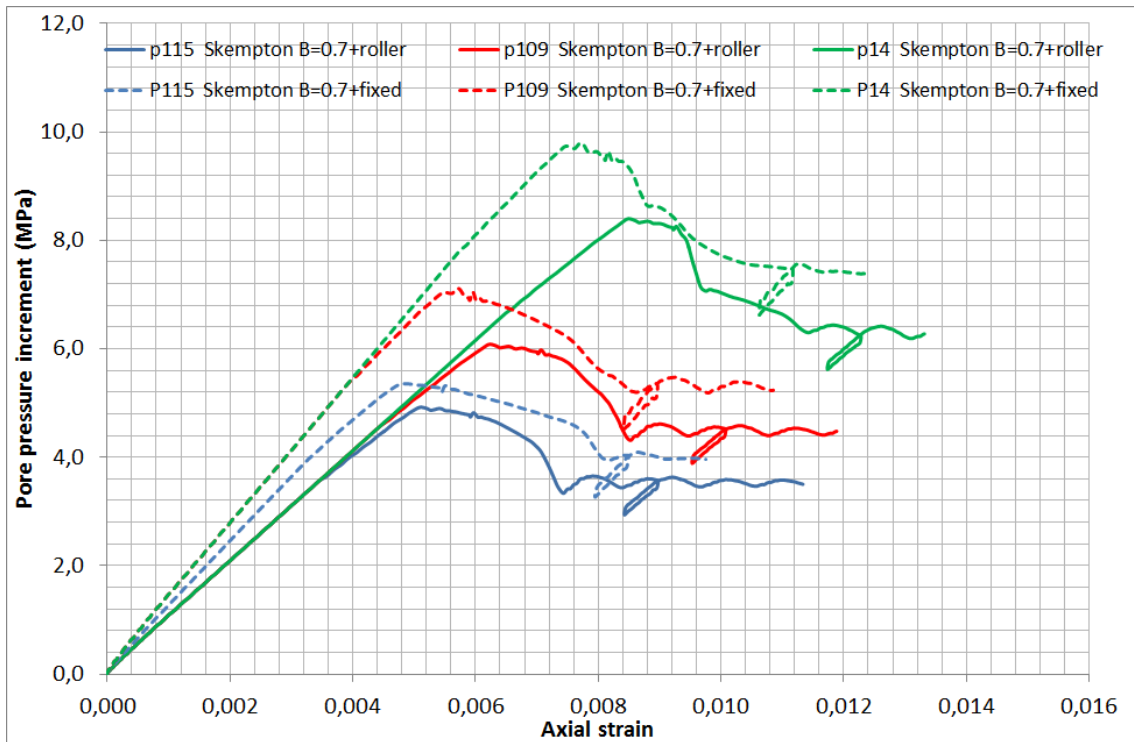


Fig. 5-40: Pore pressure increment for samples using roller and fixed boundary (P samples).

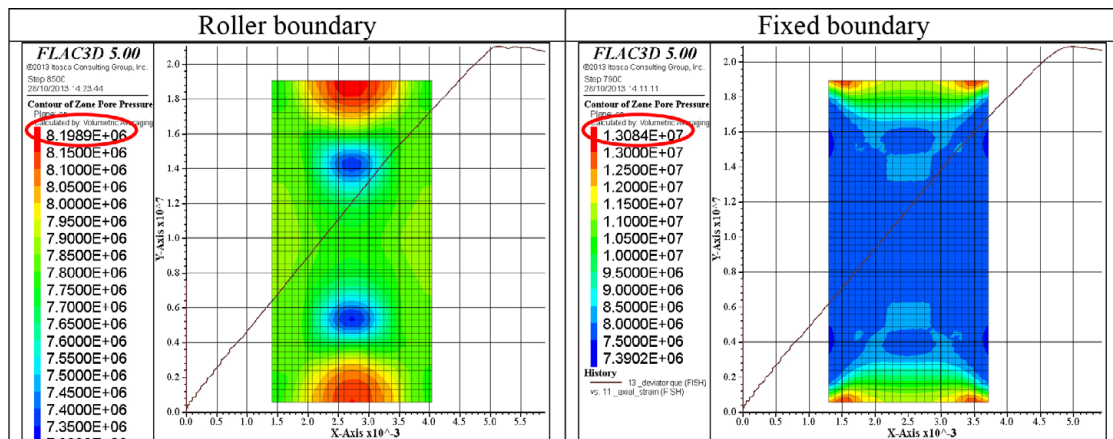


Fig. 5-41: Pore pressure just after reaching peak strength (P115).

The black line indicates stress-strain evolution from the zero point to peak, indicating that peak strength is not affected by the boundary condition. Note the different values in the color coding between the two figures as indicated by the dashed red line.

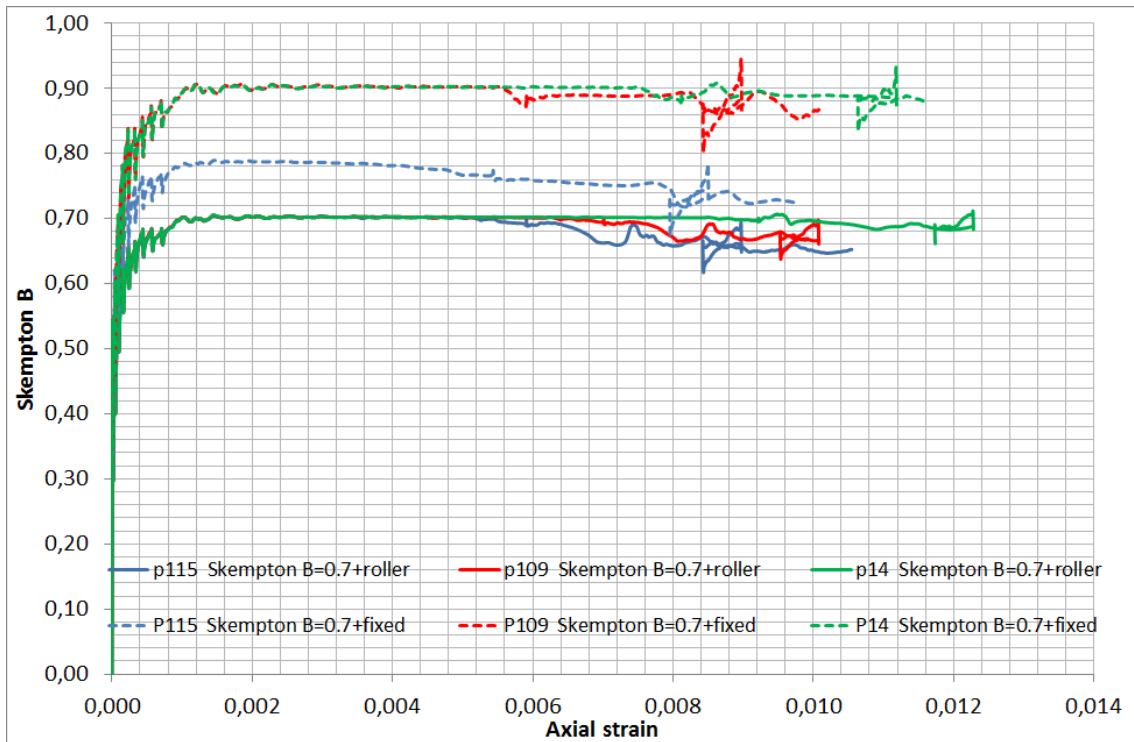


Fig. 5-42:  $B_{sk}$  for samples using roller and fixed boundary (P samples).

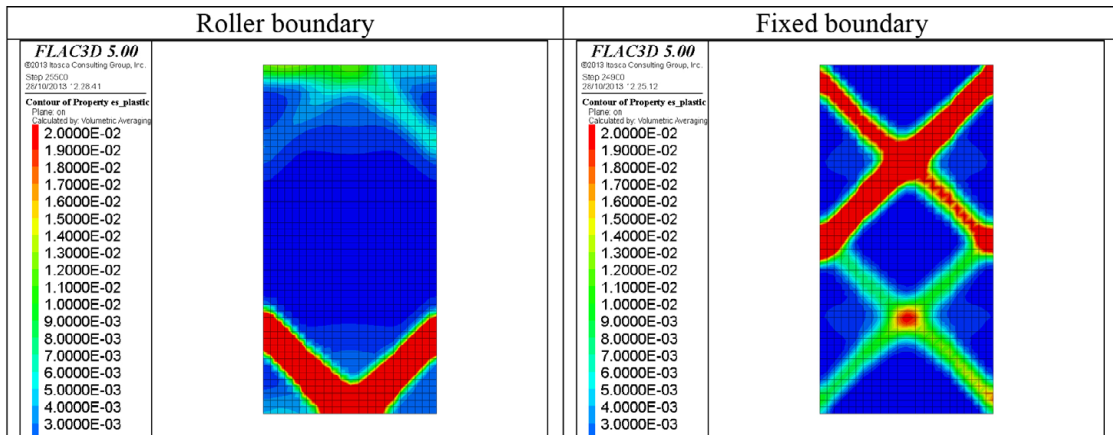


Fig. 5-43: Comparison of plastic shear strain with roller and fixed boundary. Shown are calculated strains for sample P115 at the end of the test.

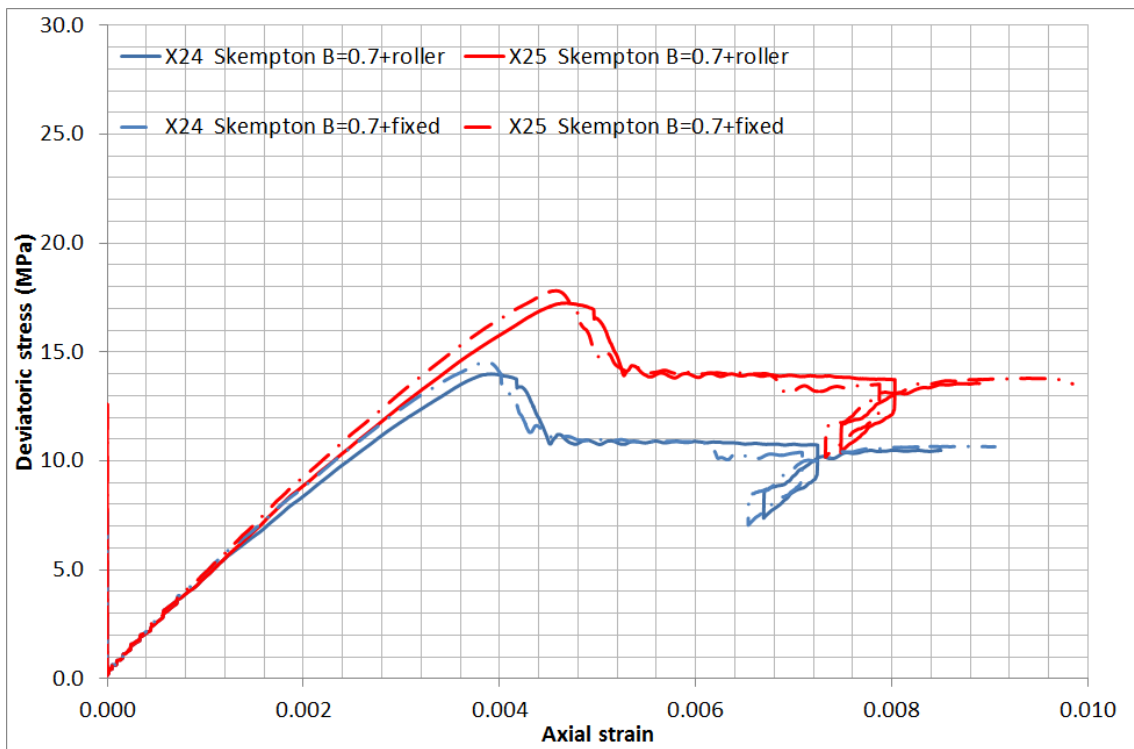


Fig. 5-44: Stress –strain curve for samples using roller and fixed boundary (X samples).

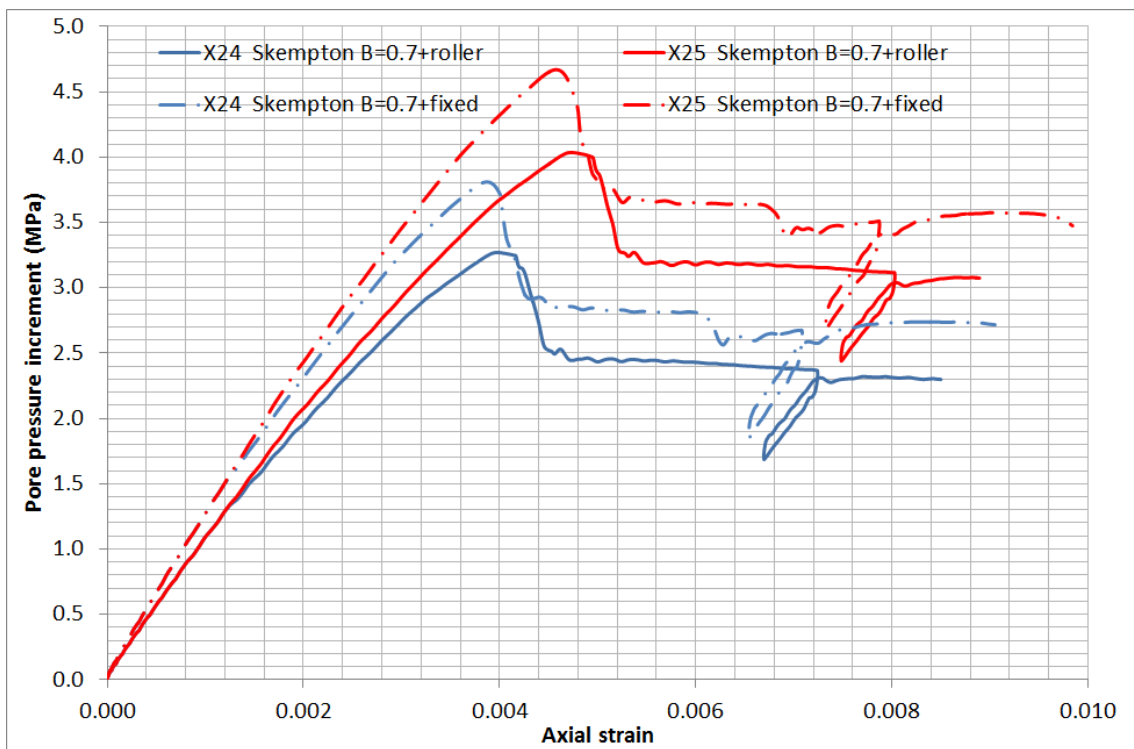


Fig. 5-45: Pore pressure increment for samples using roller and fixed boundary (X samples).

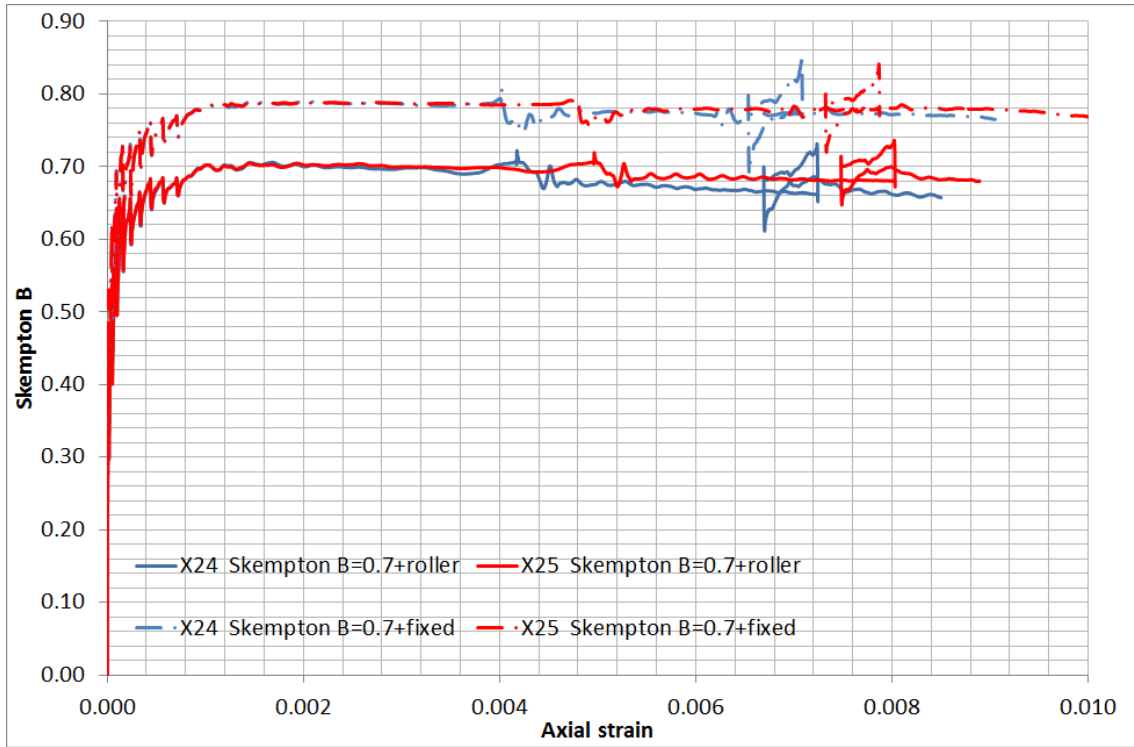


Fig. 5-46: Comparison of  $B_{sk}$  for samples using roller and fixed boundary (X samples).

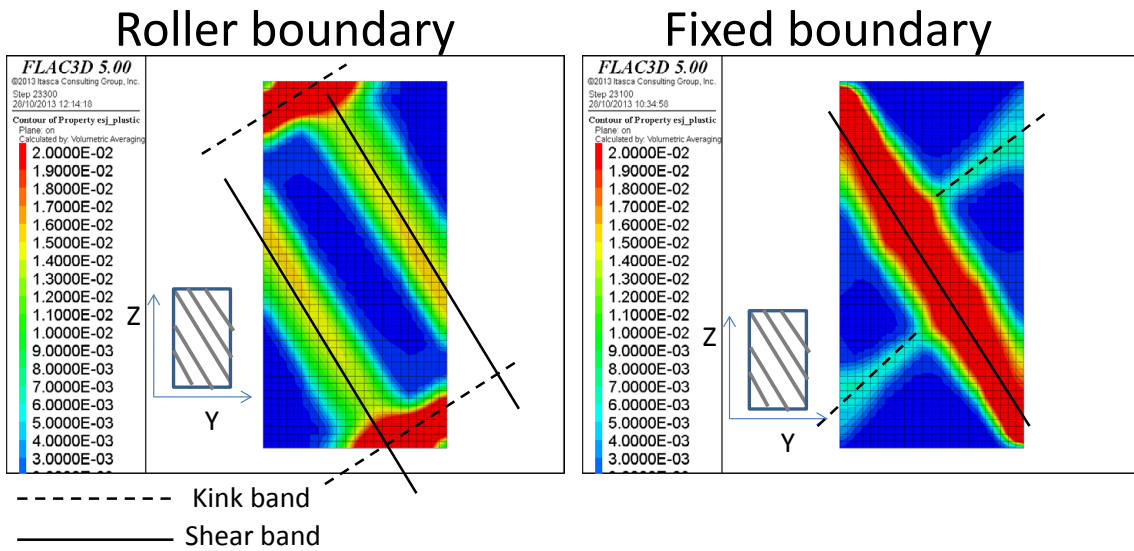


Fig. 5-47: Plastic shear strain at the end of the test (X24).

## 5.5 Angle between loading and bedding orientation

In the presented work, the simulations are carried out on P ( $\beta = 0^\circ$ ), S ( $\beta = 90^\circ$ ), X ( $\beta = 30^\circ$ ) and Z ( $\beta = 45^\circ$ ) samples. Beta is defined as the angle between the loading direction and the bedding orientation. Theoretically, the model should predict sliding on ubiquitous joints if  $\beta > \phi$  (with  $\phi$ , the joint friction angle). In order to better understand the mechanism for shear band formation while changing beta, a series of simple compression tests are conducted using FLAC 2D. Roller boundary conditions are used for these tests. The joint friction angle is set at  $30^\circ$ , with an elastic matrix. This implies that sliding along the bedding is forced.

Beta varies from  $25^\circ$  to  $50^\circ$  with a of  $5^\circ$  increment. Results in terms of maximum shear increment and of displacement vectors are presented in Fig. 5-48. For each figure, red lines indicate the bedding plane, solid black lines indicate shear bands along the bedding and dotted black lines indicate kink bands perpendicular to bedding. Clearly, the dominant sliding orientation changes when beta varies. For large betas, sliding patterns are mostly observed along the bedding (shear band). Kink bands appear as well in the direction perpendicular to bedding for small shear strains. The dominant sliding orientation tends to change when decreasing beta. For  $\beta = 30^\circ$  and  $\beta = 25^\circ$ , the dominant sliding occurs in the direction perpendicular to bedding.

The Z and X simulations described in this report all fall in the "small beta" range: Z samples correspond to  $\beta = 45^\circ$  and X samples to  $\beta = 30^\circ$ . Thus, dominant sliding is perpendicular to bedding. The results of FLAC3D models are compatible with those obtained from FLAC. Finally, a simulation using a larger beta is carried out in three dimensions using FLAC3D ( $\beta = 55^\circ$ ). As illustrated in Fig. 5-49, the dominant sliding occurs along the bedding for this case.

A summary of localization orientations produced by the ubiquitous joint model is shown in Fig. 5-50. These results are obtained from numerical simulations of simple compression tests (for the 2D models) and of triaxial tests (for the 3D models). Thus, the summary presented in Fig. 5-50 is valid for numerical simulations with the same predefined configurations (roller boundaries, sample size ratio height/width of 2, plane strain condition for 2D model, etc.).

Numerical reproduction of shear band formation is a difficult task. Any minor perturbation of the system may induce a change in the orientation of shear band propagation (sample geometry, velocity of loading frame, boundary condition, etc.). In FLAC and FLAC3D, the weakness of the bedding is represented by "ubiquitous-joints". However, only the strength anisotropy is accounted for in this constitutive model. The elastic anisotropy is omitted. Thus, the numerical ubiquitous-joint model can be seen as a representation of a rock matrix containing an infinite number of bedding planes, with zero spacing. However, real bedding planes do have a finite thickness, with a non-zero bending resistance and anisotropic stiffnesses. For such "discontinuous" bedding systems, kink band formation is more difficult.

In its current state, the SUBI model reproduces shear band sliding correctly and develops kink band sliding too easily. It is therefore pessimistic. Development of an advanced ubiquitous-joint model accounting for such features is ongoing. This will allow a better reproduction of the shear behavior for materials with bedding.

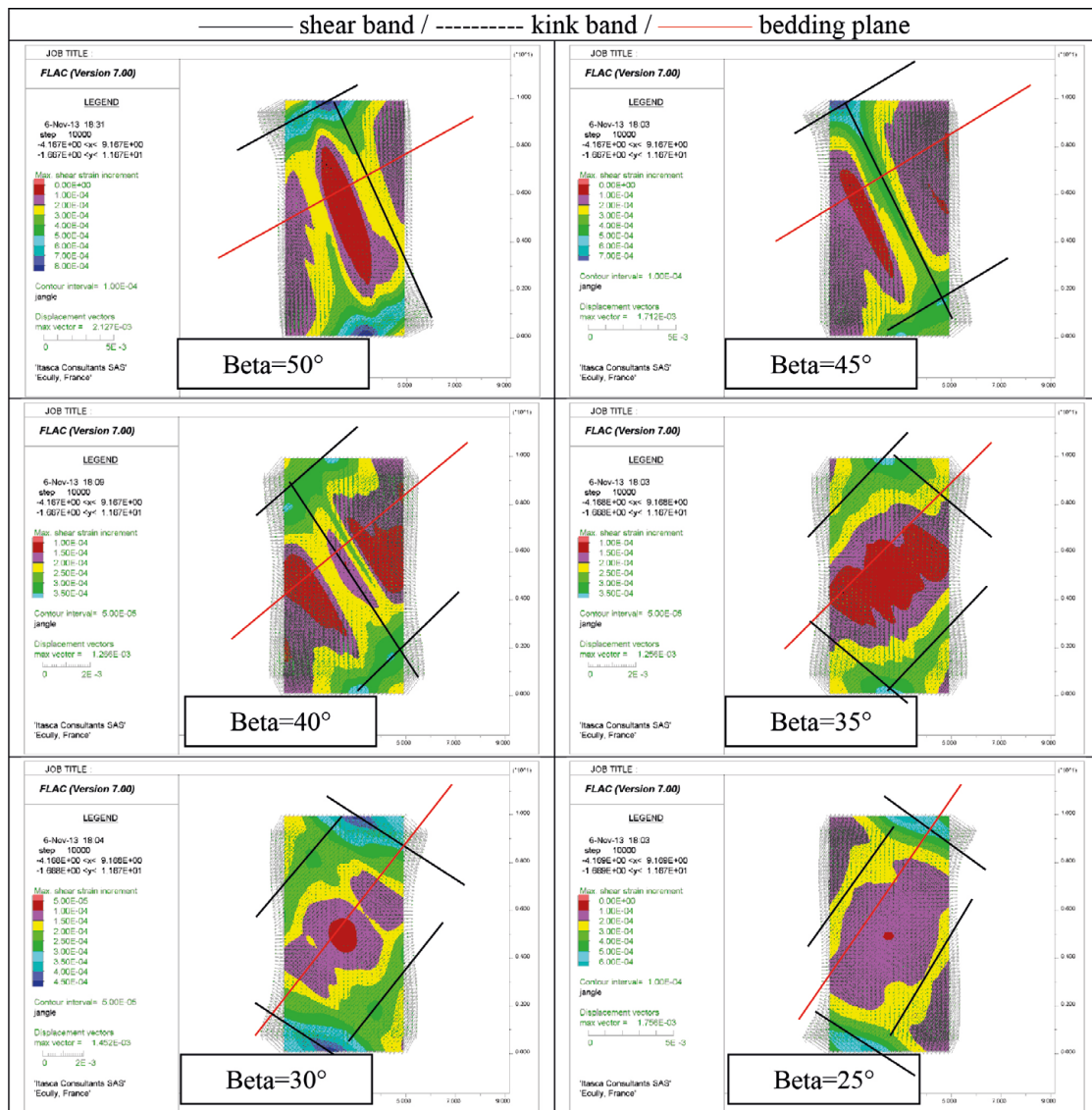


Fig. 5-48: Maximum shear strain and displacement vector for samples using different bedding orientation.

Simulations performed on FLAC 2D, with friction angle of bedding of 30°.

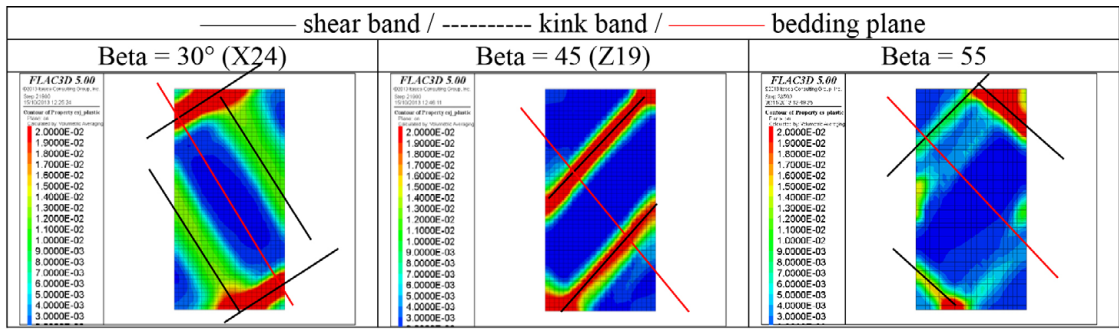


Fig. 5-49: Plastic shear strain for samples using different bedding orientation. Simulations performed on FLAC 3D, with friction angle of bedding of 30°.

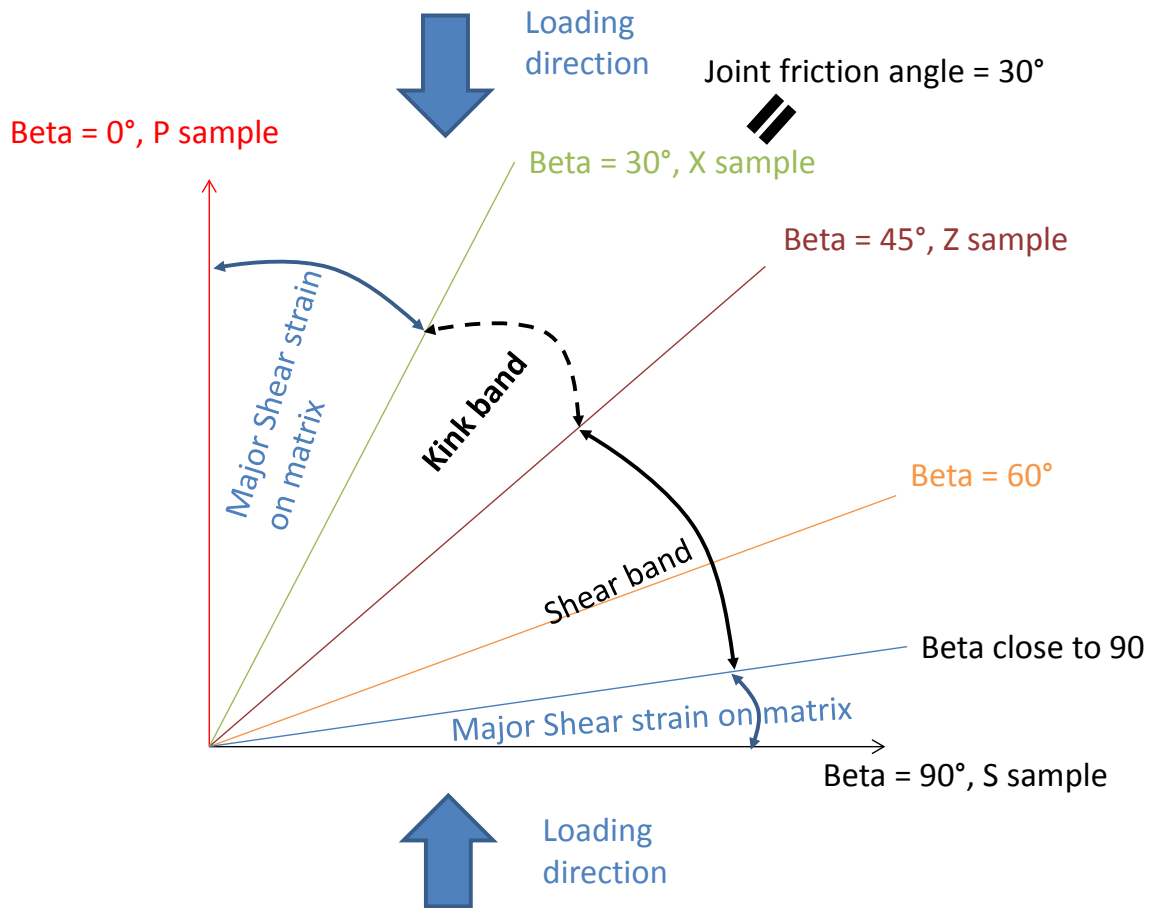


Fig. 5-50: Schematic of localization using subequivalent joint model.

## 6 Conclusions

The objective of this study is to conduct a consistency check on the constitutive law used to characterize the elasto-plastic behaviour of Opalinus Clay by numerically reproducing undrained triaxial laboratory tests using FLAC3D software. The constitutive law used for the numerical modelling is the bilinear strain hardening-softening ubiquitous-joint model (SUBI). The numerical sample is generated to fit the geometry of the laboratory experiments (cylindrical shape). Triaxial loading is conducted in a way similar to the laboratory experiments. The pore pressure is set at 40% of the confinement pressure and increasing axial strains are applied until failure. Also, hysteretic cycles are conducted during post-peak. Material properties are assigned to matrix and bedding (cohesion and friction angle) based on data provided by Nagra (Table 2-2). A hardening-softening behaviour is simulated by varying the cohesion (and the friction angle) as a function of plastic shear strain.

The study first focussed on calibration of the critical strain for the softening behavior (Task 1) and the hardening behavior (Task 2), respectively. The effect of a variation in the dilation angle and values of the hydromechanical coupling parameters (Biot coefficient  $\alpha$  and Skempton coefficient  $B_{sk}$ ) were also examined (as part of Task 2)

It is noted that the tensile strength is not calibrated in the present work. According to the value reported in Tab. 2-2, it is set to 2 MPa for both bedding and matrix. The numerical model is used to reproduce triaxial tests with a rather high confinement pressure (from 7.6 MPa to 22.6 MPa). Thus, stresses in the sample stay in compression region during the simulation. As a consequence, the tensile failure will never be triggered. Additional experimental/numerical work is needed to calibrate the tensile strength, using other stress paths (typically, UCS test or direct tension test).

The numerical results were compared with the laboratory experiments. In general, the numerical results fit well the experimental data, though they cannot fit the results for P and S samples using the same parameter set. This limitation arises from the fact that the SUBI model used accounts only for strength anisotropy but uses isotropic elasticity. The parameters of the best calibration are reported in Table 4-3 and Table 4-4 for Subiquitous-joint material properties and in Tables 5-1 and 5-2 for poroelastic properties.

Special attention has been paid in this work in order to better understand shear band formation using the Subiquitous – joint model. As shown in Section 5.5, the numerical model predicts mostly sliding perpendicular to bedding if the angle between the loading direction and the bedding orientation is smaller than (or close to)  $45^\circ$ , which is the case for both Z samples –  $\beta = 45^\circ$ , and X samples –  $\beta = 30^\circ$ . However, laboratory experiments systematically show shear bands along the bedding (for both Z and X samples). Numerical development is ongoing in which the subiquitous-joint model will account for the effective stiffness between bedding and matrix. This advanced model should be able to better reproduce the shear behaviour of materials with bedding plane.



## 7 References

- Albert W., Madritsch H., Vogt T., Weber H.-P., Bläsi H. (2012): Geologie, Stratigraphie, Strukturgeologie und bohrlochgeophysikalisches Logging der Geothermiebohrung Schlattingen SLA-1 (Rohdaten). Nagra Project Report NPB 12-16. Nagra, Wettingen.
- Cundall P.A. & Fairhurst C. (1986): Correlation of discontinuum models with physical observations – an approach to the estimation of rock mass behaviour. Felsbau Fachzeitschrift für Geomechanik und Ingenieurgeologie im Bauwesen und Bergbau. Jg. 4, Nr. 4.
- Ferrari A., Favero V., Manca D. & Laloui L. (2012): Geotechnical characterization of core samples from the geothermal well Schlattingen LSA-1. Nagra Arbeitsbericht NAB 12-50. Nagra, Wettingen.
- Itasca Consulting Group Inc. (2012): FLAC3D (Fast Lagrangian Analysis of Continua in 3 Dimensions), Version 5. 0. Minneapolis: ICG.
- Jahns Gesteinslabor (2013): Geomechanical laboratory tests on Opalinus Clay cores from the bore hole Schlattingen SLA-1. Nagra Arbeitsbericht NAB 13-18. Nagra, Wettingen.
- Nagra (2001): Sondierbohrung Benken – Untersuchungsbericht. Textband und Beilagenband. Nagra Tech. Bericht NTB 00-01. Nagra, Wettingen.
- Nagra (2002): Projekt Opalinuston: Synthese der geowissenschaftlichen Untersuchungsergebnisse – Entsorgungsnachweis für abgebrannte Brennelemente, verglaste hochaktive sowie langlebige mittelaktive Abfälle. Nagra Tech. Bericht NTB 02-03. Nagra, Wettingen.
- TeKamp L. (2008): Comparative rock-mechanical modeling of ILW caverns in different host rocks. Nagra Arbeitsbericht NAB 08-45. Nagra, Wettingen.



## Appendix A: Bilinear, strain-(hardening-)softening ubiquitous joint model

The bilinear strain-hardening/softening ubiquitous-joint model is a generalization of the ubiquitous-joint model. In the bilinear model, the failure envelopes for the matrix and joint (bedding) are the composite of two Mohr-Coulomb criteria with a tension cutoff that can harden or soften according to specified laws.

The softening behaviour of the matrix and the joint are specified in tables in terms of four independent hardening parameters (two for the matrix and two for the joint) that measure the amount of plastic shear and tensile strain, respectively. In this numerical model, general failure is first detected for the step, and relevant plastic corrections are applied. The new stresses are then analyzed for failure on the weak plane, and updated accordingly. The hardening parameters are incremented if plastic flow has taken place, and the parameters of cohesion, friction, dilation and tensile strength are adjusted for the matrix and the joint using the tables.

The criterion for failure in the matrix used in this model is sketched in the principal stress plane  $(\sigma_1, \sigma_3)$  in Figure A-1. The failure envelope is defined by two Mohr-Coulomb failure criteria:  $f_2^s = 0$  and  $f_1^s = 0$  for segments A-B and B-C, and a tension failure  $f^t = 0$  for segment C-D. The shear failure criterion has the general form  $f^s = 0$ . The criterion is characterized by a cohesion,  $c_2$  and a friction angle  $\phi_2$  for segment A-B, and by a cohesion  $c_1$  and friction angle  $\phi_1$  for segment B-C. The tensile failure criterion is specified by means of the tensile strength,  $\sigma^t$ . Thus, we have:

$$f^s = \sigma_1 - \sigma_3 N_\phi + 2c\sqrt{N_\phi}$$

$$f^t = \sigma_3 - \sigma^t$$

Where

$$N_\phi = \frac{1 + \sin(\phi)}{1 - \sin(\phi)}$$

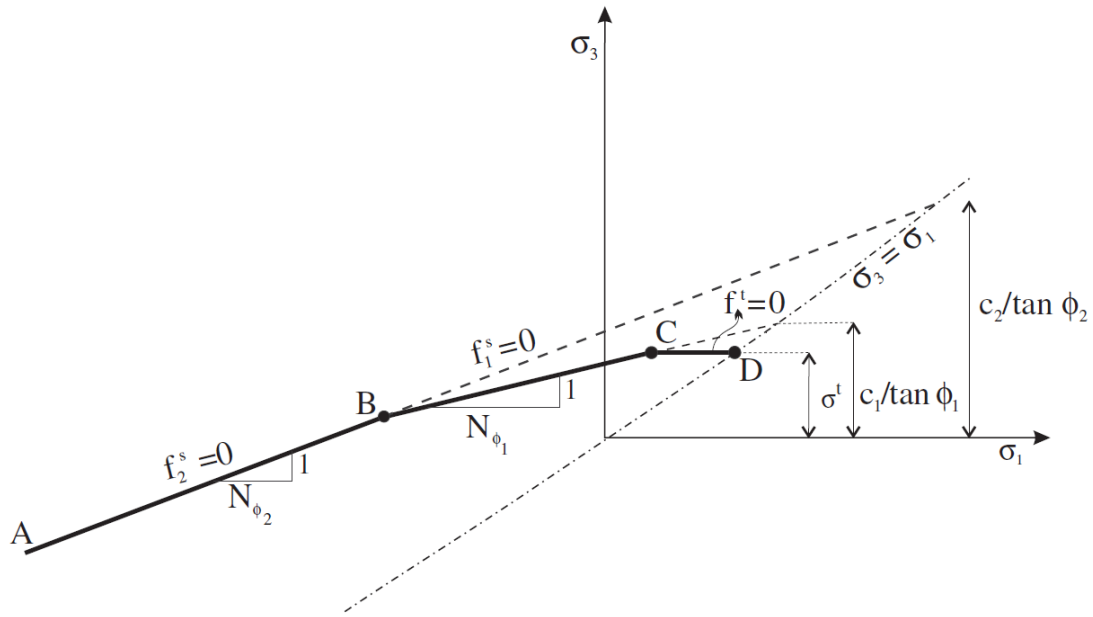


Fig. A1: Failure criterion in principal stress plane (Matrix).

The failure criterion for the weak plane is expressed in terms of the magnitude of the tangential component,  $\tau = \sqrt{\sigma_1'3'^2 + \sigma_2'3'^2}$ , and the normal traction component,  $\sigma_3'3'$ , on the weak plane. The failure criterion is represented in Figure A-2 and corresponds to two Mohr-Coulomb failure criteria ( $f_2^s = 0$  for segment A-B, and  $f_1^s = 0$  for segment B-C) and a tension failure criterion ( $f^t = 0$  for segment C-D). Each shear criterion has the general form  $f^s = 0$ , and is characterized by a cohesion and a friction angle ( $c_{j2}, \phi_{j2}$  for segment A-B, and  $c_{j1}, \phi_{j1}$  for segment B-C). The tension criterion is specified by means of the tensile strength,  $\sigma_j^t$ . Thus, we have:

$$f^s = \tau + \sigma_3'3' \tan \phi_j - c_j$$

$$f^t = \sigma_3'3' - \sigma_j^t$$

The previous description about the bilinear strain-hardening/softening ubiquitous-joint model can be found at [1].

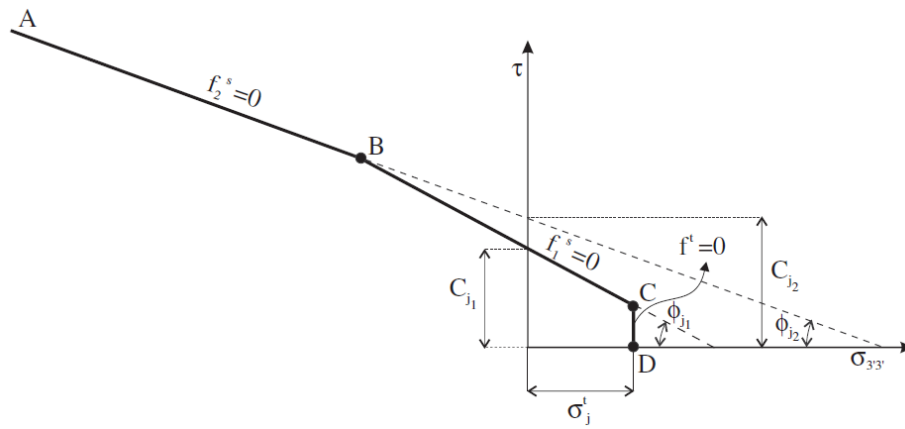


Fig. A2: Failure criterion in component parallel ( $\tau$ ) and perpendicular ( $\sigma_{33}$ ) to the weak plane (Bedding).



## Appendix B: Strain dependency to the mesh discretization

The numerical simulation of rock damage depends on the mesh refinement employed to model the rock. For example, Figure B-1 shows the shear band thickness obtained with two meshes, one being twice finer than the other. When localization appears and a shear band develops, the shear displacement at which peak (and then residual) properties are reached should be constant and independent from the zone size. However, for a given displacement ( $\Delta L$ ) along the shear band, the recorded strain in the finer mesh is twice larger. Therefore, if the plastic shear strain is used as the evolution parameter, the input strain ( $\gamma_{ref}^{peak}$ ) must be adjusted for each zone according to its edge length. A simple regularization technique can be selected to address this issue using the following equation:

$$\gamma_l^{peak} = \gamma_{ref}^{peak} \cdot \left(\frac{L}{l}\right)$$

With  $l$  the size of the zone in which  $\gamma_l^{peak}$  is calculated, and  $L$  the reference zone size used for calibrating model properties, among which  $\gamma_{ref}^{peak}$ . This procedure improves the damage propagation in the rock mass and makes it less dependent on the model mesh around the excavation.

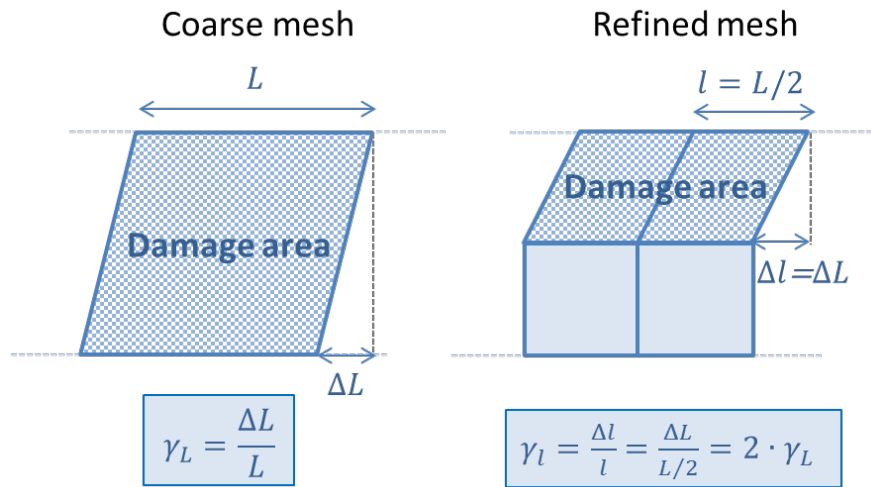


Fig. B1: Strain dependency to the mesh discretization.



Appendix C  
 Parameter set used for the different  
 modelling runs

Sign convention used in the table: m=matrix; j=bedding; c=(Mohr-Coulomb-)cohesion; f=internal friction angle; Indices 1 and 2 refer to first and second segment of bilinear law

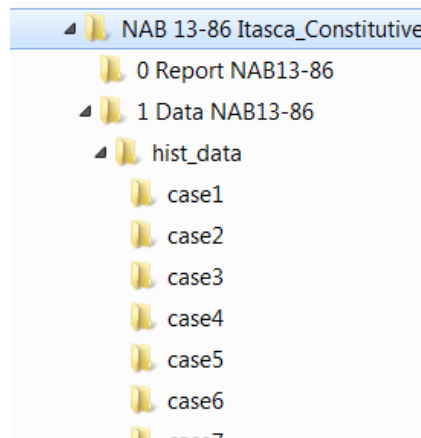
n°	description	Critical strain for matrix cohesion		Critical strain for bedding cohesion		Critical strain for matrix friction angle		Critical strain for bedding friction angle		Plastic tensile strain for matrix and bedding		Dilation angle		Biot coefficient $\alpha$	Biot Modulus M	Skempton B	Drained Young's Modulus E	Boundary conditions	Strain-softening	Strain-hardening
		mc1	mc2	jc1	jc2	mf1	mf2	jf1	jf2	mt	jt	j	m							
101		1.20E-02	6.00E-03	6.00E-03	6.00E-03	1.20E-02	6.00E-03	6.00E-03	6.00E-03	1.20E-02	1.20E-02	-	-	0.8	3.39E+09	0.25	1.20E+10	Roller	o	x
102		2.00E-02	6.00E-03	6.00E-03	6.00E-03	2.00E-02	6.00E-03	6.00E-03	6.00E-03	1.20E-02	1.20E-02	-	-	0.8	3.39E+09	0.25	1.20E+10	Roller	o	x
103	Ref. case	2.00E-02	6.00E-03	3.00E-03	3.00E-03	2.00E-02	6.00E-03	3.00E-03	3.00E-03	1.20E-02	1.20E-02	-	-	0.8	3.39E+09	0.25	1.20E+10	Roller	o	x
104	mc1,mf1	6.00E-02	6.00E-03	3.00E-03	3.00E-03	6.00E-02	6.00E-03	3.00E-03	3.00E-03	1.20E-02	1.20E-02	-	-	0.8	3.39E+09	0.25	1.20E+10	Roller	o	x
105	mc2,mf2	2.00E-02	1.80E-02	3.00E-03	3.00E-03	2.00E-02	1.80E-02	3.00E-03	3.00E-03	1.20E-02	1.20E-02	-	-	0.8	3.39E+09	0.25	1.20E+10	Roller	o	x
106	jc1,jf1	2.00E-02	6.00E-03	9.00E-03	3.00E-03	2.00E-02	6.00E-03	9.00E-03	3.00E-03	1.20E-02	1.20E-02	-	-	0.8	3.39E+09	0.25	1.20E+10	Roller	o	x
107	jc2,jf2	2.00E-02	6.00E-03	3.00E-03	9.00E-03	2.00E-02	6.00E-03	3.00E-03	9.00E-03	1.20E-02	1.20E-02	-	-	0.8	3.39E+09	0.25	1.20E+10	Roller	o	x
108	dila = 3	2.00E-02	6.00E-03	3.00E-03	3.00E-03	2.00E-02	6.00E-03	3.00E-03	3.00E-03	1.20E-02	1.20E-02	3.00	3.00	0.8	3.39E+09	0.25	1.20E+10	Roller	o	x
109	hardening	2.00E-02	6.00E-03	3.00E-03	3.00E-03	2.00E-02	6.00E-03	3.00E-03	3.00E-03	1.20E-02	1.20E-02	-	-	0.8	3.39E+09	0.25	1.20E+10	Roller	o	o
		2.50E-04	2.00E-04	3.00E-04	3.00E-04	2.50E-04	2.00E-04	3.00E-04	3.00E-04	-	-	-	-	-	-	0.25	-	-	-	-
110	Biot	2.00E-02	6.00E-03	3.00E-03	3.00E-03	2.00E-02	6.00E-03	3.00E-03	3.00E-03	1.20E-02	1.20E-02	-	-	0.9	2.68E+09	0.25	1.20E+10	Roller	o	o
111	Biot	2.00E-02	6.00E-03	3.00E-03	3.00E-03	2.00E-02	6.00E-03	3.00E-03	3.00E-03	1.20E-02	1.20E-02	-	-	1.00	2.98E+09	0.25	1.20E+10	Roller	o	o
112	Md1=2,md2=0,2	1.50E-02	5.00E-03	3.00E-03	3.00E-03	1.50E-02	5.00E-03	3.00E-03	3.00E-03	1.20E-02	1.20E-02	-	2/0,2	0.8	3.39E+09	0.25	1.20E+10	Roller	o	o
113	Biot=0,9	2.00E-02	6.00E-03	3.00E-03	3.00E-03	2.00E-02	6.00E-03	3.00E-03	3.00E-03	1.20E-02	1.20E-02	-	-	0.9	3.16E+09	0.25	1.20E+10	Roller	o	o
114	Biot=1,0	2.00E-02	6.00E-03	3.00E-03	3.00E-03	2.00E-02	6.00E-03	3.00E-03	3.00E-03	1.20E-02	1.20E-02	-	-	1.00	2.98E+09	0.25	1.20E+10	Roller	o	o
115	biotC=0.8_B=0.25	2.00E-02	6.00E-03	3.00E-03	3.00E-03	2.00E-02	6.00E-03	3.00E-03	3.00E-03	1.20E-02	1.20E-02	-	-	0.8	3.40E+09	0.25	1.20E+10	Roller	o	o
116	biotC=0.8_B=0.236	2.00E-02	6.00E-03	3.00E-03	3.00E-03	2.00E-02	6.00E-03	3.00E-03	3.00E-03	1.20E-02	1.20E-02	-	-	0.8	3.16E+09	0.236	1.20E+10	Roller	o	o
117	biotC=0.8_B=0.225	2.00E-02	6.00E-03	3.00E-03	3.00E-03	2.00E-02	6.00E-03	3.00E-03	3.00E-03	1.20E-02	1.20E-02	-	-	0.8	2.98E+09	0.225	1.20E+10	Roller	o	o
118	md1.5 jd0.5	2.00E-02	6.00E-03	3.00E-03	3.00E-03	2.00E-02	6.00E-03	3.00E-03	3.00E-03	1.20E-02	1.20E-02	0.50	1.50	0.8	2.60E+09	0.2	1.20E+10	Roller	o	o
119	B=0.2 md0.5 jd0 best Calib	2.00E-02	6.00E-03	3.00E-03	3.00E-03	2.00E-02	6.00E-03	3.00E-03	3.00E-03	1.20E-02	1.20E-02	-	0.50	0.8	2.60E+09	0.2	1.20E+10	Roller	o	o
120	B=0.7	2.00E-02	6.00E-03	3.00E-03	3.00E-03	2.00E-02	6.00E-03	3.00E-03	3.00E-03	1.20E-02	1.20E-02	-	0.50	0.8	5.77E+09	0.7	4.00E+09	Roller	o	o
121	B=0.8	2.00E-02	6.00E-03	3.00E-03	3.00E-03	2.00E-02	6.00E-03	3.00E-03	3.00E-03	1.20E-02	1.20E-02	-	0.50	0.8	8.06E+09	0.8	4.00E+09	Roller	o	o
122	B=0.9	2.00E-02	6.00E-03	3.00E-03	3.00E-03	2.00E-02	6.00E-03	3.00E-03	3.00E-03	1.20E-02	1.20E-02	-	0.50	0.8	1.17E+10	0.9	4.00E+09	Roller	o	o
123	-																	Roller	o	o
124	B=0.7	2.00E-02	6.00E-03	3.00E-03	3.00E-03	2.00E-02	6.00E-03	3.00E-03	3.00E-03	1.20E-02	1.20E-02	-	0.50	0.8	5.77E+09	0.7	4.00E+09	fixed	o	o
125	B=0.8	2.00E-02	6.00E-03	3.00E-03	3.00E-03	2.00E-02	6.00E-03	3.00E-03	3.00E-03	1.20E-02	1.20E-02	-	0.50	0.8	8.06E+09	0.8	4.00E+09	fixed	o	o
126	B=0.9	2.00E-02	6.00E-03	3.00E-03	3.00E-03	2.00E-02	6.00E-03	3.00E-03	3.00E-03	1.20E-02	1.20E-02	-	0.50	0.8	1.17E+10	0.9	4.00E+09	fixed	o	o
127	-																	fixed	o	o
128	a=0.8_B=0.25	2.00E-02	6.00E-03	3.00E-03	3.00E-03	2.00E-02	6.00E-03	3.00E-03	3.00E-03	1.20E-02	1.20E-02	-	0.50	0.8	3.40E+09	0.25	1.20E+10	fixed	o	o
129	a=0.9_B=0.25	2.00E-02	6.00E-03	3.00E-03	3.00E-03	2.00E-02	6.00E-03	3.00E-03	3.00E-03	1.20E-02	1.20E-02	-	0.50	0.9	3.16E+09	0.25	1.20E+10	fixed	o	o
130	a=1.0_B=0.25	2.00E-02	6.00E-03	3.00E-03	3.00E-03	2.00E-02	6.00E-03	3.00E-03	3.00E-03	1.20E-02	1.20E-02	-	0.50	1	2.98E+09	0.25	1.20E+10	fixed	o	o
131	a=0.8_B=0.236	2.00E-02	6.00E-03	3.00E-03	3.00E-03	2.00E-02	6.00E-03	3.00E-03	3.00E-03	1.20E-02	1.20E-02	-	0.50	0.8	3.16E+09	0.236	1.20E+10	fixed	o	o
132	a=0.8_B=0.225	2.00E-02	6.00E-03	3.00E-03	3.00E-03	2.00E-02	6.00E-03	3.00E-03	3.00E-03	1.20E-02	1.20E-02	-	0.50	0.8	2.98E+09	0.225	1.20E+10	fixed	o	o



## Appendix D: Structure of the electronic data base

### Overview

Digital data files containing all the history output data from FLAC3D modelling were made available to Nagra. The electronic data base ensures the traceability of the reported raw data and the results of data analyses and collects all graphical data representations. The electronic data base is compiled in the "Data" directory:



The history output files are classified into different folders, from case1 to case26. For each history output file, the following quantities are exported: axial strain, radial strain, deviatoric stress ( $\sigma_1 - \sigma_3$ ), axial stress ( $\sigma_1$ ), volumetric strain and average pore pressure. Also contained in the folder *hist\_data* are Excel files, in which output files can be imported to create comparative graphical representations. The following is a guidance to create Excel graphs using the history files.

### Figure generation for comparison between numerical tests (parametric study)

All the history data are imported into excel files (only for figures of comparison between numerical tests). Thus, no importation is needed for figure generation. For each sample orientation, two excel files are included (example: "p\_study\_1" and "p\_study\_2" for P samples).

Example: generate figures comparing the effect of critical strain value for cohesion of the first segment (i.e., mc1 and mf1).

- Step 1: Open the file "P\_study\_1" (for P samples) and go to the worksheet "analyses".
- Step 2: Check the parameter set table and find the corresponding n°. In this example, the corresponding n°s are 103 (for the reference case) and 104 (for the case using different "mc1" and "mf1").
- Step 3: go to the worksheet "compare". Type 103 and 104 in the cells "C2" and "C3" (next to "comp1" and "comp2").
- Step 4: in the same worksheet, type the legends in the cell "N2", "N3" and give the related value in the cells "O2", "O3" (i.e., N2 = mc1 and O2 = 0.02).
- Figures are generated in the worksheets "B\_vs\_epsA", "PP\_vs\_epsA" and "Q\_vs\_epsA".

- In the excel files of "xx\_study\_2" (with xx = P, S, X or Z), the comparison can be made up to three cases. The third case can be inputted in the worksheet "compare" (comp3).

### **Figure generation for comparison between FLAC3D and experimental data**

Use the file "FLAC3D\_vs\_EXP" to generate figures of any comparison between FLAC3D and experimental data. In the worksheet "param\_set", all the parameter set for different cases can be found (c.f. Appendix C). Simulations of "Task 1" (without strain hardening) correspond to the cases of n° 101 to n° 108. Simulations of "Task 2" starts from n° 109.

Example: generate the plot for p samples of the case 3 (reference case of the simulation "Task 1").

- Step 1: open the file "FLAC3D\_vs\_EXP".
- Step2: go to the worksheet "Feuille1" (or create a new worksheet), import the file /case3/hist\_P\_115\_2.out/ (for the sample P115).
- Step 3: Copy all the imported data and paste them in the worksheet "data\_P" of the cell "A3" (the paste data will cover from the cell "A3" to the cell "F3").
- Repeat step 2 and step 3 for the file /case3/hist\_P\_109\_3.out and /case3/hist\_P\_14\_4.out. Note that the paste should be made in the cell "L3" and the cell "W3" respectively for "hist\_P\_109\_3.out" and "hist\_P\_14\_4.out".
- Figures of P samples are automatically updated in the worksheets "Fig\_P\_B\_a", "Fig\_P\_pp\_a" and "Fig\_P\_qa".